



**Mayara Guilherme Marzano**

**Soft Chemistry Approaches for Synthesis of Less  
Agglomerated  $A_2M_3O_{12}$  and Structurally Related Ceramic  
Phases**

**Doctoral Thesis**

Thesis presented to the Programa de Pós-graduação em Engenharia de Materiais e de Processos Químicos e Metalúrgicos of PUC-Rio in partial fulfillment of the requirements for the degree of Doutor em Engenharia de Materiais e de Processos Químicos e Metalúrgicos.

Advisor: Prof. Bojan Marinkovic

Co-advisor: Prof<sup>a</sup>. Patricia Isabel Pontón Bravo

Rio de Janeiro

August 2022



**MAYARA GUILHERME MARZANO**

**Soft Chemistry Approaches for Synthesis of  
Less Agglomerated  $A_2M_3O_{12}$  and Structurally  
Related Ceramic Phases**

Thesis presented to the Programa de Pós-graduação em Engenharia de Materiais e de Processos Químicos e Metalúrgicos of PUC-Rio in partial fulfillment of the requirements for the degree of Doutor em Engenharia de Materiais e de Processos Químicos e Metalúrgicos. Approved by the Examination Committee.

**Prof. Bojan Marinkovic**

Advisor

Departamento de Engenharia Química e de Materiais - PUC-Rio

**Prof<sup>a</sup>. Patricia Isabel Pontón Bravo**

Co-Advisor

Escuela Politecnica Nacional

**Prof. Roberto Ribeiro de Avillez**

Departamento de Engenharia Química e de Materiais - PUC-Rio

**Dra. Anja Dosen**

International Center for Diffraction Data

**Dra. Lidija Mancic**

Institute of Technical Sciences of the Serbian Academy of Science and Arts

**Prof. Anderson Gabriel Marques da Silva**

Departamento de Engenharia Química e de Materiais - PUC-Rio

Rio de Janeiro, August 29<sup>th</sup>, 2022.

All rights reserved.

## Mayara Guilherme Marzano

Graduated in Mechanical Engineering at Pontificia Universidade Católica do Rio de Janeiro (Puc - Rio) in 2015 and obtained her M.Sc. Degree in Materials Engineering and Chemical and Metallurgical Processes from (Puc - Rio), as well as, post graduated in work safety engineer from UCP in 2018. She had experience in the synthesis of nanostructures, materials with low, negative, and near zero thermal expansion. Currently, she works as an installation and operation engineer in the sector of oil and gas.

### Ficha Catalográfica

Marzano, Mayara Guilherme

Soft chemistry approaches for synthesis of less agglomerated  $A_2M_3O_{12}$  and structurally related ceramic phases / Mayara Guilherme Marzano ; advisor: Bojan Marinkovic ; co-advisor: Patricia Isabel Pontón Bravo. – 2022.

134 f. : il. color. ; 30 cm

Tese (doutorado) - Pontificia Universidade Católica do Rio de Janeiro, Departamento de Engenharia Química e de Materiais.  
Inclui referências bibliográficas.

1. Engenharia Química e de Materiais – Teses. 2. Expansão térmica negativa. 3. Coprecipitação. 4. Aglomeração. 5. Sol-Gel Não-hidrolítico. I. Marinkovic, Bojan. II. Pontón, Patricia. III. Pontificia Universidade Católica do Rio de Janeiro. Departamento de Engenharia Química e de Materiais. IV. Título.

CDD: 620.11

A vida é um jogo de xadrez a qual você deve saber perder algumas peças para  
enfim dar a última jogada de mestre, o xeque-mate.  
Aos meus pais,  
Rita Marzano e Marcos Marzano.

## Acknowledgment

I'm very grateful to my parents and my brother for their support every time I stumbled, and for all the credibility deposited in me, complicity, partnership, teachings, and suggestions. My mother and father are my greatest inspiration for achievement and success. Every stone in the path must be diverted, and those that we cannot divert, serve as a basis for our ascension.

My advisor, Prof. Bojan Marinkovic, and my co-advisor Patricia Pontón remain grateful for the opportunity given to me to be able to demonstrate my potential, even with an audience that disbelieved. My deep admiration and respect. I appreciate all the teachings, help, and criticism that contributed to my professional development.

Thanks to Prof. Cremona, Rian Esteves, and Arthur Barreto for their collaboration in the non-hydrolytic sol-gel experiments. Thanks to Prof. Paula Jardim for the collaboration on the SEM/MET images. Thanks to Ronald Rojas for his collaboration in the DLS and zeta potential experiments. Thanks to Marco Antonio Abreu for his collaboration in the BET experiments. I would like to thank my friends at the Photocatalysis Laboratory for their friendship, contribution, and partnership.

I thank all my family for their strength, prayers, and faith that I would make it. I thank God that in moments of despair and lack of hope, he renewed my belief and strengthened me to move forward.

Love all of you.

This study was financed in part by the Coordenação de Aperfeiçoamento de Pessoal de Nível Superior - Brasil (CAPES) - Finance Code 001.

## Abstract

Marzano, Mayara Guilherme; Marinkovic, Bojan (Advisor); Pontón, Patricia (Co-Advisor). **Soft Chemistry Approaches for Synthesis of Less Agglomerated  $A_2M_3O_{12}$  and Structurally Related Ceramic Phases**. Rio de Janeiro, 2022. 134p. Tese de Doutorado - Departamento de Engenharia Química e de Materiais, Pontifícia Universidade Católica do Rio de Janeiro.

The aim of this work was to synthesize  $Al_2W_3O_{12}$  and  $ZrMgMo_3O_{12}$  submicronic powders using different soft-chemical routes, such as: co-precipitation and non-hydrolytic sol-gel (NHSG) to evaluate the effect of the methods on agglomeration degree of the as-prepared powders.  $Al_2W_3O_{12}$  was synthesized via co-precipitation, which includes i) simultaneously mixing reactants at room temperature, ii) simultaneously mixing reactants at 3.5 °C, iii) simultaneously mixing reactants with CTAB surfactant addition, and by non-hydrolytic sol-gel (NHSG). The purpose of each method was to study the effect of the synthesis parameters, such as, molarity (0.1 M and 0.005 M), calcination temperature on the morphology, size, and agglomeration of the powders, evaluated through specific surface areas. The best combination of synthesis parameters in both methods, co-precipitation, and NHSG, resulted in  $Al_2W_3O_{12}$  nanometric powders, with average primary particle sizes of 40 nm, and 45 nm, respectively.  $Al_2W_3O_{12}$  nanopowder, with high surface area ( $26 \text{ m}^2 \text{ g}^{-1}$ ), was prepared by the NHSG through a less laborious way than commonly reported in the literature for this type of ceramics. In addition, attempts to synthesize crystalline  $Al_2W_3O_{12}$  in one step by hydrothermal treatment at 180 °C have been performed, however, the desired phase did not crystallize.  $ZrMgMo_3O_{12}$  was synthesized *via* co-precipitation by total evaporation route. The influence of the calcination parameters such as temperature and time of the synthesized powders were assessed. Even though different calcination temperatures were tested a completely monophasic powder was not fully attained by total evaporation route, presenting at least, 27% of secondary phases. Two additional different co-precipitation routes have been applied which include i) co-precipitation by simultaneously mixing reactants, ii) co-precipitation by dropwise addition of reactants and controlled pH at 9, however, both methods were unsuccessful since the desired phase was not crystallized.

## Keywords

Zero and low thermal expansion;  $A_2M_3O_{12}$  ceramics; co-precipitation; non-hydrolytic sol-gel; total evaporation route; specific surface area.

## Resumo

Marzano, Mayara Guilherme; Marinkovic, Bojan (Advisor); Pontón, Patricia (Co-Advisor). **Métodos de Química Suave para a Síntese de Fases  $A_2M_3O_{12}$  Menos Aglomerados e Fases Cerâmicas Estruturalmente Relacionadas**. Rio de Janeiro, 2022. 134p. Tese de Doutorado - Departamento de Engenharia Química e de Materiais, Pontifícia Universidade Católica do Rio de Janeiro.

O objetivo deste trabalho foi sintetizar pós submicrônicos de  $Al_2W_3O_{12}$  e  $ZrMgMo_3O_{12}$  usando diferentes rotas de química suave, tais como: co-precipitação e sol-gel não hidrolítico (NHSG) para avaliar o efeito dos métodos no grau de aglomeração dos pós preparados.  $Al_2W_3O_{12}$  foi sintetizado via co-precipitação, que inclui i) mistura simultânea de reagentes à temperatura ambiente, ii) mistura simultânea de reagentes a 3,5 °C, iii) mistura simultânea de reagentes com adição de surfactante CTAB e por sol-gel não hidrolítico (NHSG). O objetivo de cada método foi estudar o efeito dos parâmetros de síntese, como molaridade (0,1 M e 0,005 M), temperatura de calcinação sobre a morfologia, tamanho e aglomeração dos pós, avaliados através de áreas superficiais específicas. A melhor combinação dos parâmetros de síntese em ambos os métodos, co-precipitação e NHSG, resultou em pós nanométricos de  $Al_2W_3O_{12}$ , com tamanhos médios de partículas primárias de 40 nm e 45 nm, respectivamente.  $Al_2W_3O_{12}$ , com alta área superficial ( $26 \text{ m}^2 \text{ g}^{-1}$ ), foi preparado pelo NHSG de forma menos trabalhosa do que comumente relatada na literatura para esse tipo de cerâmica. Além disso, tentativas de sintetizar  $Al_2W_3O_{12}$  cristalino em uma etapa por tratamento hidrotérmico a 180 °C foram realizadas, porém, a fase desejada não cristalizou.  $ZrMgMo_3O_{12}$  foi sintetizado via co-precipitação por rota de evaporação total. A influência dos parâmetros de calcinação como temperatura e tempo dos pós sintetizados foi avaliada. Apesar de terem sido testadas diferentes temperaturas de calcinação, um pó completamente monofásico não foi totalmente obtido por evaporação total, apresentando pelo menos 27% de fases secundárias. Duas rotas adicionais de co-precipitação foram investigadas, que incluem i) co-precipitação por mistura simultânea de reagentes, ii) co-precipitação por gotejamento de reagentes e pH controlado a 9, no entanto, ambos os métodos não tiveram sucesso, pois a fase desejada não foi cristalizada.

## Palavras-chave

Zero e baixa expansão térmica; cerâmica  $A_2M_3O_{12}$ ; co-precipitação; sol-gel não hidrolítico; rota de evaporação total; área específica da superfície.

# Contents

1.	Introduction	16
2.	Literature Review	18
2.1.	Fundamentals of thermal expansion	18
2.1.1	Negative thermal expansion (NTE)	19
2.1.2	$A_2M_3O_{12}$ Family and $ABM_3O_{12}$ subfamily	21
2.2.	The relevance of deagglomerated oxide nanopowders and the challenges of synthesis	23
2.2.1.	Intermolecular force impact on the synthesis of oxide nanoparticles	24
2.2.2.	pH	31
2.2.3.	Surfactant addition	32
2.2.4.	Aging time	33
2.2.5.	Temperature of crystallization	34
2.3.	Co-precipitation method	35
2.4.	Sol-Gel method	46
2.5.	Non-hydrolytic Sol-Gel	52
3.	Objectives	58
3.1	General objective	58
3.2	Specific objectives	58
4.	Comparison between different co-precipitation approaches for the synthesis of low-agglomerated $Al_2W_3O_{12}$ powders	59
4.1	Background	59
4.2.	Materials and methods	63
4.2.1.	Co-precipitation of $Al_2W_3O_{12}$ powders by mixing reactants at room temperature (Method A)	63
4.2.2.	Co-precipitation of $Al_2W_3O_{12}$ powders by mixing reactants at 3.5 °C (Method A35)	63
4.2.3.	Co-precipitation of $Al_2W_3O_{12}$ powders by mixing reactants at 45 °C (Method A45)	64

4.2.4. Co-precipitation of $\text{Al}_2\text{W}_3\text{O}_{12}$ powders by mixing reactants with CTAB surfactant addition (Method CTAB)	64
4.2.5. Characterization of amorphous precursor and crystalline $\text{Al}_2\text{W}_3\text{O}_{12}$ powders	65
4.3. Results	66
4.3.1. Amorphous $\text{Al}_2\text{W}_3\text{O}_{12}$ precursor powders	66
4.3.2. $\text{Al}_2\text{W}_3\text{O}_{12}$ calcined powder	69
4.4. Discussion	73
4.4.1. Effect of the molarity of the reactant starting solutions	73
4.4.2. Effect of the synthesis temperature during co-precipitation on the particle size of $\text{Al}_2\text{W}_3\text{O}_{12}$ powders	75
4.4.3. Effect of the crystallization temperature and calcination time on the particle size of $\text{Al}_2\text{W}_3\text{O}_{12}$ powders	76
4.5. Conclusions	80
5. Non-Hydrolytic Sol-Gel synthesis of $\text{Al}_2\text{W}_3\text{O}_{12}$ nanopowders	81
5.1 Background	81
5.2. Materials and methods	84
5.2.1. Synthesis of $\text{Al}_2\text{W}_3\text{O}_{12}$ powders by NHSG	84
5.2.2. Characterization of amorphous and crystalline $\text{Al}_2\text{W}_3\text{O}_{12}$ powders	85
5.3 Results and discussions	86
5.4 Conclusions	93
6. Evaluation of total evaporation route for the synthesis of zero thermal expansion $\text{ZrMgMo}_3\text{O}_{12}$ powders	94
6.1 Background	94
6.2 Materials and methods	97
6.2.1. Total evaporation route	97
6.2.2. Characterization of amorphous precursors and calcined powders	98
6.3 Results and discussions	99
6.4 Conclusions	106
7. Conclusions and future works	107
8. References	110
9. Appendix	125

## List of Figures

Figure 1: Potential energy (U) curves as a function of interatomic distance (r) for an ideal harmonic system (dashed curve) and an asymmetric, real-life, system (full curve) [1].	18
Figure 2: Schematic representation of transverse thermal vibration of A-O-M bonds (A and M are grey circles and O is a white circle) [3].	19
Figure 3: Coefficients of thermal expansion as a function of polyhedral ( $AO_6$ ) distortion in $A_2M_3O_{12}$ family [7].	22
Figure 4: Scheme showing the stages in the preparation of oxide nanoparticles.	24
Figure 5: Scheme showing the interaction of a liquid between a sphere and a flat surface (a) before contact and (b) after contact [12].	25
Figure 6: Capillary forces acting on the particles [13].	26
Figure 7: Electrical double layer [16].	27
Figure 8: The interaction potential energy varying with $K$ ( $K = \text{Debye-Hückel length (k) in cm}^{-1}$ ) [16].	28
Figure 9: A schematic illustration of zeta potential as a function of pH [17].	29
Figure 10: Schematic illustration of different types of surfactants [30].	32
Figure 11: - LaMer diagram [39].	39
Figure 12: Diagram for precipitation rate as a function of solute concentration [41].	40
Figure 13: Ostwald ripening effect [50].	43
Figure 14: Properties of the precipitate and the referred parameters that affect its characteristics. [37].	45
Figure 15: Schematic showing hydrolysis reaction (in green) and condensation reaction (in red) [35].	46
Figure 16: Three general steps in the sol-gel process [35].	48
Figure 17: Stages of drying (figure adapted from Fig.6 in Ref [55]).	49
Figure 18: Sol-Gel drying process [56].	50
Figure 19: Schematic showing the NHSG route applied for $Al_2W_3O_{12}$ phase.	55

Figure 20: TGA/DSC curves of amorphous precursor synthesized by Method A using (a) 0.1 M and (b) 0.005 M reactant aqueous solutions. ....	67
Figure 21: TGA/DSC curves of amorphous precursor synthesized by method A35 using 0.005 M reactant aqueous solutions.....	67
Figure 22: TGA/DSC curves of amorphous precursor synthesized by method CTAB at room temperature and using 0.005 M reactant aqueous solutions. ....	68
Figure 23: XRPD patterns of monophasic orthorhombic $\text{Al}_2\text{W}_3\text{O}_{12}$ , obtained by method A (0.1 M reactant aqueous solutions) and calcined at different temperatures for 20 min. ....	71
Figure 24: XRPD patterns of monophasic orthorhombic $\text{Al}_2\text{W}_3\text{O}_{12}$ , obtained by method A (0.005 M reactant aqueous solutions) and calcined at different temperatures for 20 min, if it is not marked different. ....	71
Figure 25: XRPD patterns of monophasic orthorhombic $\text{Al}_2\text{W}_3\text{O}_{12}$ , obtained by method A35 (0.005 M reactant aqueous solutions) and calcined at different temperatures for 20 min, if it is not marked different. ....	72
Figure 26: XRPD patterns of monophasic orthorhombic $\text{Al}_2\text{W}_3\text{O}_{12}$ , obtained by method A45 (0.005 M reactant aqueous solutions) and calcined at different temperatures for 20 min. ....	72
Figure 27: XRPD patterns of orthorhombic $\text{Al}_2\text{W}_3\text{O}_{12}$ obtained by Method CTAB (0.005 M of reactant aqueous solutions) and calcined at different temperatures. ↓ stands for a diffraction peak of $\text{WO}_3$ . ....	73
Figure 28: Relationship between supersaturation, nucleation, and growth [38]. ....	75
Figure 29: Relationship between specific surface areas ( $\text{m}^2\text{g}^{-1}$ ) and calcination temperatures (samples calcined during 20 min).....	78
Figure 30: Relationship between specific surface areas ( $\text{m}^2\text{g}^{-1}$ ) and calcination time for samples of method A calcined at 625 and 635°C. ....	79
Figure 31: TGA/DSC curves of amorphous $\text{Al}_2\text{W}_3\text{O}_{12}$ -based precursors synthesized by NHSG (a) $\text{pAl}_2\text{W}_3\text{O}_{12}$ _NHSG_0.1M (b) $\text{pAl}_2\text{W}_3\text{O}_{12}$ _NHSG_0.005M. ....	87

Figure 32: XRPD patterns of orthorhombic $\text{Al}_2\text{W}_3\text{O}_{12}$ (0.1 M) obtained by NHSG route; * stands for a diffraction peak of monoclinic $\text{WO}_3$ . .....	88
Figure 33: XRPD patterns of orthorhombic $\text{Al}_2\text{W}_3\text{O}_{12}$ (0.005 M) obtained by NHSG route; * stands for a diffraction peak of monoclinic $\text{WO}_3$ . .....	88
Figure 34: SEM images of monophasic orthorhombic $\text{Al}_2\text{W}_3\text{O}_{12}$ (0.005 M) calcined at $660^\circ\text{C}$ . .....	91
Figure 35: TEM images of monophasic orthorhombic $\text{Al}_2\text{W}_3\text{O}_{12}$ (0.005 M). (a-b) Sample calcined at $660^\circ\text{C}$ . .....	92
Figure 36: Total evaporation route for synthesis of orthorhombic $\text{ZrMgMo}_3\text{O}_{12}$ . .....	98
Figure 37: TGA and DSC curves of the precursor powder ( $\text{pZrMgMo}_3\text{O}_{12\_ET}$ ). Endothermic peaks are marked as $\downarrow$ , and the exothermic peak is marked as $\uparrow$ . .....	100
Figure 38: XRPD patterns of calcined powders. $\text{ZrMo}_2\text{O}_8$ diffraction lines are marked as $\blacksquare$ , $\text{ZrO}_2$ peaks are marked as $\bullet$ , $\text{MgMoO}_4$ peaks are marked as $\blacktriangledown$ , and peaks related to $\text{MoO}_3$ are marked with $\blacktriangle$ . The main phase is orthorhombic $\text{ZrMgMo}_3\text{O}_{12}$ . .....	104
Figure 39: SEM images of the sample calcined at $700^\circ\text{C}$ .....	105
Figure 40: Co-precipitation by mixing reactants as an attempt to prepare a $\text{ZrMgMo}_3\text{O}_{12}$ precursor. .....	128
Figure 41: Co-precipitation by dripping reactants at controlled pH ( 9) as an attempt to synthesize $\text{ZrMgMo}_3\text{O}_{12}$ . .....	130
Figure 42: TGA/DSC of $\text{ZrMgMo}_3\text{O}_{12}$ precursors obtained by co-precipitation by mixing reactants (a) S1; (b) S2; (c) S3 (d) S4 and (e) S5. ....	131
Figure 43: XRPD of samples obtained by co-precipitation by mixing reactants as an attempt to synthesize $\text{ZrMgMo}_3\text{O}_{12}$ . .....	132
Figure 44: Co-precipitation dripping reactants at pH control $\sim 9$ (a) TGA/DSC of pGC; (b) XRPD of the calcined powder GC_800 $^\circ\text{C}$ .....	133

## List of Tables

Table 1: Examples of temperature ranges to synthesize the study phases .....	22
Table 2: Average size of silica nanoparticles.....	34
Table 3: Concentration of SDS vs. Ostwald ripening rate .....	44
Table 4: Different synthesis routes for the preparation of $\text{Al}_2\text{W}_3\text{O}_{12}$ powders .....	60
Table 5: Synthesis conditions applied for each method and the specific surface areas and average particle sizes ( $d_{\text{BET}}$ ) of the as-prepared $\text{Al}_2\text{W}_3\text{O}_{12}$ powders. The density of orthorhombic $\text{Al}_2\text{W}_3\text{O}_{12}$ phase used for the $d_{\text{BET}}$ calculation was $5.12 \text{ g cm}^{-3}$ [114]. .....	70
Table 6: Comparison between different methods evaluating the effect of the crystallization temperature and calcination time on the particle size for orthorhombic $\text{Al}_2\text{W}_3\text{O}_{12}$ phase.....	79
Table 7: Specific surface areas and the average particle sizes of orthorhombic $\text{Al}_2\text{W}_3\text{O}_{12}$ powders, prepared by NHSG using different molarities and calcined at different temperatures.....	89
Table 8: Different synthesis routes for the preparation of $\text{ZrMgMo}_3\text{O}_{12}$ and its solid solutions, as reported in the literature. ....	95
Table 9: Phase composition of crystallized powders, prepared by total evaporation, followed by rapid calcination at different temperatures and times.....	102
Table 10: Quantitative phase analysis of the powders crystallized at different temperatures and times.....	103
Table 11: pH synthesis conditions applied to reach $\text{ZrMgMo}_3\text{O}_{12}$ by mixing reactants .....	129
Table 12: Calcination temperature of $\text{ZrMgMo}_3\text{O}_{12}$ precursors obtained through co-precipitation by mixing reactants. $\text{ZrMo}_2\text{O}_8$ presents in the samples is a hexagonal phase. ....	132

## List of Equations

Equation 1: Coefficient of linear expansion from 23 °C to 1000 °C .....	20
Equation 2: Coefficient of linear compression to 100 kbar .....	20
Equation 3: Thermal shock resistance ( $R_s$ ) .....	20
Equation 4: Capillary pressure .....	26
Equation 5: Electric potential varies with distance .....	27
Equation 6: Debye-Hückel length .....	28
Equation 7: Ionic strength .....	28
Equation 8: Example of a general reaction .....	37
Equation 9: Solubility product constant, $K_{sp}$ .....	37
Equation 10: Supersaturation .....	37
Equation 11: Dependence between nucleation rate and supersaturation	38
Equation 12: Growth rate (G) .....	38
Equation 13: Total Free Energy Variation .....	40
Equation 14: Critical radius .....	40
Equation 15: Number of spherical embryos .....	41
Equation 16: Number of stable nuclei .....	41
Equation 17: Relationship between equilibrium concentration and precipitate radius .....	42
Equation 18: Diffusion current of solute .....	42
Equation 19: Radius of the precipitate varying with time .....	42
Equation 20: Gibbs-Thomson .....	43
Equation 21: Ostwald ripening rate ( $W_T$ ) .....	43
Equation 22: Hydrolysis reaction .....	46
Equation 23: Condensation reaction .....	47
Equation 24: Alkyl halide elimination reaction .....	53
Equation 25: Metal alkoxide group formed in situ by reaction of metal chloride with ether .....	53
Equation 26: Metal alkoxide group formed in situ by reaction of metal chloride with primary/secondary alcohols .....	53
Equation 27: NHSG redistribution reaction .....	54
Equation 28: NHSG heterocondensation reaction .....	54
Equation 29: NHSG homocondensation reaction .....	54

Equation 30: Ether elimination reaction.....	55
Equation 31: Ester elimination reaction.....	56
Equation 32: Acetamide elimination reaction.....	56
Equation 33: Heterocondensation reaction .....	56
Equation 34: Self-condensation reaction.....	56
Equation 35: Johnson-Mehl-Avrami-Kolmogorov .....	68
Equation 36: Rate of nucleation .....	74
Equation 37: Rate of crystal growth.....	74
Equation 38: Arrhenius equation .....	76
Equation 39: Borgwardt equation .....	77

## 1. Introduction

Bulk ceramic materials are dependent on their chemical composition, crystal arrangement, and microstructure since these determine their properties and applications and classified them as traditional or advanced. Advanced ceramics exhibit superior mechanical properties, corrosion/oxidation resistance, electrical, optical, and/or magnetic properties and these depend on the powder synthesis route.

The ceramic powder synthesis methods are commonly classified into two groups: a) high energy synthesis, such as solid-state reaction, and b) low energy synthesis such as sol-gel, solvothermal routes, and coprecipitation. High energy methods requires homogenous distribution of precursor, high temperatures, and extended time of calcination leading to the synthesis of stable phases with large particles. On the other hand, low energy methods require low temperatures and reaction times, promoting the synthesis of stable and metastable phases with small particles.

These kinds of methods allow the synthesis of thermomiotic ceramics, which exhibits low-positive, near-zero, or negative thermal expansion. Important applications of these materials might be in high thermal shock resistance, when in a bulk form, or as a fine thermal expansion controller when incorporated as the dispersed phases in a polymer, metal or ceramic matrix.

In this context,  $\text{Al}_2\text{W}_3\text{O}_{12}$  and  $\text{ZrMgMo}_3\text{O}_{12}$  (orthorhombic phases) are good candidates to fulfill these requirements due to low thermal expansion. The challenge during the synthesis of nanosized powders is to minimize the agglomeration of particles, going against the natural path since nanoparticles have higher surface energy. To reach a stable state, the particles agglomerate in order to minimize the surface energy.

Thereby, this thesis is intended to study different co-precipitation methods to synthesize  $\text{Al}_2\text{W}_3\text{O}_{12}$  and  $\text{ZrMgMo}_3\text{O}_{12}$  submicronic powders in a deagglomerated form and to develop a new route based on Non-Hydrolytic Sol-Gel to synthesized  $\text{Al}_2\text{W}_3\text{O}_{12}$ . The following is a brief description of the subsequent chapters:

- Chapter 2: Theoretical foundations of the thermal expansion properties of the  $A_2M_3O_{12}$  family, fundamentals of co-precipitation route, and the synthesis by sol-gel, including the non-hydrolytic sol-gel (NHSG).
- Chapter 3: Objectives of the thesis.
- Chapter 4: Comparison between different co-precipitation approaches for the synthesis of low-agglomerated  $Al_2W_3O_{12}$  powders
- Chapter 5: Non-Hydrolytic Sol-Gel synthesis of  $Al_2W_3O_{12}$  nanopowders.
- Chapter 6: Evaluation of total evaporation route for the synthesis of zero thermal expansion  $ZrMgMo_3O_{12}$  powders
- Chapter 7: Conclusion and future works

## 2. Literature Review

### 2.1. Fundamentals of thermal expansion

Materials typically change their dimensions as temperature increases, most commonly experiencing dilatation, i.e., positive thermal expansion (PTE). Expansion can cause thermal stress when the material is exposed to external restrictions, such as in the case of brazed parts, resulting in possible structural damage.

The phenomenon of thermal expansion is understood through the potential energy well as a function of interatomic distances. Normally, when temperature increases, the bond distances between the atoms increase as well, expanding the material as a whole due to the well asymmetry. Figure 1 depicts the interatomic equilibrium distance at a temperature of 0 K corresponding to the minimum point of the well [1-2].

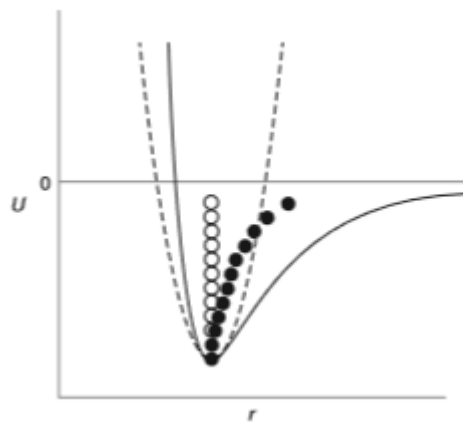


Figure 1: Potential energy ( $U$ ) curves as a function of interatomic distance ( $r$ ) for an ideal harmonic system (dashed curve) and an asymmetric, real-life, system (full curve) [1].

On heating, the vibrational (kinetic) energy increases, and thus, being the well, more or less, asymmetric the average distances between atoms increase, resulting in overall material expansion [1]. If the potential energy curve were symmetrical, even with the increase of the average vibrational amplitude of the

atoms, there would be no resulting variation in the interatomic distance and, consequently, there would be no thermal expansion.

### 2.1.1 Negative thermal expansion (NTE)

In a solid crystal, the oscillations of atoms about their equilibrium positions form a regular mesh represented as collective vibrations of atoms in the crystal lattice. The atoms are bonded to their neighbors and the vibrations are not independent of each other. Phonons are represented as quanta of lattice vibration, playing an important role in various solid state phenomena, in which vibration waves can be propagated in the longitudinal or transverse directions [3].

Negative and near-zero thermal expansion cannot be explained by the potential energy well and it is explained through the transversal motion of oxygen or some other ion within the 2-folded coordination. An example of A-O-M bond (where M and A is a cations and O the oxygen atom) is shown in Figure 2. As the temperature increases, longitudinal (high energy modes) and transverse (low energy modes) vibrations are populated [2-5].

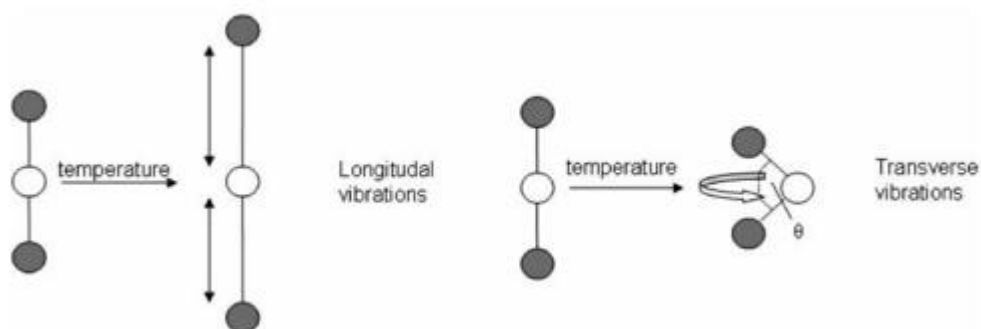


Figure 2: Schematic representation of transverse thermal vibration of A-O-M bonds (A and M are grey circles and O is a white circle) [3].

According to the potential energy curve shown in Figure 1, the stronger the bond, the lower the thermal expansion. Therefore, strong chemical bonds of A-O and M-O types are one of the main requirements for the predominance of the effect

of transverse vibrations on thermal expansion. Hazen and Prewit [6] developed empirical functions (Equation 1 and Equation 2) to determine values of expansion and compression coefficients for several metal-oxygen bonds assuming that metal-oxygen distances vary approximately linearly with temperature or pressure. The relationships between bond expansion, compression, and other bonding variables are:

Equation 1: Coefficient of linear expansion from 23 °C to 1000 °C

$$\alpha = 32.9 (0.75 - z/p) \times 10^{-6} \text{ } ^\circ\text{C}^{-1}$$

Equation 2: Coefficient of linear compression to 100 kbar

$$\beta = 37.0 (d_0^3/z) \times 10^{-6} \text{ kbar}^{-1}$$

where  $z$  is the cation charge and  $p$  is the cation coordination number,  $d_0$  means polyhedral metal - oxygen distance at 1 atm and 23 °C. The authors noted that all cations having similar values of  $\alpha/\beta$  will correspond in structurally similar ways to variations of pressure and temperature.

The thermomiotic materials (materials that contract when heated) present interesting features beyond the negative thermal expansion. The heat capacity, due to the vibrational modes (phonons), makes the material adopt different behavior. The strong chemical bonds intensify the effect of transverse vibrations and therefore, the materials present less thermal expansion. Thus, the displacements between vibrational energy levels increase, characterizing the low heat capacity of NTE materials. Also, the structure of NTE materials allows the reduction of the phonon mean free path compared with less flexible materials [1].

The related properties, such as thermal conductivity and thermal shock resistance are also associated with the heat capacity and the coefficient of thermal expansion (CTE), respectively. If the CTE of the material becomes lower and approaches zero, the thermal shock resistance will be increased (Equation 3):

Equation 3: Thermal shock resistance ( $R_s$ )

$$R_s = \frac{k\sigma}{|\alpha|E}$$

where  $k$  is the thermal conductivity,  $\sigma$  is the material strength,  $\alpha$  is the CTE and  $E$  is Young's modulus.

### 2.1.2

#### **A<sub>2</sub>M<sub>3</sub>O<sub>12</sub> Family and ABM<sub>3</sub>O<sub>12</sub> subfamily**

The A<sub>2</sub>M<sub>3</sub>O<sub>12</sub> family has large chemical flexibility and is commonly defined as an open framework built from AO<sub>6</sub> octahedrons sharing all their vertices with MO<sub>4</sub> tetrahedrons [1].

- A is a trivalent cation of transition metals or lanthanides occupying octahedral position.
- M is a hexavalent cation, such as W<sup>+6</sup> or Mo<sup>+6</sup>, occupying tetrahedral position.
- O is an oxygen anion.

HfMgMo<sub>3</sub>O<sub>12</sub> and ZrMgMo<sub>3</sub>O<sub>12</sub> phases are an example of the subfamily ABM<sub>3</sub>O<sub>12</sub>. This subfamily, as the A<sub>2</sub>M<sub>3</sub>O<sub>12</sub> family, also presents an open framework crystal structure sharing polyhedral and octaetra. The following items are related to the equivalent chemical element:

- A= Hf<sup>4+</sup> / Zr<sup>4+</sup>
- B= Mg<sup>2+</sup> / Mn<sup>2+</sup>
- M= W<sup>6+</sup> / Mo<sup>6+</sup>

The materials from A<sub>2</sub>M<sub>3</sub>O<sub>12</sub> family present anisotropic thermal expansion and in the monoclinic structure the three axes expand, while in the orthorhombic structure this behavior depends on the size of the trivalent cation (A).

The cations with a small radius (approximately 143 pm, such as aluminum) form AO<sub>6</sub> octahedrons with strong oxygen-oxygen repulsions, due to the short distances between oxygen, providing rigidity to the polyhedron and reducing the coordinated movement. As the A<sup>3+</sup> cation size increases, the CTE becomes more negative, once larger cationic radii result in a greater distortion of polyhedra. Large radii such as yttrium, which has an atomic radius of 180 pm, expand the octahedron, AO<sub>6</sub>, increasing the oxygen-oxygen distances and decreasing the oxygen-oxygen repulsions in the polyhedron that allows the coordinated movement of the polyhedron. In addition, when the size of cation A increases, the free spaces in the structure become large enough to admit small molecules, such as water, that can

inhibit the movement of polyhedron. The materials with high hygroscopicity prevent their NTE performance at room temperature and the phase shows positive thermal expansion.

Figure 3 presents the coefficient of thermal expansion of the main members of the  $A_2M_3O_{12}$  family.

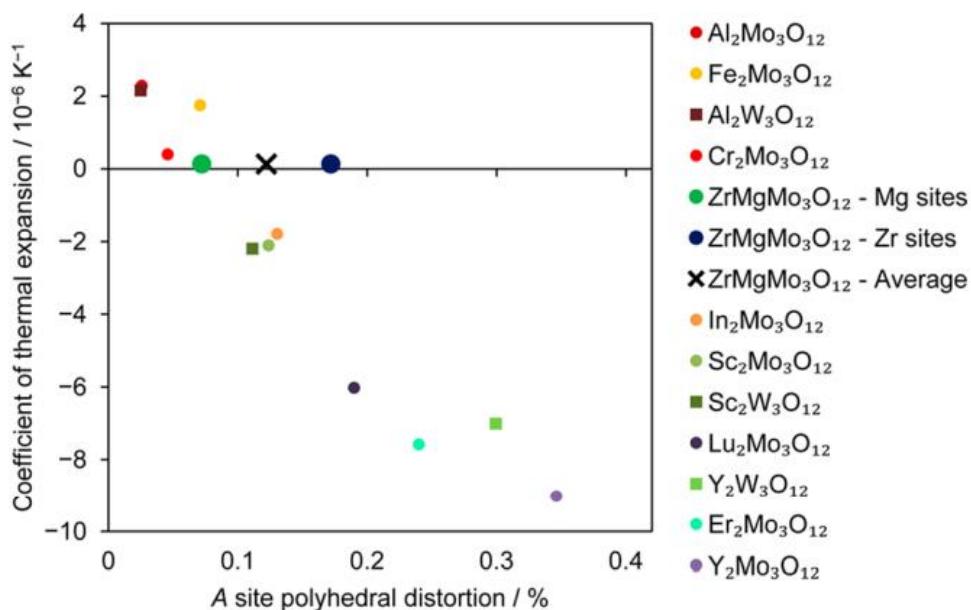


Figure 3: Coefficients of thermal expansion as a function of polyhedral ( $AO_6$ ) distortion in  $A_2M_3O_{12}$  family [7].

Table 1 shows temperature ranges to synthesize in an orthorhombic structure the phases of interest for this study. The orthorhombic structure is more attractive than monoclinic structure once the first one usually has a negative CTE.

Table 1: Examples of temperature ranges to synthesize the study phases

Phase	Temperature for crystallization ( $^{\circ}C$ )
$Al_2W_3O_{12}$ [8]	Room temperature – 1100 [8]
$ZrMgMo_3O_{12}$ [7]	(-126) – 700 [7]

## 2.2.

### **The relevance of deagglomerated oxide nanopowders and the challenges of synthesis**

The thermomiotics of the  $A_2M_3O_{12}$  family, due to their intrinsic characteristics described above, can be applied in a bulk form or as a fine thermal expansion controller when incorporated as the dispersed phases in a metal, ceramic, or polymer matrix.

The polymer composites, generally, are reinforced by fillers to improve their mechanical and physical properties and the use of nanoscale fillers provides a huge interfacial area per unit volume between the nanofillers and polymers which is beneficial for and leads to superior properties [9]. The agglomerated nanoparticles are not able to be dispersed homogeneously into the matrix acting as stress concentrators, which implies the reduction of the mechanical properties in nanocomposites.

The main challenge during the synthesis of thermomiotics is to achieve well dispersed and nanosized particles. However, the synthesis stage is not the only main point to take care of to avoid agglomeration. The materials in a bulk form, generally, shall be sintered at high temperatures, which can cause grain growth and a decrease in mechanical strength.

The low thermal conductivity of  $A_2M_3O_{12}$  family in a bulk form makes these materials good candidates for thermal shock resistance applications. Prisco et al.[10], studied the mechanical and physical properties of  $Al_2W_3O_{12}$  sintered by two different methods: pressureless three-stage sintering (TSS) and spark plasma sintering (SPS). The  $Al_2W_3O_{12}$  bulk samples composed of nanometric grains (200 nm), obtained by SPS, were approximately 50 % stiffer and harder than the material produced from TSS (mean grain size  $\approx 2 \mu\text{m}$ ).

Figure 4 shows the principal stages during the preparation of oxide nanoparticles.

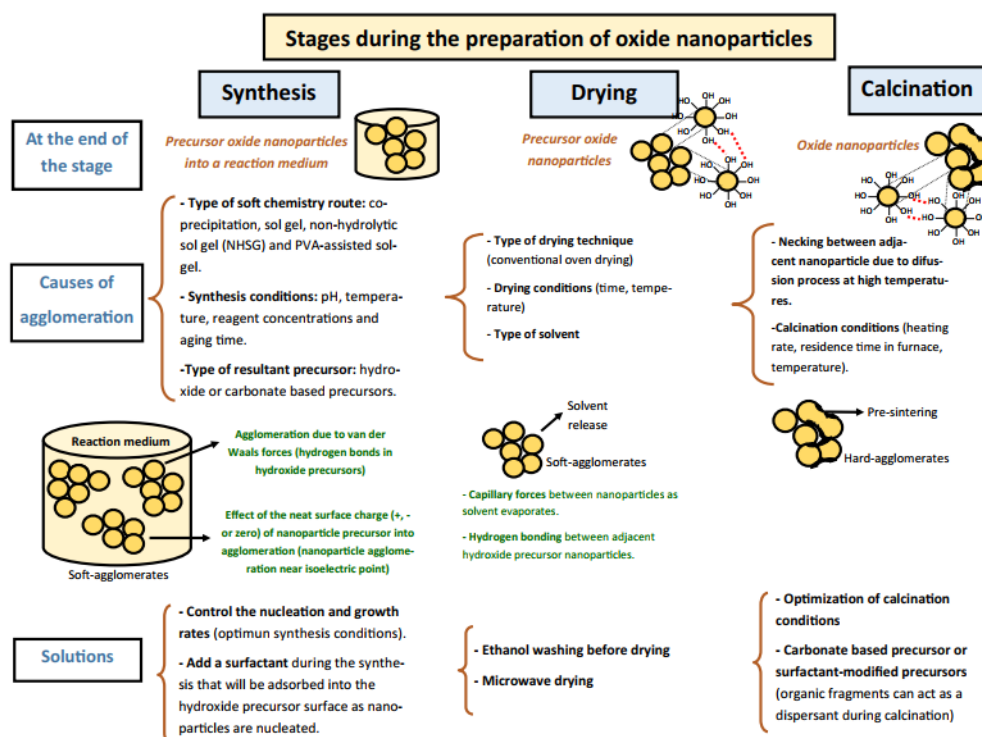


Figure 4: Scheme showing the stages in the preparation of oxide nanoparticles

### 2.2.1. Intermolecular force impact on the synthesis of oxide nanoparticles

The high specific surface area can also turn itself into a problem for nanoparticles. The nanoparticles are in a thermodynamic state of higher surface energy and consequently clump together to reach a more stable state by minimizing surface energy. Thus, micron-sized agglomerates tend to be formed by van der Waals forces, while the state of agglomeration is affected by the synthesis method [11].

The phenomena of adhesion become significant as decreases in particle size. The Van der Waals force is associated with dispersion force. The dispersion force is related to the instantaneous positions of the electrons around an atomic nucleus, in this way, an electric dipole field is formed at any instant of time which induces neighbor atoms to be polarized. Thus, the dispersion force corresponds to the electrostatic interaction of these induced dipoles with each other. The steric

repulsion is associated with the overlap of the electron clouds of two different atoms at a distance close to the atomic radius, which leads to strong electrostatic repulsion [12].

The wet material has for each particle a thin liquid film due to the condensation of water from the atmosphere and this leads to a strong cohesive force between the particles due to the liquid bridge. This liquid bridge introduces a capillary force that attracts the two particles toward each other, leading to the adhesion of the particles. Figure 5 shows the geometrical parameters for a liquid bridge between spherical particle and flat surface. The  $r_1$  is the radius of the liquid meniscus between the interface profile leading to a liquid bridging adhesion,  $r_2$  is the distance of a triple point,  $\theta$  is the solid/liquid contact angle,  $\phi$  is the half of the angle and depends on the liquid bridge volume, being a measure of the capillary force [12].

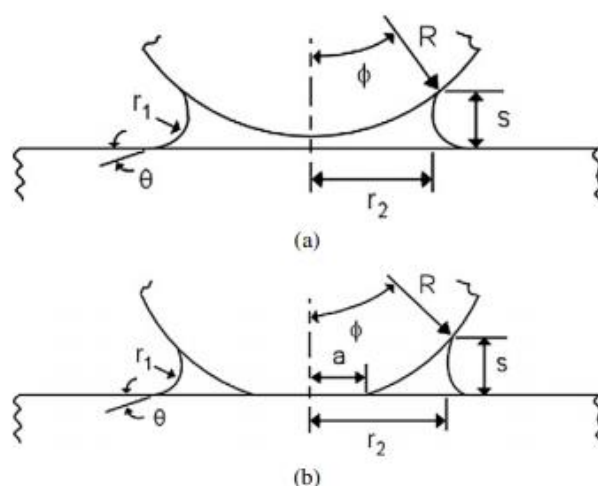


Figure 5: Scheme showing the interaction of a liquid between a sphere and a flat surface (a) before contact and (b) after contact [12].

The attraction force between two particles is dependent on their separation distance and can be expressed through the capillary forces (capillary pressure). Therefore, drying techniques that aim to reduce capillary forces can avoid particle agglomeration. The capillary forces ( $F_c$ ) do not contribute to the agglomeration of the particles when a critical distance between them ( $L_c$ ) is overcome (Figure 6). If the critical distance of the particles is less than  $L_c$ , the remaining wet powder after drying will agglomerate due acting of capillary forces [13].  $F_a$  is the adhesion force

and  $L_c$  is defined as a critical distance below which two particles cannot resist the capillary forces.

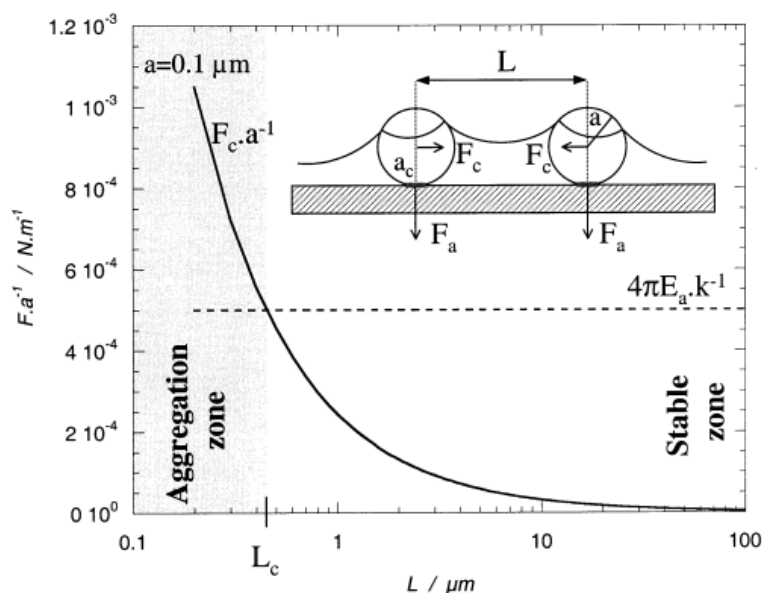


Figure 6: Capillary forces acting on the particles [13].

The high-energy liquid/vapor interfaces, from the remaining colloids after the drying process, increase the capillary pressure promoting the agglomeration of the particles. The basic relationship between capillary pressure ( $P$ ), the interfacial tension between liquid/vapor energy ( $\sigma$ ), contact angle ( $\theta$ ), and radius of curvature ( $r_p$ ) is given by Equation 4 [14]:

Equation 4: Capillary pressure

$$P = \frac{2\sigma \cos(\theta)}{r_p}$$

The liquid layer that surrounds the particle is composed of two parts: i) an internal region, where the ions of a solution are strongly linked to the particle, and ii) an external region, where they are less linked forming a double electrical layer around each particle. The internal region, the boundary of the layer closest to the charged particle surface composed of counter ions, is defined as the Stern layer. The external region, the diffuse layer, presents a limit where the ions within this move with the particle. This frontier is the sliding plane and its potential is known as the zeta potential (Figure 7). The zeta potential is a measure of the stability of dispersion and depends critically on the magnitude of the electrostatic potential ( $\Psi_0$ ) at the surface of the colloidal particles [15].

The electrostatic stabilization is limited by the kinetic stabilization once the distributions are determined by electrostatic force and Brownian motion.

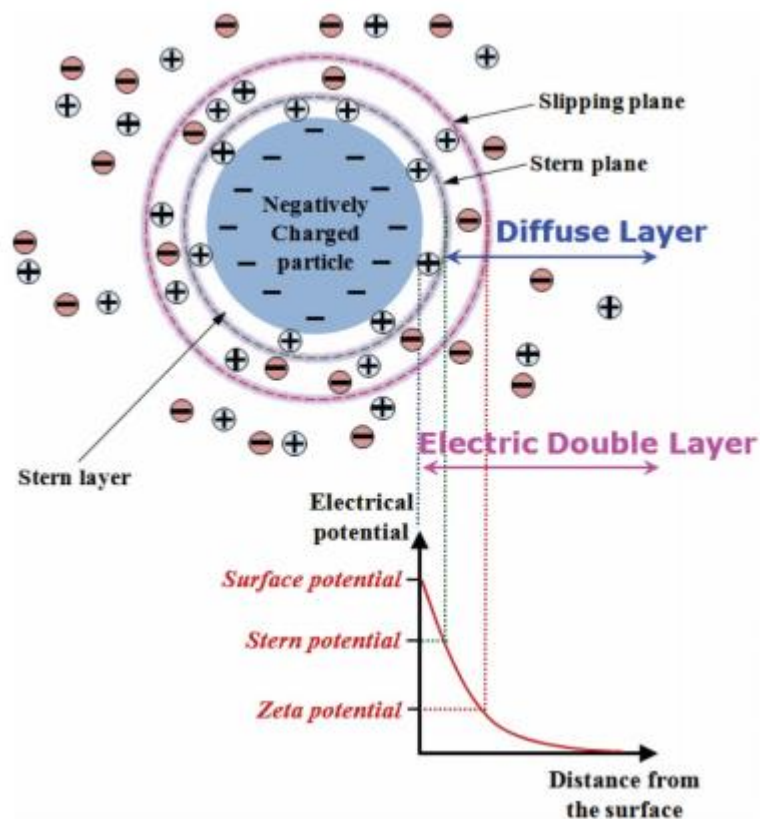


Figure 7: Electrical double layer [16]

The electric potential ( $\Psi$ ) varying with distance ( $x$ ) from the surface can be described as Equation 5.

Equation 5: Electric potential varies with distance

$$\Psi(x) = \Psi_s e^{-kx}$$

Where,  $\Psi_s$  is the Stern potential, and  $k$  is the double layer thickness.

The double layer thickness is characterized by Debye-Hückel length ( $1/k$ ) defined by Equation 6 and varies with ionic strength ( $I$ ) expressed by Equation 7. The equations show that as the ionic strength increases,  $k^{-1}$  (which the potential varies by  $1/e$ ) decreases, thus, the double layer thickness increases and, therefore, the zeta potential decreases. Figure 8 clarifies this effect of electrolyte concentration on the interaction potential energy ( $X$  axis is the separation distance between particles and  $Y$  axis is the interaction energy). The increment of concentration, thus,

the increase of the ionic strength, increases the  $k$ , therefore, resulting in a faster decrease of the electric potential.

Equation 6: Debye-Hückel length

$$k^{-1} = 1.988 \cdot 10^{-10} \sqrt{\frac{\epsilon_r T}{I}}$$

Where  $I$  is the ionic strength of the electrolyte,  $\epsilon_r$  is the dielectric constant (permittivity of the solvent),  $T$  is the temperature (in K).

Equation 7: Ionic strength

$$I = \sum \frac{c_i z_i^2}{2}$$

Where  $c$  is the concentration of ions with valence  $z$ .

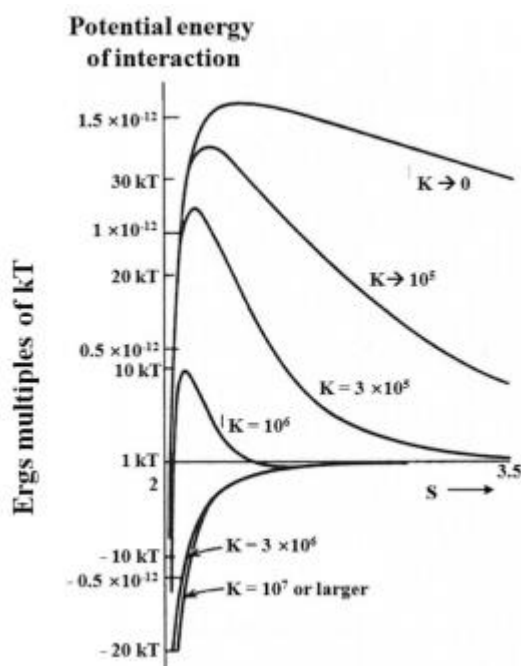


Figure 8: The interaction potential energy varying with  $K$  ( $K = \text{Debye-Hückel length } (k) \text{ in } \text{cm}^{-1}$ ) [16]

The double electric layer theory deals with the distribution of ions, and, therefore, the intensity of the electrical potentials that occur on the charged surface.

Thus, ionic conditions such as pH control the thickness of the electrical double layer and thereby the interaction distance among the particles.

The magnitude of the zeta potential indicates the stability of the colloid system. If particles in suspension have a high zeta potential, negative or positive, normally characterized by  $> \pm 30$  mV, the particles will tend to repel and there will be no tendency to agglomeration. However, if the pH value where the zeta potential is zero, defined as the isoelectric point, (Figure 9), the interaction potential energy of the particles will be neutral and there will be no force to avoid the agglomeration of particles. The isoelectric point of the solution corresponds to the point of minimum solubility of the solid.

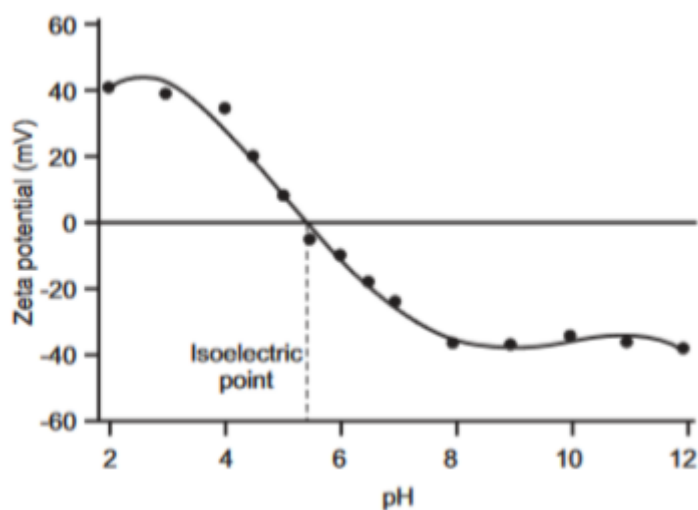


Figure 9: A schematic illustration of zeta potential as a function of pH [17]

However, when two particles approach, the repulsive interactions caused by hydration force (when the solvent is water) or solvation force (for any other polar solvent) in a liquid medium, the predictions of double electrical layer theory is not obeyed [18].

Solvation is a phenomenon that occurs when an ionic or polar compound dissolves in a polar substance (cosolute). This dissolution is related to the rupture of bonds or intermolecular forces present in the solute, generating bonds between the molecules of the solute and the molecules of the solvent. The hydration force is a repulsive force that acts between polar surfaces separated by a thin layer of water or other polar solvents. The repulsive force between two surfaces into contact is

related to the energy required to remove the water of hydration from the surface due to the strong charge-dipole, dipole-dipole, or H-bonding interactions [16].

The mechanism of the hydration force is that the solvent molecules are bound strongly and form a hydration layer around the cosolute and an overlap of the solvent layers between those charges leads to a repulsive force. The cosolute can be repelled or attracted to the surfaces of the macromolecules, thus, a cosolute can increase or decrease the stability of dispersion [16].

On the other hand, for hydrophobic surfaces (not applied for ceramics oxides once that are always hydrophilic) a different interaction is observed once, hydrophobic surfaces attract each other and this behavior is called London dispersive interaction. The origin of the London force is the redistribution around the charge, which polarizes the electron clouds in adjacent molecules, resulting in nonpolar intermolecular attraction [16].

Until now, the interaction of colloidal particles was explained by different types of mechanisms, such as dispersion forces, the electrical double-layer force, steric forces, hydration (solvation) forces, and hydrophobic forces. These cases show that an inhomogeneous surface layer due to the counter-ion distribution results in a net repulsive or attractive interaction [19].

Although several articles [20-21] study the influence of aging time on particle size, these usually do not rationalize the phenomenon, evidencing only its existence, without exploring the driving force behind this tendency.

Parks and Bruyn [22] defend the variation in pH with aging time and relate this phenomenon to the possible dissolution of amorphous layers on the oxide surface. Thus, the internal layers could favor the reabsorption of hydroxyl species in solution back onto the oxide surface and in this way, promote a displacement of the isoelectric point [23].

Cromieres et al. [24] measured for colloidal hematite the variation of the zeta potential with aging time. The dispersion was aged in an interval between 0, 24, and 48 h at 0.1 M under mixture in hermetically closed polycarbonate tubes. The initial isoelectric point was measured at 9.5, but after 24 h it decreased to 7.5 (similar variations were obtained for 0.001 M). The authors explained that during storage and aging,  $H^+$  ions were released which could have been incorporated into the particles during their storage in the acidic medium. However, if the  $H^+$  ions are

incorporated into the particles the medium would be more basic. In this way, very likely, the  $H^+$  ions were released from the inner layer of particles and could have been incorporated into the solution keeping the medium more acidic. The zeta potential decreases when ionic strength increases, as explained before. This phenomenon corresponds to the increase of the effect of the counter ions.

The conditions of storage after synthesis can also affect the zeta potential. Furlong et al. [25], studied the isoelectric point of titanium dioxide and alumina colloids during the aging time of dispersions in glass and polyethylene vessels. The authors observed that the isoelectric point of each colloid decreases as aging time in the glass vessel but remains constant in polyethylene. This fact was associated with increases in the concentration of aqueous silica due soluble silica of the glass vessel, which caused a decrease in the value of zeta potential.

Quast [26] studied the effects of solution aging on the zeta potential characteristics of hematite. The isoelectric point of the mineral was measured as 2.6 under standard conditions. The aging time (11 days) of the hematite in plastic vessels increased the isoelectric point to 4.8, whereas storage in glass decreased the isoelectric point to 2.5. This decrease in isoelectric point was associated with the result of the adsorption of aqueous silica, possibly as a result of its leaching from the glass at normal values of pH. The increase in the isoelectric point of hematite can be explained by interactions of hydroxyl groups with the particle surface. The hydration result in hydrogen bonding between neighboring hydroxyl groups. Thus, the isoelectric point values for oxides become more basic with hydration.

Agglomeration of nanoparticles harms the advantages associated with their intrinsic nanometric size by affecting the final properties of the material, however, some synthesis conditions allow minimizing this effect of agglomeration.

### **2.2.2. pH**

In order to avoid agglomeration, the pH of the solution should be the one that causes the maximum zeta potential (positive or negative value) and in this way, promotes the repulsion of the particles. However, it is important to note that the addition of some solutions such as NaCl or HCl, used to change the pH of the solution, affects the ionic medium. As discussed before, the solvation process will

occur and increase the ionic strength of the solution, causing a decrease in zeta potential. Thus, the formation of mixed products can be minimized by keeping the pH constant during the synthesis by controlling the pH with acid or bases or even using a simultaneous addition of reactants [27].

### 2.2.3. Surfactant addition

Several reports relate the addition of a surfactant as a tool for more controllable synthesis of nanostructures and improvement of their dispersion state [28-29].

Surfactants are amphiphilic molecules, i.e., they have in their chemical structure two distinct parts: a polar, hydrophilic, head and a nonpolar, hydrophobic, tail. The surfactants adsorb on the surface of the nanoparticles with the polar side, thus, the nonpolar side is directed to the solvent. Therefore, the new apparent surface of the nanoparticle is nonpolar. Depending on the charge that polar groups acquire when surfactants are dissociated in water, there are four classes of surfactants: nonionic, zwitterionic, anionic, and cationic (Figure 10).

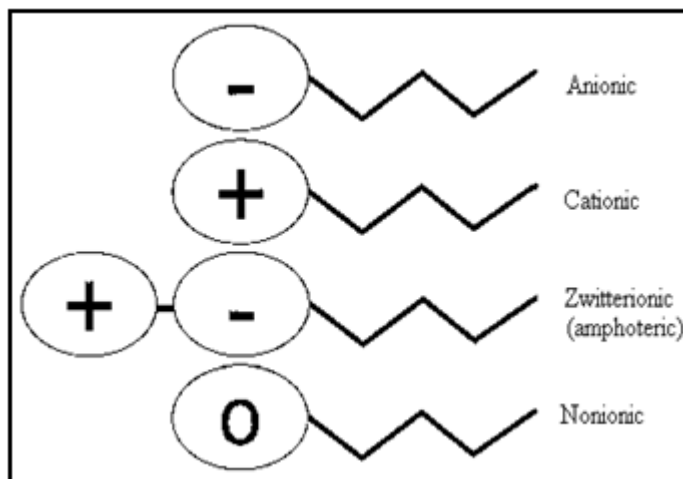


Figure 10: Schematic illustration of different types of surfactants [30]

- Anionic surfactant: the surface-active portion of the molecule bears a negative charge, for example,  $\text{RCOO}^-\text{Na}^+$  (soap);

- Cationic surfactant: the surface-active portion of the molecule bears a positive charge, for example, cetyltrimethylammonium bromide (CTAB);
- Zwitterionic (amphoteric) surfactant: both positive and negative charges may be present in the surface-active portion, for example,  $\text{RN}^+\text{H}_2\text{CH}_2\text{COO}^-$  (long-chain amino acid);
- Nonionic surfactant: the surface-active portion bears no apparent ionic charge, for example,  $\text{R}(\text{OC}_2\text{H}_4)_x\text{OH}$  (polyoxyethylenated alcohol).

The principle of surfactant modification is the preferential adsorption of the surfactant polar group on the high-energy surface of nanoparticles through electrostatic interactions [17]. Thus, agglomeration may be reduced as the addition of surfactant decreases the surface energy of the nanoparticles, therefore, surfactants may decrease interactions between nanoparticles. In addition, the surfactants cause steric repulsion which is dependent of the polymer macromolecule size. If two particles, each one covered by an adsorbed surfactant layer with thickness  $\delta$ , approach a separation distance lower than  $2\delta$ , the particles will be repelled due to the strong repulsion of the chains.

#### **2.2.4. Aging time**

Jalilpour and Fathalilou [31] studied the effect of aging time and calcination temperature for  $\text{CeO}_2$  nanoparticles synthesized via the reverse co-precipitation method. The suspensions were aged at room temperature for 1, 6, and 12 h and after that, were centrifuged to collect the precursor. The precursors were washed 3 times with distilled water and ethanol. The precursor was dried at 80 °C for 12 h and calcined at 600 and 800 °C for 2 h to obtain  $\text{CeO}_2$  nanoparticles. The authors concluded that an increase in aging time forms larger crystallite sizes and smaller particle sizes, thus less agglomerated powder.

On the other hand, Azlina et al. [32], synthesized  $\text{SiO}_2$  nanostructures using the sol-gel method. The range of aging time studied was 2, 4, and 6 hours. The

colloidal sol then was centrifuged and washed with ethanol and centrifuged again. The precipitate was dried at 60 °C for 1 day. The authors also studied the calcination temperature between 600 °C and 700 °C at a holding time of 1 hour and 30 minutes to produce the silica nanopowder. The results are shown in Table 2:

Table 2: Average size of silica nanoparticles

Calcination Temperature (°C)	Aging Time (h)		
	2	4	6
600	± 79.68	± 147.6	± 156.7
700	± 87.35	± 153.9	± 162.9

The results show that by tripling the aging time, the particles double in size. It was also observed that raise in calcination temperature promotes the increase in particle size. This effect was also observed by Marzano et al.[33].

The aging parameter is still very controversial and deserves to be further explored.

### 2.2.5. Temperature of crystallization

Regarding the synthesis of thermomiotic ceramics focused on  $Y_2W_3O_{12}$ , Pontón et al. [34] studied the co-precipitation by mixing reactants and developed the modified reverse co-precipitation method to synthesize  $Y_2W_3O_{12}$ , since sodium tungstate solution plays also the role of the basic solution instead of a precipitating agent as occurs in the common reverse co-precipitation. The methodology followed by these authors for the modified reverse co-precipitation method was to add, under gentle stirring, an aqueous solution of yttrium nitrate to sodium tungstate, with the same molarity. The pH at the beginning of the co-precipitation was approximately 8 and at the end of the co-precipitation, the pH of the final suspension was around 6.5. Therefore, the pH was not preserved during the co-precipitation, since there was precipitation of the  $OH^-$  and therefore a pH reduction of it in the solution. At the end of precipitation, the precipitate was washed, followed by vacuum drying. In order to crystallize this amorphous precipitated powder, it was calcined at 640

°C for 0.5 h. Submicronic powders in the range of 0.60–0.70  $\mu\text{m}$  were synthesized. The authors concluded that the calcination process causes the formation of necks, resulting in hard agglomerates.

Marzano et al. [33], synthesized  $\text{Y}_2\text{W}_3\text{O}_{12}$  submicronic powders through modified reverse strike co-precipitation keeping the pH nearby 10, which is an advantage in comparison with the procedure proposed by Pontón et al. [34] once, at pH=10, the solubility product ( $K_{\text{sp}}$ ) of the co-precipitated precursor was highly exceeded. The primary particle size was around 100 nm on average, however, agglomerated. The addition of CTAB to amorphous aged colloidal suspension assisted in the dispersion of the agglomerates, lowering agglomeration (mean agglomerate size around 500 nm) due to the electrostatic and/or steric stabilization, although in the specific case of  $\text{Y}_2\text{W}_3\text{O}_{12}$  it mainly acts as a dispersant during calcination process when volatilized. The authors suggested also for small calcination temperature variations, *p.ex.* an increment of 15 °C on calcination temperature, which did not change the average crystallite size, however, increased ~ 20% the average size of the agglomerates. The authors found promising results once surface-modified nanoparticles are less likely to agglomerate and may be more evenly dispersed.

It proves that the choice of calcination temperature is very important to avoid the formation of hard agglomerates.

### **2.3. Co-precipitation method**

A homogeneous solution after achieving the supersaturation level, i.e., a solid phase is formed after the limit of saturation is overcome or the conversion of the soluble substance into an insoluble form is defined as precipitation. The supersaturation can be achieved by changing the pH or the temperature of the solution [35].

The precipitation process is normally related to the appearance of insoluble particles from a solution while co-precipitation, although a type of precipitation, is a method that normally involves the precipitation of one or more metals in the form of hydroxide from a salt precursor with the assistance of a base in a solvent [27,36]. Afterwards, the product is removed from the solution through a precipitate (mostly

done by filtration) and labeled as a precursor [37]. Across the co-precipitation method, there are a lot of factors such as mixing and stirring which have a great influence on the dispersion and allow better control of the agglomeration of primary particles that impact the final particle size [27].

Additionally, the crystallization from solution, i.e, the process in which a solid is obtained after precipitation is in a crystalline form, normally occurs in a low supersaturation, promoted due to the reduction of the temperature or evaporation of the solvent during the synthesis. In contrast, precipitation frequently is related to high supersaturation as it promotes higher nucleation rather than crystal growth, which implies the precipitation of highly dispersed materials [27]. Therefore, it is very common to achieve an amorphous precursor by co-precipitation route, although it can be converted to a crystalline phase after subsequent aging [27,37]. Consequently, co-precipitation often comprises the following sequence: precipitation, filtration, washing, drying, and calcination step [27].

Co-precipitation reactions involve the stages of nucleation, growth, coarsening, and/or agglomeration processes. The co-precipitation process involves three main stages, in accordance with LaMer theory:

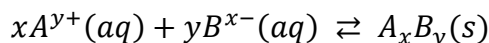
- Embryo formation;
- Homogeneous nucleation of stable nuclei;
- Growth of stable nuclei.

Despite the co-precipitation in most cases is reflected as homogeneous nucleation [35], as described above, in practice, this event is very difficult to occur as the nucleation normally is induced by seeds of solid material or by impurities causing heterogeneous nucleation [37].

The interaction between ions and molecules in the solution forms the embryos, which can grow or dissolve. Only those embryos that reach a size by the addition of monomers equal to or larger than the critical radius can grow as stable nuclei, and this occurs when they overcome the activation energy barrier. The activation energy barrier is related to the supersaturation state reached before the nucleation and crystal growth stages.

The equilibrium between the product and its reagents is expressed by the solubility product constant,  $K_{sp}$ . Assuming the reaction below (Equation 8),  $K_{sp}$  is given by Equation 9:

Equation 8: Example of a general reaction



Equation 9: Solubility product constant,  $K_{sp}$

$$K_{sp} = (A)^x(B)^y$$

The supersaturation can be expressed by Equation 10:

Equation 10: Supersaturation

$$S = \frac{C}{K_{sp}} = \frac{C}{C_s}$$

When a maximum supersaturation is reached at a specific temperature in the closed system, it begins to decrease over time approaching the equilibrium state. This behavior can be understood through the LaMer diagram (Figure 11).

LaMer theory explains the formation kinetics of particles, which describes the rate of the precursor concentration varying with time [37]. When the concentration of the precursor solute,  $C_s$ , increases to the critical nucleation concentration exceeding this limit,  $C_{min}$ , the system reaches the nucleation stage, resulting in rapid homogeneous nucleation, thus, promoting the start of precipitation. New particles are formed while the concentration of precursor is kept above  $C_{min}$ . However, when the concentration decrease below the  $C_{min}$ , due to the consumption of precursors by nucleation or due to the growth process, the only process that is prevalent is the particle growth of existing particles [37].

As supersaturation increases, it causes a nucleation rate that is faster than the growth rate of the precipitated particles (Figure 11). This occurs since the nucleation rate ( $B$ ) for homogeneous nucleation depends exponentially on

saturation level (S) (Equation 11). Therefore, carefully analyzing Equation 11, the nucleation rates depend on the concentration of reactants and temperature during the synthesis.

Equation 11: Dependence between nucleation rate and supersaturation

$$B = Ke^{-\left(\frac{16\pi\sigma^3 M^2}{3(kT)^3 \rho^2 N^2 \ln^2(S)}\right)}$$

$\sigma$ : interface energy between solid and liquid surface

M: molecular weight of the solid

$\rho$ : density of the solid

N: Avogadro constant

S: supersaturation ratio;

k: Boltzmann constant

T: absolute temperature

K: a constant (function of temperature and supersaturation)

The supersaturation is the driving force of nucleation and also for crystal growth as shown by Equation 12 [38].

Equation 12: Growth rate (G)

$$G = k_g S^g$$

Where  $k_g$  is the rate constant of growth and g is growth order.

The nucleation and growth processes occur simultaneously, however, at different rates characterized by different inclinations. Although it is often agreed that for the formation of monodisperse crystals the nucleation and growth are events treated separately [27]. Thus, nucleation occurs faster than growth. In this way, increasing the concentration of solute raises the nucleation rate (asymptotically rate). In this way, a large number of precipitates with small sizes are formed. The nucleation rate increases exponentially with concentration (supersaturation), while the growth rate is approximately a linear function (Figure 12). Hence, high supersaturation levels promote more nucleation rather than crystal growth, and,

therefore, the formation of fine precipitates. The rate of nucleation decreases due to increased solute consumption until the end of the nucleation stage, so definitely the size control of these particles shall be done during the nucleation stage [35].

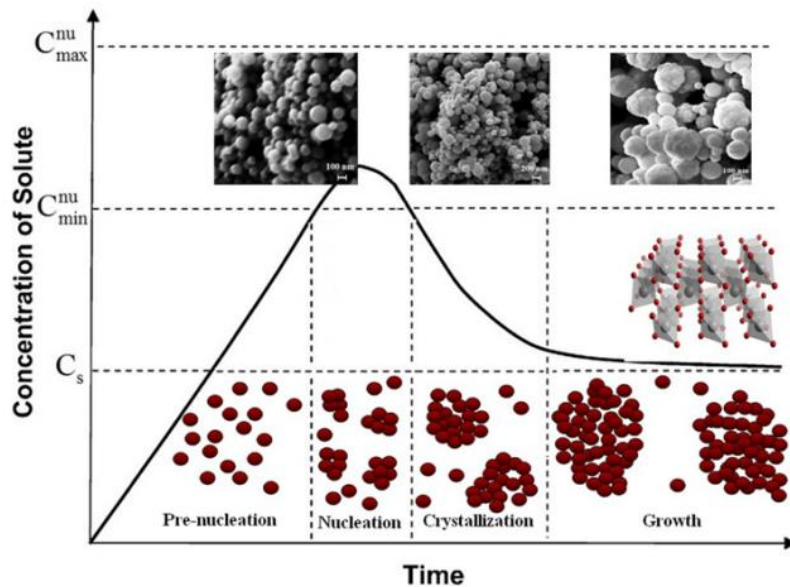


Figure 11: - LaMer diagram [39]

However, the permanence at a high supersaturation level above  $C_{min}^*$  (characterized by the gap of nucleation in Figure 11 and also in Figure 12 - curve B) should be avoided to generate monodispersed particles. The powders with a narrow particle size distribution are obtained in short nucleation, otherwise, the nucleation over a longer period results in a larger particle size distribution [37].

The particle size is a function of the peak area of the LaMer curve, that is, between the onset of the nucleation curve and the end of the nucleation threshold. It can be summarized that the final particle size is determined by the competition between nucleation and growth (and possibly also later steps, such as Ostwald ripening) [40].

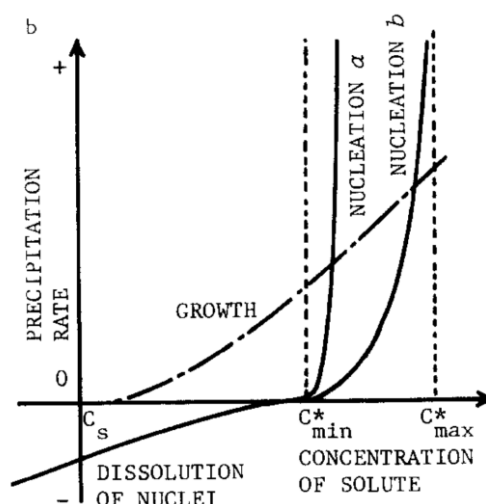


Figure 12: Diagram for precipitation rate as a function of solute concentration [41]

The supersaturation can occur through a precipitation agent (nitrates, carbonates, or ammonium) that changes the pH of the solution, leading to the formation of hydroxides or oxides. The precipitation must occur in such a way that the removal of the counter ions from the precursor salts and the precipitation agent are easily removed through the calcination process [40-41].

The formation of a particle is conducted by the free energy of agglomerates (embryo) of the constituents of the solution [37], which is better explained as follows. The classical theory of nucleation kinetics leads to Gibbs approach for homogeneous nucleation which uses the sum of surface energy and formation free energy for spherical nuclei of radius  $r_c$  [42]. During precipitation, there is a contribution of the difference between Gibbs free energies of solid and liquid phases ( $\Delta G_v$ ), i.e, the difference of the free energy between solution species and solid species [37], which is the driving force for phase transformation, and surface free energy ( $\gamma$ ) (Equation 13):

Equation 13: Total Free Energy Variation

$$\Delta G = -\frac{4}{3}\pi r^3 \Delta G_v + 4\pi r^2 \gamma$$

A solid sphere of radius  $r_c$  will have its free energy per volume ( $\Delta G_v$ ) increased when the energy of the same material is in bulk form (Equation 14):

Equation 14: Critical radius

$$r_c = \frac{2\gamma}{\Delta G_v}$$

It is well known that the liquid has a larger volume than the solid, therefore presenting greater freedom of movement of the atoms. These average atomic positions over time are completely random. However, considering an instant of determined time, it can be noted the presence of several atomic agglomerates (embryo) in the liquid with a compact organization similar to that of a crystalline network.

The average number of spherical embryos ( $n_r$ ) is given by Equation 15:

Equation 15: Number of spherical embryos

$$n_r = n_0 \cdot \exp\left(-\frac{\Delta G_r}{KT}\right)$$

Where  $\Delta G_r$  is the energy associated with the embryo and  $n_0$  is the number of atoms in the system.

As  $n_r$  decreases with increasing  $\Delta G_r$ , which increases rapidly with  $r$ , the probability of finding an embryo decreases as its size increases.

Similarly, the number of stable nuclei can be expressed by Equation 16:

Equation 16: Number of stable nuclei

$$C^* = C_0 \cdot \exp\left(-\frac{\Delta G^*}{KT}\right)$$

Where  $\Delta G^*$  is the energy needed for homogeneous nucleation.

The size distribution of nanoparticles depends on the growth process of the nuclei which includes the diffusion and adsorption of growth species onto the growth surface. If the concentration of growth species decays below the  $C_{\min}$ , the nucleation process finishes while the growth process continues.

Diffusion is an important factor to be considered during crystal growth since the molecules have to diffuse through the solution to get adsorbed on the growing crystal boundary [43]. The particle growth is related to diffusion or interface controlled by Ostwald ripening, which was treated first by Lifshitz and Slyozov [44]. The authors studied the kinetics of precipitation from supersaturated solid solutions. In a supersaturated solid solution occurs the diffusion effect, where a mass transfer will occur from a region that has high chemical potential migrating to another region with lower chemical potential. The dispersion particle in a matrix

increases the overall energy of a system due to the interfacial energy. Once the system ever desires to minimize its energy, the induced way to achieve this, is to reduce the number of particles to decrease the excess of energy due to the interfaces [45].

$C_\infty$  is the concentration of the saturated solution and  $\alpha = (2\sigma/kT)vC_\infty$ , is the parameter that contains the surface tension  $\sigma$  and the atomic volume of solute is  $v$ . The equilibrium concentration,  $C_R$ , at the boundary of a particle is related to the particle radius by Equation 17:

Equation 17: Relationship between equilibrium concentration and precipitate radius

$$C_R = C_\infty + \frac{\alpha}{R}$$

If the degree of supersaturation is very small and for extended annealing times (Lifshitz and Slyozov analysis), it can be approximated by  $C - C_\infty = \Delta$ . In this way, the diffusion is given by Equation 18:

Equation 18: Diffusion current of solute

$$\begin{aligned} &= D \left. \frac{\partial C}{\partial r} \right|_{r=R} = \frac{D}{R} (C - C_R) = \frac{D}{R} \left( \Delta + C_R - \frac{\alpha}{R} - C_R \right) = \frac{D}{R} \left( \Delta - \frac{\alpha}{R} \right) \\ J &= D \left. \frac{\partial C}{\partial r} \right|_{r=R} = \frac{D}{R} \left( \Delta - \frac{\alpha}{R} \right) \end{aligned}$$

If the precipitate radius changes over time, it can be described with the following Equation 19:

Equation 19: Radius of the precipitate varying with time

$$\frac{dR}{dt} = \frac{D}{R} \left( \Delta - \frac{\alpha}{R} \right)$$

In this way, for each supersaturation value, there will be a critical radius in equilibrium with the solution. If  $R > R_c$  the particle grows, if  $R < R_c$  it dissolves, even if for a solid solution this solution can be applied to any medium in which diffusion occurs.

As growth and nucleation rates decline, the Gibbs–Thomson effect (Equation 20) becomes significant so that smaller nuclei dissolve and transfer their mass to larger nuclei that grow. When smaller nuclei minimize their critical nucleus size, they become thermodynamically unstable and spontaneously dissolve in the solution again. It was illustrated as phase 4 in Figure 11, following the growth.

Equation 20: Gibbs-Thomson

$$\Delta G_\gamma = \frac{2\gamma V_m}{r}$$

where  $V_m$  is the molar volume of the phase.

This phenomenon is better explained through Ostwald ripening which describes the phase transformation that occurs from the species which are more thermodynamically unstable and then converted into more stable phases [46-47]. Ostwald ripening (Figure 13) occurs through the dissolution of small particles and simultaneous re-precipitation in regions whose particles are larger in size, i.e. the largest radius of curvature. This occurs in order to reach a more thermodynamically stable state wherein the surface to area ratio is minimized [48-49].

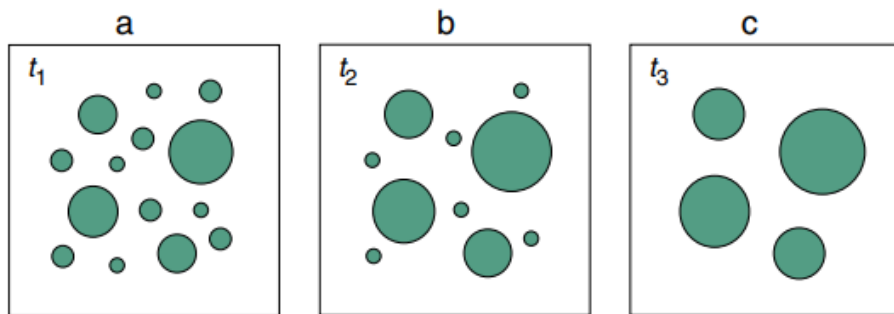


Figure 13: Ostwald ripening effect [50]

The driving force for Ostwald ripening is the difference in chemical potential of the material, caused by the difference in curvature, and can be expressed as Equation 21[51].

Equation 21: Ostwald ripening rate ( $\omega_T$ )

$$\omega_T = \frac{8\gamma C_w^{eq} D_w V_m}{9kT}$$

Where  $\gamma$  is the interfacial tension,  $V_m$  is the molecular volume,  $C_w^{eq}$  is the solubility,  $D_w$  is the diffusivity of the molecule,  $k$  is the Boltzmann constant and  $T$  is the absolute temperature. The Ostwald ripening rate  $\omega$  is directly proportional to the interfacial tension  $\gamma$ , in this way, reducing  $\gamma$ ,  $\omega$  is reduced.

Soma and Papadopoulos [52], confirmed this by measuring  $\omega$  as a function of an anionic surfactant sodium dodecyl sulfate (SDS) concentration for decane-in-water emulsion below the critical micelle concentration (CMC). The interfacial tension showed a linear decrease with an increase in  $\log$  [SDS] concentration (Table 3).

Table 3: Concentration of SDS vs. Ostwald ripening rate

Concentration of SDS	“Undiluted” emulsions	“Diluted” emulsions
	Experimental rate $\omega_e$ , ( $m^3 s^{-1}$ )	Experimental rate $\omega_e$ , ( $m^3 s^{-1}$ )
0.0	$2.5 \times 10^{-24}$	-
$1.0 \times 10^{-4}$	$4.62 \times 10^{-25}$	$2.80 \times 10^{-25}$
$5.0 \times 10^{-4}$	$4.17 \times 10^{-25}$	$2.56 \times 10^{-25}$
$1.0 \times 10^{-3}$	$3.68 \times 10^{-25}$	$2.30 \times 10^{-25}$
$5.0 \times 10^{-3}$	$2.13 \times 10^{-25}$	$1.61 \times 10^{-25}$
$1.0 \times 10^{-2}$	$2.06 \times 10^{-25}$	$1.59 \times 10^{-25}$
$2.5 \times 10^{-2}$	$2.87 \times 10^{-25}$	$2.38 \times 10^{-25}$
$5.0 \times 10^{-2}$	$3.64 \times 10^{-25}$	-

Although nucleation and growth models provide simplified ideas of particle formation from solution, it is mostly applied to a single phase formation and disregards the agglomeration processes which corroborates the formation of less quantity of particles and larger in size [37]. The decrease of agglomeration to develop a more uniform distribution of the final particle size can be reached by

mechanical agitation or other processes which leads to the fragmentation of growing crystals [37].

The parameters with a great influence on precipitation processes and consequently in the as-synthesized powder are described in Figure 14.

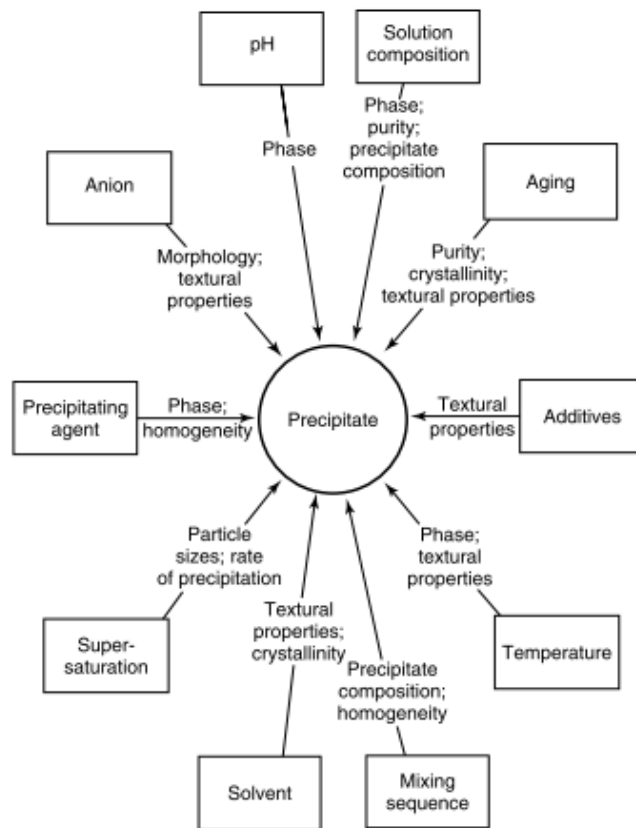


Figure 14: Properties of the precipitate and the referred parameters that affect its characteristics. [37]

Although several factors directly affect precipitation, as previously reported, the main problem of co-precipitation is related to the agglomeration of nanoparticles (primary particles) in hard micron-sized agglomerates (secondary particles) which mostly is related to physical or chemical forces between particles [27,36].

Chapters 4 and 6 address in more detail, at least, the following aspects related to precipitation:

- Supersaturation: Driving force of the precipitation
- Temperature: Nucleation rate is dependent on the temperature and impacts the particle sizes

- Additives: Surfactant addition can stabilize small particle sizes
- Aging: Particle sizes can increase due to Ostwald ripening during the aging time or even leads to crystallization without the calcination step (while the solid is in the mother liquor)
- pH: To control the degree of supersaturation

## 2.4. Sol-Gel method

The main advantage of the sol-gel method is that the formation of a precursor gel allows a very homogeneous stoichiometrically favorable atomic mixture with smaller interatomic distances facilitating diffusion. The sol-gel method requires lower temperatures and reaction times being a synthesis route that is classified as low energy one.

Sol-gel processes may be divided into traditional (aqueous route) or non-hydrolytic. Traditional sol-gel routes include the hydrolysis (Equation 22) and condensation (Equation 23) of alkoxide precursors to form an oxide network directly from a solution (see Figure 15).

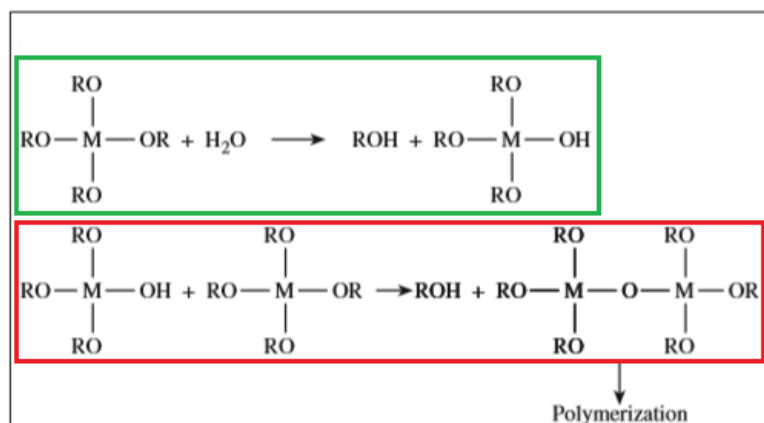


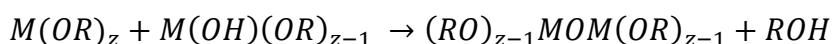
Figure 15: Schematic showing hydrolysis reaction (in green ) and condensation reaction (in red) [35].

Equation 22: Hydrolysis reaction



Alkoxides  $M(OR)_z$  are compounds with metal or semi-metal atoms (M) and alkoxy groups (OR) as ligands. In the sol, the dispersion medium is a liquid (such as water, for an aqueous route, or alcohol/ether for NHSG route) and the dispersed phase is a solid (alkoxide) which mixture appearance is a liquid. The addition of water is followed by a proton transfer, forming an alcohol molecule (ROH) which is eliminated during the hydrolysis reaction.

Equation 23: Condensation reaction



The alkoxy groups ( $-OR$ ) of the condensation product can be hydrolyzed further to form a cross-linked, three-dimensional network of metal-oxygen bonds.

This technique is well-established for the preparation of metal oxides in various forms, such as xerogels, aerogels, micro/nanoparticles, fibers, thin films, etc. There are two ways to prepare sol-gel [53]:

- Inorganic method: formation of a colloidal suspension (usually oxides) and gelation of the sol (colloidal suspension of very small particles (1–100 nm)) to form a network in a continuous liquid phase.
- Organic method: solution of alkoxide precursors,  $M(OR)_n$ , in an alcohol or other organic solvent, where M is usually metal and R is an alkyl chain.

These reactions between metal alkoxides dissolved in alcohol and small amounts of water in organic solvents lead to the hydrolysis process. In this process, the breakdown of the metal-oxygen bond is the limiting step in the reaction rate, resulting in significantly different kinetics of hydrolysis for different metal alkoxides, once the reaction rate increases as the increment of the difference in the electronegativity of the metal [1,53].

As the hydrolysis reaction occurs, there may also be condensation (any condensation reaction, of a monomer having two functional groups, which process allows the production of polymers) where the M-OH alkoxide molecules can react

with other M-OH species by removing water or react with the M-OR group to produce an alcohol molecule. The hydrolysis and condensation steps lead to the formation of the polymeric network (gel).

The hydrolysis rates of the precursors are very important once for different precursors this rate can be different and form inhomogeneities of the gel. This kind of problem can be minimized if the less reactive component is added before the addition of the more reactive precursor. For alkali metals and alkaline earth metals, it is complicated to use alkoxides because they are difficult to prepare. In these cases, some reactants such as acetates and citrates, which are soluble in organic solvents, are a viable alternative [35].

Although expensive, this technique can produce powders with a high surface area (small particle size), which allows during the sintering process high density at much lower temperatures when compared to other techniques [35]. However, some variables in the sol-gel process impact the final product such as the type of alkoxide, reaction temperature, and the amount of water added that influence the gelation times vary from seconds to several days.

The conversion of sol to gel (gelation process) occurs via hydrolysis and condensation reactions (increasing the viscosity due to the formation of a three-dimensional network) while the conversion of gel to oxide occurs via drying (loss of water and alcohol) and calcination (Figure 16) [35].

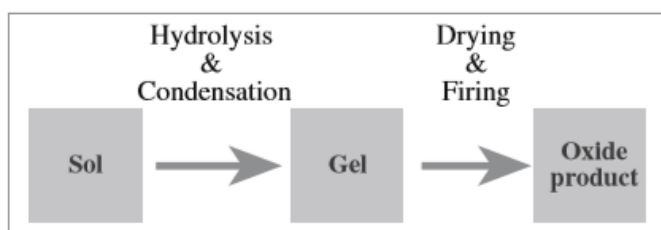


Figure 16: Three general steps in the sol-gel process [35].

A drying step of a wet gel into a dried one is represented in Figure 17, where  $dW/dt$  = drying rate,  $\Delta l/l_0$  = relative deformation,  $P/P_s$  = relative vapor pressure, and  $F$  = capillary force.

1. Stage I: gel volume decreases in a constant drying rate period.

2. Stage II: competition between capillary forces and deformation due to the resistance of gel framework.
3. Stage III: the appearance of the hysteresis from relative vapor pressure due to the non-uniform pore geometries, which lead to differences in adsorption and desorption isotherm of water by the gel with decreases in drying rate. Firstly, the water is removed from the large pores once the small pores show a slow drying rate [54].
4. Stage IV: the final stage of drying represents the evaporation of remaining water from contact points between the particles, increasing the action of capillary forces again.

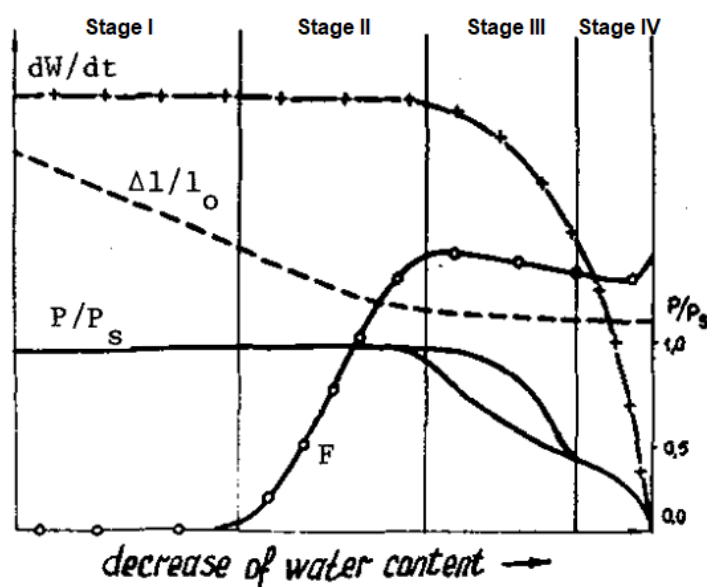


Figure 17: Stages of drying (figure adapted from Fig.6 in Ref [55]).

The aerogels have lower densities than xerogels due to the replacement of the liquid phase of a gel with gas through supercritical drying forming pores through the network connection. The aerogel presents a shrinkage  $< 15\%$  while a xerogel is obtained when the liquid phase of a gel is removed by evaporation (shrinkage  $> 90\%$  that is experienced while being dried). This porosity of the aerogels makes them good candidates to be applied in thermal insulation. On the other hand, the drying process for xerogels occurs slowly, and the chain has time to restructure and densify, minimizing their porosity as shown in Figure 18 [56].

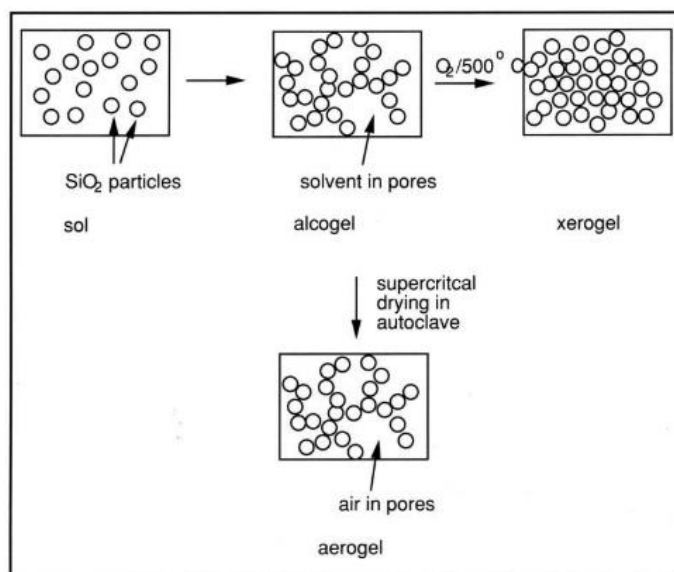


Figure 18: Sol-Gel drying process [56].

The gel structure can be classified as a network of colloidal particles or polymeric gel, which uses an array of polymeric chains. The last one is the most common methodology applied to ceramics.

The growth of particles in the sol-gel process follows nucleation and aggregation, being dependent on the concentrations of reagents since they are affected by the rate of hydrolysis and condensation reactions. Jafarzadeh et al. [57] studied the synthesis of silica nanoparticles by sol-gel method analyzing the effect of experimental parameters on the particle size and the influence of the mixing mode. The authors proposed different mixing modes of the reactants as follows:

- Mode-A: TEOS (tetraethyl orthosilicate) was firstly dissolved in ethanol for 10 min, and then water was added to the reaction medium.
- Mode-B: TEOS, EtOH, and  $\text{H}_2\text{O}$  were mixed at the same time.
- Mode-C:  $\text{H}_2\text{O}$  + EtOH (mixed for 10 min, then TEOS was added to the mixture).

The average particle size was found to be  $10.6 \pm 1.4$ ,  $13.8 \pm 1.7$ , and  $14.9 \pm 1.6$  nm for Mode-A, B, and C, respectively. Although the low difference between the results, it was demonstrated that the mixing mode of reactants during synthesis preparation affects particle size. The TEOS is immiscible in water, but dissolves

easily in ethanol showing a high homogeneity among TEOS and ethanol, and consequently, better results for mode A. In the other modes (B and C) due to the low homogeneity of TEOS molecules in the mixture of water and ethanol, the growth of nanoparticles was increased.

When silica particles were prepared at the same conditions but with different feed rates of ammonia (0.01, 0.02, and 0.03 mL min<sup>-1</sup>), the rate affected the particle size of silica obtained via freeze drying (10.6 ± 1.4, 11.4 ± 1.7 and 15.0 ± 1.6 nm, respectively). Although there is not so much difference between the results, it can be seen a tendency to increase the particle size according to the increase of the feed rate. Thus, smaller silica nanoparticles can be obtained decreasing the feed rate of ammonia.

However, in the presence of hydrolysis as the rate-limiting step, the model proposed by Matouskas and Gulari [58] based on monomer-addition growth in a slow hydrolysis rate, only the hydrolyzed monomers are available for nucleation, therefore, the slow release of the monomer acts as a mechanism that inhibits nucleation and, therefore, it promotes the growth of large particles. As the feed rate of reactant is increased, enhanced the rate of hydrolysis, which increases the concentration of hydrolyzed monomer that lead to a higher nucleation rate. In this case, small particles should be formed as observed in previous studies [59].

There are reports on the synthesis of nanostructured mesoporous oxides using surfactant as an assisted pathway to synthesize nanoparticles. Shadiya et al [60]. studied via a one-step sol-gel method using PVA as the polymeric surfactant to synthesize nanoparticles of zirconia powder. The authors investigated varying the conditions such as concentration of PVA and calcination temperatures, to compare the zirconia formed during each condition at a constant molar ratio of reactants. The conclusion was that PVA assisted the formation of nanoparticles with particle size distribution analyzed by dynamic light scattering (DLS).

Sivakumar et al. [61], synthesized by sol-gel method of the spinel ferrites using metal nitrates as precursors and PVA as surfactant. The authors confirmed that the ranges of crystallite size (verified through histograms) were reduced with the increment of PVA concentration. The result of HR-SEM (High-resolution scanning electron microscopy) images shows that the particle size was reduced, achieving an optimum PVA concentration of 9 wt. % from the method.

Siwinska-Stefanska et al. [62], verified that in the sol-gel method,  $\text{TiO}_2$  was obtained with the addition of acetylacetonate (AcAc), used as a stabilizing agent to control the rate of hydrolysis and condensation of the metal alkoxide, decreasing the agglomeration and the diameter of particles. The large distribution of particle size in  $\text{TiO}_2$  sols is due to the uncontrolled hydrolysis - condensing reacting rate. Thus, as AcAc reacts easily with the metal alkoxide, the reactivity of the alkoxide with chelating agents is a way to control the hydrolysis-condensing behavior of alkoxide [63].

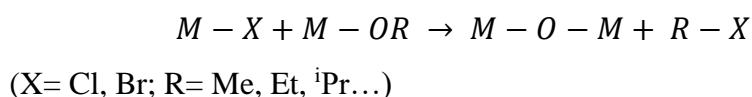
## 2.5. Non-hydrolytic Sol-Gel

The non-hydrolytic sol-gel (NHSG) process has versatility in the preparation of inorganic oxides as it involves reactions between a metal halide with an oxygen donor, such as alcohol or ether to form an alkoxide in the absence of moisture, with subsequent formation of inorganic oxide [64]. NHSG is a feasible improvement to non-aqueous synthesis conditions using other oxygen resources instead water based on the condensation of metal chlorides with metal alkoxides for the synthesis of metal oxides. In this way, the M–O–M bonds are formed under the elimination of organic molecules, without a hydrolysis step, and the oxygen is provided by alcohols, ethers, or metal alkoxides. Thus, as the reaction rates settle, very atomic homogeneous dispersions of metal cations in mixed oxides are obtained and the samples can be crystallized at lower temperatures [65].

However, there are some reports [65-67] that describe the production of water content in-situ, such as the reactions between carboxylic acids with tetraalkoxysilane and alcohols, or acetone with metallic chlorides. To investigate in-situ water production, it can be measured by Karl Fisher (KF) titration which method consists of the oxidation reaction between iodine and sulphur dioxide. There are two primary methods of KF titration, denoted volumetric [68] and coulometric [66,69]. Therefore, non-hydrolytic sol-gel methods can be divided into two groups: reactions that have the participation of M–OH groups or not. If M–OH groups are not present, the results are strictly anhydrous conditions (no water contains) and the condensation reactions follow below [70].

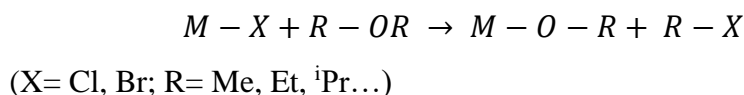
The alkyl halide elimination (Equation 24) is the reaction of condensation between alkoxide and metal halide (usual chloride) is the first NHSG reaction studied and one of the most useful for the synthesis of mixed oxides [53]. It is important to highlight that there are three subtypes of alkyl halide elimination reactions depending on the oxygen donor used: alkoxide, ether, or alcohol [65]. Nonetheless, the reactions conducted by an aprotic condensation reaction between metal chlorides and isopropyl ether, it is classified as a strictly non-hydrolytic reaction, without the formation of water content in-situ [66].

Equation 24: Alkyl halide elimination reaction

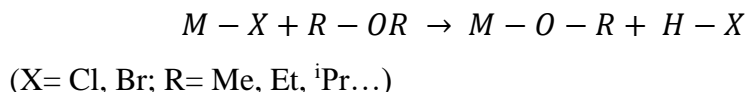


The alkyl halide elimination can occur in two different ways (Equation 25 and Equation 26). Equation 25 is classified as an ether route (with metal chlorides and ethers as precursors, thus, the alkoxide group is formed in situ.

Equation 25: Metal alkoxide group formed in situ by reaction of metal chloride with ether



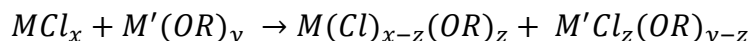
Equation 26: Metal alkoxide group formed in situ by reaction of metal chloride with primary/secondary alcohols



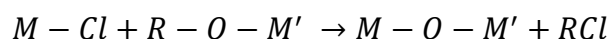
Ligand exchange occurs between metal halides and alkoxides before condensation reaction (Equation 27). Hence, metal chloroalkoxides are the precursors of NHSG condensation [65]. The homogeneity is strictly dependent on the kinetics of heterocondensation (Equation 28) and homocondensation (Equation 29) while the kinetics of the hetero/homocondensation reactions is dependent on the type of the metal precursors and therefore the homogeneity of the products are variants. Extremely homogeneous samples are synthesized if the rate of

heterocondensation of M and M' (Equation 28) is equivalent or higher than that of homocondensation (Equation 29) [65].

Equation 27: NHSG redistribution reaction



Equation 28: NHSG heterocondensation reaction



Equation 29: NHSG homocondensation reaction



Mahandrimanana et al. [71], synthesized aluminum titanate gels by NHSG reaction. Due to the redistribution reactions, the condensation rates have been achieved leading to highly homogeneous gels. The authors observed a metastable  $\beta$ -Al<sub>2</sub>TiO<sub>5</sub> phase during the calcination at 850 °C, thus, the NHSG is very suited to the preparation of metastable compounds.

Arnal et al. [72], studied the NHSG route regarding the alkoxylation / condensation of TiCl<sub>4</sub> by diisopropyl ether and the condensation between TiCl<sub>4</sub> and titanium isopropoxide and concluded that in both cases the condensation is slow at room temperature although the oxide formation requires heating 80 - 150 °C. The authors concluded that the concentration of Ti(OiPr)Cl<sub>3</sub> is higher in the ether route than in the alkoxide route due the alkoxylation reaction which leads to a shorter induction time and gelling.

It is well established that NHSG can produce a very homogeneous material, comprising new and metastable phases, such as ZrTiO<sub>4</sub> [73] and M<sub>2</sub>MO<sub>3</sub>O<sub>12</sub> (M = Ga, Y, Sc, Fe, In, Al) [74-77].

Figure 19 presents the NHSG method from alkyl halide elimination reaction using ether as an oxygen donor to obtain nanopowders from the A<sub>2</sub>M<sub>3</sub>O<sub>12</sub> family, such as Al<sub>2</sub>W<sub>3</sub>O<sub>12</sub>. Diisopropyl ether has been notoriously identified as excellently appropriate for alkyl halide elimination in the ether route due to the high yields and high surface area [65]. Thus, the ether route is at present the most generally utilized for the metal oxides preparation in the NHSG route.

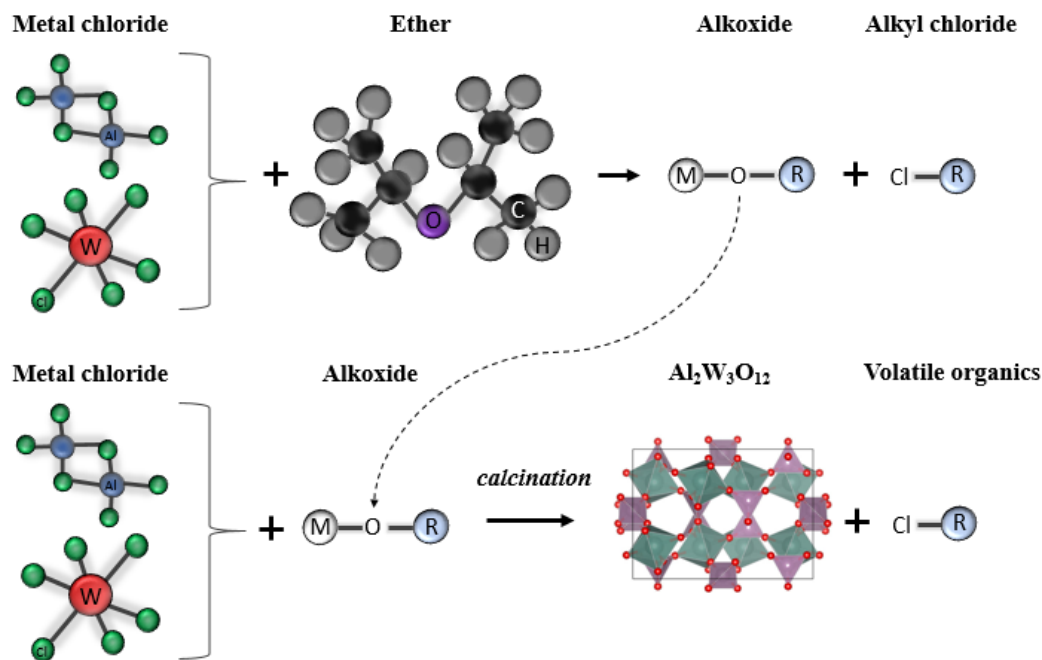


Figure 19: Schematic showing the NHSG route applied for  $\text{Al}_2\text{W}_3\text{O}_{12}$  phase.

In the last years, there is a particular group that developed large studies of new materials by NHSG approach [74-77]. Part of the study is concentrated on metal oxides classified as thermomiotics, with  $\text{A}_2\text{M}_3\text{O}_{12}$  stoichiometry (A = Al, Sc, Fe, In, Ga, Y, Mg-Zr, Mg-Hf; M = Mo or W) which shows negative thermal expansion. Most of those studies follow the alkyl halide elimination reaction regarding the ether route. For instance, based on the impact of solvent on the reactions, it has been shown that acetonitrile improved the homogeneity and lower crystallization temperatures (400 - 700 °C) compared to dichloromethane [65].

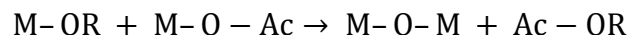
The ether elimination reactions (Equation 30) are characteristic of multivalent transition elements such as Mo, W, and Nb, for which the inorganic molybdate or tungstate are directly produced in the presence of alkoxides [53].

Equation 30: Ether elimination reaction



The ester elimination (Equation 31) has been used for the preparation of alkylsilyloxy derivatives of titanium, zirconium, niobium, and tantalum [53].

Equation 31: Ester elimination reaction



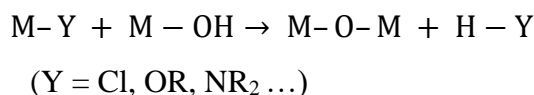
The reactions between acetoxysilanes and metal amides allow a high number of M–O–M bonds and dialkylacetamide as a volatile organic product (Equation 32) [65].

Equation 32: Acetamide elimination reaction

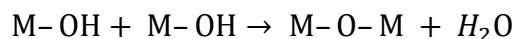


The reactions that involve M–OH groups are considered non-hydrolytic once the results come from heterocondensation reactions (Equation 33) rather than from M–OH self-condensation (Equation 34) [70].

Equation 33: Heterocondensation reaction



Equation 34: Self-condensation reaction



The high degree of condensation of nonhydrolytic gels that withstand well the capillary forces, formed by solvent during drying, allows the synthesis of mesoporous xerogels [78].

Gates et al. [77] synthesized Ga<sub>2</sub>Mo<sub>3</sub>O<sub>12</sub> for the first time using non-hydrolytic sol-gel. The authors prepared under argon in dried glassware, stoichiometric quantities of GaCl<sub>3</sub> (2 mmol) and MoCl<sub>5</sub> (3 mmol), and used distilled acetonitrile (10 mL) as solvent. Isopropyl ether (12 mmol) was added to the mixture as an oxygen donor. The sample was cooled in liquid nitrogen and sealed under a vacuum. The ampoule was heated at 130 °C for one week and after that, it was opened to air to evaporate the solvent. The sample was heated to 300 °C, and kept at this temperature for 3 h. As the sample was partially crystallized a second heat treatment was carried out for plus 3 h at 600 °C to crystallize the sample. In a conclusion, the authors succeeded to prepare monoclinic Ga<sub>2</sub>Mo<sub>3</sub>O<sub>12</sub> based on the

reaction of metal alkoxides with metal halides, or ethers with metal halides to produce the alkoxides. M–O–M linkages and alkyl halides are formed as the reaction proceeds.

Gates and Lind [76], also prepared  $Y_2Mo_3O_{12}$  by non-hydrolytic sol-gel. The authors used the same approach detailed in the previous paragraph. The contribution of this work was to demonstrate the existence of orthorhombic (Pba2 space group), a new  $Y_2Mo_3O_{12}$  polymorph obtained during heat treatments through annealing.

### 3. Objectives

#### 3.1 General objective

Development of soft chemistry routes for the synthesis of low agglomerated nanopowders of different  $A_2M_3O_{12}$ -type phases, with negative or near zero thermal expansion.

#### 3.2 Specific objectives

- 1) Synthesis of  $Al_2W_3O_{12}$  nanopowders via i) hydrothermal treatment ii) mixing reactants, evaluating the followings aspects regarding the deagglomeration of nanopowder:
  - Assess the effect of each method on the agglomeration state of the as-synthesized powders.
  - Study the impact of two crystallization methods, such as heat treatment (calcination) and hydrothermal treatment, on the agglomeration of the nanopowders.
  - Crystallization due to the aging time
  - Surfactant addition
  - Molarity
  - Study the effect of the calcination parameters on the agglomeration degree
  
- 2) Synthesis of  $Al_2W_3O_{12}$  by NHSG method (new route) evaluating:
  - The effect of the synthesis molarity and the calcination parameters regarding the size and agglomeration degree of powder.
  
- 3) Synthesis of  $ZrMgMo_3O_{12}$  nanopowders via (i) co-precipitation by mixing reactants; (ii) co-precipitation by dripping reactants and pH control  $\sim 9$  or (iii) co-precipitation by total evaporation route.
  - The main goal is to apply low energy synthesis approach to develop  $ZrMgMo_3O_{12}$  based on the co-precipitation method.

## 4.

### Comparison between different co-precipitation approaches for the synthesis of low-agglomerated $\text{Al}_2\text{W}_3\text{O}_{12}$ powders

#### 4.1

##### Background

Among  $\text{A}_2\text{M}_3\text{O}_{12}$  family members,  $\text{Al}_2\text{W}_3\text{O}_{12}$ , exhibits a low-positive linear thermal expansion coefficient ( $1.50 \times 10^{-6} \text{ }^\circ\text{C}^{-1}$ , from 25 to 800  $^\circ\text{C}$ ) [79-81], being attractive not only due to its peculiar CTE, but also by its relatively low cost and non-hygroscopic nature [10,79]. Commonly, materials from  $\text{A}_2\text{M}_3\text{O}_{12}$  family have been tested as thermal expansion regulator fillers of metal, ceramic and polymer matrixes. In spite of the fact that  $\text{Al}_2\text{W}_3\text{O}_{12}$  has only been used to reinforce few matrices, such as high-density polyethylene (HDPE) [82], polymethyl methacrylate (PMMA) [83], and  $\text{Al}_2\text{O}_3$ -toughened  $\text{ZrO}_2$  (ATZ) [84], it is a promising candidate for this application considering all its physico-chemical features [10,79,85].

As a filler,  $\text{Al}_2\text{W}_3\text{O}_{12}$  presents the advantage of its high Young's (E) and bulk moduli (K) of 92 GPa [82] and 48 GPa [86], respectively, in comparison to other family members of  $\text{A}_2\text{M}_3\text{O}_{12}$ , such as  $\text{Y}_2\text{W}_3\text{O}_{12}$  (E ~31 GPa [82] and K ~25 GPa) [87]. These elastic constants are of paramount importance to: i) increase the rigidity, and ii) decrease the CTE of composites, especially when polymer matrices are used [88]. Additionally, as advanced ceramic,  $\text{Al}_2\text{W}_3\text{O}_{12}$  has been proposed in the literature for thermal shock resistance applications in its monolithic form [10,79]. However, both applications demand the use of crystalline  $\text{Al}_2\text{W}_3\text{O}_{12}$  nanopowders with low agglomeration degree and high specific surface area, which have been the main motivations to develop new synthesis approaches [10,79,85]. Thus, one of the best candidates is the soft chemistry, also referenced as "*chimie douce*", which explores, through low energy synthesis conditions, the achievement of ceramic powders with low agglomeration of primary particles [49, 89-90].

There are several soft chemistry routes for the preparation of ceramic oxides, such as co-precipitation, hydrothermal synthesis, sol-gel, non-hydrolytic sol-gel,

total evaporation route, *etc.* In the case of Al<sub>2</sub>W<sub>3</sub>O<sub>12</sub> synthesis, some studies reported in the literature are summarized in Table 4, showing the specific surface area of the crystallized powders. Note that those works employed 0.1 M aqueous solutions, independently of the type of salt reactant.

Table 4: Different synthesis routes for the preparation of Al<sub>2</sub>W<sub>3</sub>O<sub>12</sub> powders

Synthesis route	Reactants <sup>(a)</sup>	Pre-calcination	Calcination Conditions	Post-calcination	BET <sup>(c)</sup> (m <sup>2</sup> g <sup>-1</sup> )	SEM or TEM <sup>(d)</sup> (nm)	Ref.
Total evaporation route	Al(NO <sub>3</sub> ) <sub>3</sub> .9H <sub>2</sub> O, (NH <sub>4</sub> ) <sub>6</sub> W <sub>12</sub> O <sub>39</sub> .xH <sub>2</sub> O	i) T <sub>1</sub> = 60 °C until total evaporation ii) T <sub>2</sub> = 80 °C for 12 h iii) Mild milling in an agate mortar	T= 750 °C t= 30 min	Ball milled for 8 min	9.6	50 - 100	[79]
Co-precipitation	Na <sub>2</sub> WO <sub>4</sub> + Al(NO <sub>3</sub> ) <sub>3</sub> , NH <sub>4</sub> OH	i) T= 80 °C <sup>(b)</sup> ii) Mild milling in an agate mortar	T= 800 °C t= 30 min	-	1.2	-	[85]
Normal strike co-precipitation	Al(NO <sub>3</sub> ) <sub>3</sub> .9H <sub>2</sub> O, (NH <sub>4</sub> ) <sub>6</sub> W <sub>12</sub> O <sub>39</sub> .xH <sub>2</sub> O, NH <sub>4</sub> HCO <sub>3</sub>	-	T= 750 °C t= 30 min	Ball milled for 98 min	7.7	-	[82]
Co-precipitation	Al(NO <sub>3</sub> ) <sub>3</sub> .xH <sub>2</sub> O, (NH <sub>4</sub> ) <sub>6</sub> W <sub>12</sub> O <sub>39</sub> .xH <sub>2</sub> O, NH <sub>4</sub> HCO <sub>3</sub>	-	T= 750 °C t= 30 min	-	2.1	-	[10]
Co-precipitation	Na <sub>2</sub> WO <sub>4</sub> .2H <sub>2</sub> O + Al(NO <sub>3</sub> ) <sub>3</sub> .9H <sub>2</sub> O	i) T= 80 °C for 5 h	T= 630 °C t= 5 h T= 830 °C t= 5 h	-	-	10 - 40 30 - 140	[91]
Solid-state reaction	Al <sub>2</sub> O <sub>3</sub> (p.a.) + WO <sub>3</sub> (p.a.)	i) Ball milled for 6h; ii) Ball milled for 6h	T= 930 °C t= 16 h T= 1050 °C t= 8 h	-	-	20 - 120 60 - 150	
Co-precipitation	Na <sub>2</sub> WO <sub>4</sub> .2H <sub>2</sub> O + Al(NO <sub>3</sub> ) <sub>3</sub> .9H <sub>2</sub> O	i) T= 80 °C for 5h	T= 630 °C t= 5 h T= 830 °C t= 5 h	-	-	10 - 40 25 - 140	
Sol-Gel	Al <sub>2</sub> O <sub>3</sub> (p.a.) + H <sub>2</sub> WO <sub>4</sub> (p.a.) + HNO <sub>3</sub> + (CH <sub>2</sub> OH) <sub>2</sub>	i) T <sub>1</sub> = 80 °C during gelatination ii) T <sub>1</sub> = 90 °C for 5 days ii) T <sub>1</sub> = 300 °C for 30 min, raised to 600 °C (rate of 150 °C/h)	T= 630 °C t= 36 h T= 830 °C t= 5 h	-	-	10 - 90 60 - 150	[92]

(a) Concentration of reactant aqueous solutions: (0.1 M)

(b) Time not specified

(c) Specific surface area evaluated through Brunauer-Emmett-Teller (BET) method

(d) Scanning Electron Microscopy (SEM) or Transmission Electron Microscopy (TEM) for primary particles

Despite the fact that the synthesis conditions described in Table 4 allowed achieving Al<sub>2</sub>W<sub>3</sub>O<sub>12</sub> powders with primary particles in the range of 50 - 200 nm,

the powders were highly agglomerated, as deduced by the reported specific surface areas, *i.e.*, hard micron-sized agglomerates (secondary particles) have been formed in those works due to physical or chemical forces acting between primary adjacent particles [10,79,82,85, 91-92]. Thus, the drawback to be overcome for the preparation of nanosized  $\text{Al}_2\text{W}_3\text{O}_{12}$  powders is to decrease the agglomeration degree among particles. This goes against thermodynamics since nanoparticles tend to agglomerate for minimizing surface energy and to reach a more stable thermodynamic state.

The fundamentals of co-precipitation are well established by LaMer theory which explains the formation kinetics of particles regarding the rate of the precursor concentration varying with time [37]. The precipitates originate from soluble species formed under conditions of high supersaturation, therefore, the supersaturation state is mandatory to induce precipitation during the synthesis. It is important to point out that the co-precipitation reactions involve the stages of nucleation, growth, coarsening, and/or agglomeration. Hence, in accordance with LaMer theory, the co-precipitation embraces: i) embryo formation, ii) homogeneous nucleation of stable nuclei, and iii) growth of stable nuclei.

Furthermore, the preparation of ceramic powders *via* co-precipitation comprises of the following steps: i) synthesis of an amorphous precursor, ii) washing, iii) drying of the as-synthesized powder, and iv) rapid and low-temperature calcination of the amorphous precursor powder to crystallize into the desired phase. During the calcination step, temperature and time are the main parameters that can induce the formation of agglomerates due to the necking between neighbors particles [33-34]. The conditions applied during each step described above can result in the increase or decrease of the final agglomeration state of the prepared powder. The parameters with a great influence on the co-precipitation processes, and consequently, on the as-synthesized powder comprises, but are not limited to, pH, the temperature of the synthesis, initial concentration of reagent solutions, and aging time [27,36,40]. In addition, the formation of multiphase products can be minimized by keeping the pH constant during the synthesis by controlling the pH, with acid or bases, or even using a simultaneous addition of reactants [27].

Likewise, the addition of surfactants in the reaction medium where the co-precipitation is carried out has been extensively applied [28-29,33,93] to reach

powders with lower agglomeration degree. The principle for using surfactants is based on the preferential adsorption of its polar group head on the surface of the co-precipitated oxide amorphous nanoparticles through electrostatic interactions with the hydroxyl groups of those nanoparticles [17]. Thus, agglomeration may be reduced as the addition of surfactant decreases the surface energy of the nanoparticles and steric hindrance.

Marzano et al. [33], synthesized  $\text{Y}_2\text{W}_3\text{O}_{12}$  by modified reverse strike co-precipitation in which sodium tungstate solution was used as a basic solution, inducing precipitation, instead of a precipitant agent as commonly applied for reverse strike method. After synthesis, the precipitate suspension was stored for an aging time of two weeks. After that, the suspension was mixed with a cationic surfactant diluted in water at 0.5 mM and 0.9 mM. The authors concluded that the addition of surfactant assisted the decrease of powder agglomeration due to the electrostatic and/or steric stabilization, principally due to the steric effect during the calcination process in which the surfactant was volatilized, acting as a dispersant.

On the other hand, Jalilpour and Fathalilou [31] studied the effect of aging time for  $\text{CeO}_2$  synthesized via the reverse co-precipitation method. The suspensions were aged at room temperature for 1, 6, and 12 h. The suspension was centrifuged and washed 3 times with distilled water and ethanol. The wet powder was dried at 80 °C for 12 h and calcined at 600 and 800 °C for 2 h. The authors synthesized  $\text{CeO}_2$  and concluded that increasing the aging time allowed the formation of smaller particle sizes and less agglomerated powders.

The parameters of synthesis affect directly the obtaining of nanopowders with low agglomeration degree. Therefore, the aim of this research was to evaluate some of the main co-precipitation synthesis conditions to obtain a monophasic  $\text{Al}_2\text{W}_3\text{O}_{12}$  powder with low agglomeration. Three different co-precipitation routes have been compared for the purpose to synthesize  $\text{Al}_2\text{W}_3\text{O}_{12}$  submicronic powders, including i) mixing reactants at room temperature (Method A), ii) mixing reactants at 3.5 °C (Method A35), and iii) mixing reactants with surfactant addition (Method CTAB). The distinct synthesis parameters evaluated regarding the impact on the particle and agglomerate size were: i) molarity of the starting salt solutions (0.1 M and 0.005 M), ii) aging time of the co-precipitated precursor, iii) temperature of co-

precipitation, vi) surfactant addition into the reaction medium, and v) temperature and time of calcination.

## 4.2.

### Materials and methods

#### 4.2.1. Co-precipitation of $\text{Al}_2\text{W}_3\text{O}_{12}$ powders by mixing reactants at room temperature (Method A)

The co-precipitation was conducted by mixing aqueous solutions of  $\text{Al}(\text{NO}_3)_3 \cdot 9\text{H}_2\text{O}$  (Isolar, 99%) and  $\text{Na}_2\text{WO}_4 \cdot 2\text{H}_2\text{O}$  (Sigma Aldrich, 99%), simultaneously, into an empty beaker. Two concentrations of the aqueous solutions were assessed: i) 0.1 M and ii) 0.005 M. The final pH achieved by the resultant dispersion was  $\sim 4.0$ , independently of the molarity of the reactant solutions. The pH was not further adjusted since the precipitation of  $\text{Al}^{3+}$  in the hydroxide-based form is accomplished in the range of  $3.5 \leq \text{pH} < 5$  [94]. Therefore, pH 4 is suitable to promote the co-precipitation of  $\text{Al}_2\text{W}_3\text{O}_{12}$ -based amorphous powder. The co-precipitate was formed immediately after the mixing, recovered by centrifugation and, washed three times with anhydrous ethanol (Vetec, 99.9%). Afterwards, the co-precipitate was dried in a conventional domestic microwave oven for 3 min. Finally, the dried amorphous precursor was calcined in a tubular furnace (model FT-1200/H-1 Z furnace; São Carlos, Brazil) at the desired temperature for 20 min, and then quenched to room temperature in air. The desired calcination temperature was determined based on differential scanning calorimetry (DSC) and thermogravimetric analysis (TGA) data (*vide infra*).

#### 4.2.2. Co-precipitation of $\text{Al}_2\text{W}_3\text{O}_{12}$ powders by mixing reactants at 3.5 °C (Method A35)

The co-precipitation procedure for this method was identical to that described in Section 4.2.1. The only difference lies in the temperature of the aqueous solutions of the reactant salts, controlled at  $\sim 3.5$  °C instead of room temperature. The concentration of the starting solutions was selected based on the optimum molarity defined by Method A. It is important to highlight that in this case, the final pH of the resultant dispersion was  $\sim 5.0$ . Although  $\text{Al}^{3+}$

precipitation in the hydroxide-based form occurs at  $3.5 \leq \text{pH} < 5$  [94], as aforementioned, in order to minimize the synthesis parameters that affect precipitation and allow an equal evaluation with method A only by changing the synthesis temperature, thus, the pH was adjusted to 4 by addition of nitric acid (Isobar, 65%, P.A.) in a molar ratio of 1:3.

#### **4.2.3. Co-precipitation of $\text{Al}_2\text{W}_3\text{O}_{12}$ powders by mixing reactants at 45 °C (Method A45)**

The co-precipitation procedure for this method followed the same methodology applied in Section 4.2.1., although the temperature of the aqueous solutions of the reactant salts has been controlled at  $\sim 45$  °C. The purpose was to study how a variation of  $\pm 20$  °C during the synthesis can or not impact the agglomerates size comparing this method A45 with the method A and A35. As the pH was in the range of  $3.5 \leq \text{pH} < 5$  there was no need of pH adjustment.

#### **4.2.4. Co-precipitation of $\text{Al}_2\text{W}_3\text{O}_{12}$ powders by mixing reactants with CTAB surfactant addition (Method CTAB)**

The co-precipitation was conducted using the same reactant salts previously described in Section 4.2.1, at the optimum molarity defined by Method A. However, instead of the aqueous solutions of reactants being poured into an empty beaker, such solutions were added at the same time into an aqueous solution of a cationic surfactant: the bromide cetyltrimethylammonium, CTAB (Vetec Química Fina Ltda., 99 %). The concentration of the surfactant solution was selected as 0.9 mM. The value of the critical micelle concentration (CMC) of CTAB at room temperature to avoid the formation of micelles in water [33] is  $> 0.9$  mM [95-97]. Note that to assure the nucleation of the amorphous  $\text{Al}_2\text{W}_3\text{O}_{12}$  precursor particles at  $\text{pH} = 4$ , the same pH value employed in the two previous co-precipitation methods, the initial  $\text{pH} = 7.3$  of CTAB solution was adjusted by the addition of nitric acid in a molar ratio of 1:3.

The synthesis was performed under three different temperature conditions: i) reactant and CTAB solutions at room temperature, ii) reactant solutions at 60 °C and CTAB solution at room temperature, and iii) reactant and CTAB solutions at 60 °C. It is important to point out that the CMC of CTAB at 60 °C corresponds to

1.12 mM. Hence, the concentration of 0.9 mM chosen for the preparation of the surfactant solution is also below the CMC at this temperature [96]. After the co-precipitation, the resultant dispersions were allowed to reach room temperature and to follow the steps of recovery, washing, drying, and calcination detailed in Section 4.2.1.

The following nomenclature for identification of the  $\text{Al}_2\text{W}_3\text{O}_{12}$  powders synthesized by the three co-precipitation methods was defined: “Method\_x\_y\_z”, where x is the molarity, y is the calcination temperature, and z is the calcination time. In the case of powders prepared by the third method (Method CTAB), to distinguish among the three temperature conditions, the samples were named as CTAB/a, CTAB/b and CTAB/c for i), ii) and iii) conditions described in Section 2.3, respectively. In the case of amorphous  $\text{Al}_2\text{W}_3\text{O}_{12}$  precursor samples, the prefix “p\_” was added to the previously defined “Method\_x”.

#### **4.2.5. Characterization of amorphous precursor and crystalline $\text{Al}_2\text{W}_3\text{O}_{12}$ powders**

The amorphous precursors were analyzed by DSC/TGA in a PerkinElmer Simultaneous Thermal Analyzer STA-6000 (Seer Green, U.K.), with a heating rate of  $20\text{ }^\circ\text{C min}^{-1}$ , under air flow of  $20\text{ mL min}^{-1}$  in an alumina crucible, for determination of the crystallization temperature and weight losses.

$\text{Al}_2\text{W}_3\text{O}_{12}$  powders were analyzed by X-ray powder diffraction (XRPD) at room temperature, in a D8 Advance X-ray diffractometer (Bruker, Karlsruhe, Germany), using  $\text{CuK}\alpha$  radiation at  $0.02^\circ$  ( $2\theta$ ) step, with an acquisition time of 2 s per step, from  $10^\circ$  to  $80^\circ$  ( $2\theta$ ).

The specific surface area of amorphous precursors and crystallized  $\text{Al}_2\text{W}_3\text{O}_{12}$  powders was determined by the nitrogen adsorption method at  $-196\text{ }^\circ\text{C}$  using a TriStar 3020 V1.03 (Micromeritics, USA), and applying the Brunauer–Emmett–Teller (BET) approach. In addition, the primary particle sizes ( $d_{\text{BET}}$ ) were calculated based on measured specific surface areas, assuming that particles exhibit a spherical shape.

### 4.3.

## Results

### 4.3.1. Amorphous $\text{Al}_2\text{W}_3\text{O}_{12}$ precursor powders

#### 4.3.1.1. Weight losses and crystallization temperature of precursors

Figure 20 shows the TGA/DSC curves of amorphous precursors synthesized by method A, using 0.1 M and 0.005 M reactant aqueous solutions. It is clear that the total weight loss for method A, independently of the used molarity, is very similar (~ 23 wt.% until 600 °C). The weight loss up to 200 °C (17.5 wt.%) can be predominantly ascribed to moisture, while the loss above this temperature can be related to the release of hydroxyl groups since a hydroxide-based precursor is typically obtained from aqueous co-precipitation by mixing reactants. On the other hand, the precursor powder prepared by method A35, using 0.005 M reactant aqueous solutions, presented a weight loss of 50 wt.% until 900 °C (see Figure 21). In this case, the moisture content adsorbed by the precursor was 20 wt.% (weight loss up to 200 °C), whilst the loss at temperatures over 200 °C (30 wt.%) can be attributed in part to OH groups. This second weight loss for pA35\_0.005, much higher than that of precursors synthesized by method A, can be explained considering that nitric acid reacts with water forming nitrate, which can be ascribed to the subtle exothermic peak at 250 - 300 °C [98-100].

Besides that, the precursor prepared by method CTAB, employing 0.005 M reactant aqueous solutions, presented a total weight loss of 27.5 wt. %, in four stages at the following temperature ranges (see Figure 22): i) 25 - 200 °C, ii) 200 - 400 °C, iii) 400 - 625 °C and iv) 625 - 900 °C. The first stage can be related to the loss of the water adsorbed on the precursor surface. Despite hydroxyl groups being released at temperatures in the range of 200 - 900 °C, the mass losses in the second and the last two stages can be also associated with CTAB volatilization [33].

The crystallization temperature of the precursors can be detected from DSC curves (Figure 20, Figure 21, and Figure 22), for all studied methods. Methods A and CTAB show an exothermic peak at 650 °C, while for method A35 it appears at 610 °C. The endothermic peak presented only in Figure 20(a-b) can be attributed to a phase transformation, however, this event is not followed by a significant weight

loss. Thus, as the samples were still amorphous, this phase transformation can be referenced as “*polyamorphism*”, a phenomenon in which amorphous powder exists in different amorphous modifications, analogous to polymorphism in crystallized samples [101-102].

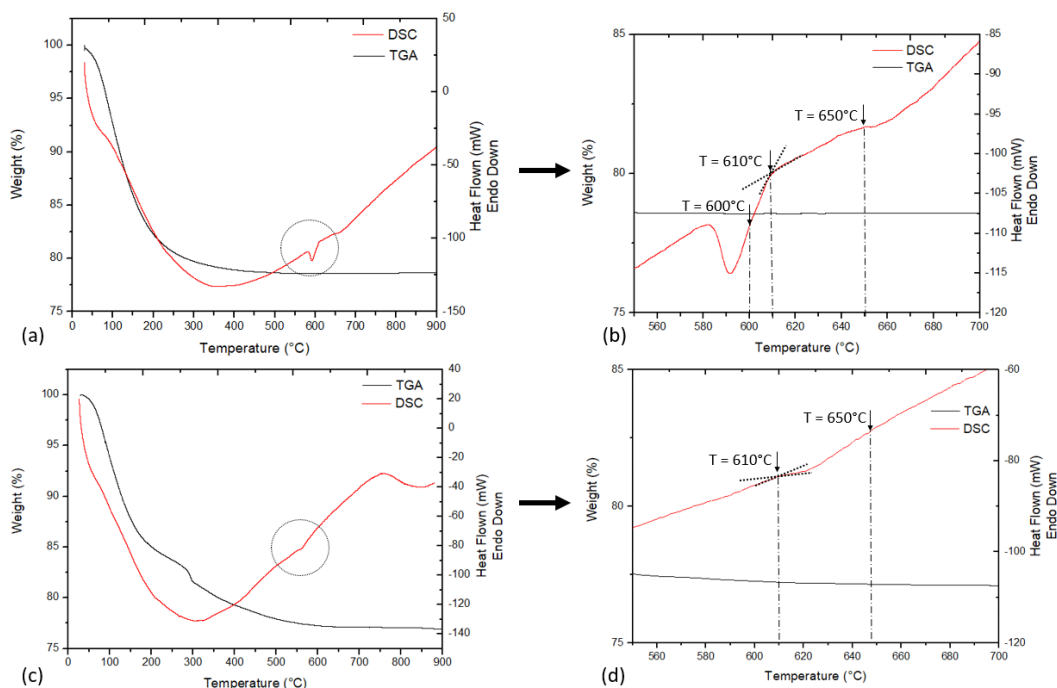


Figure 20: TGA/DSC curves of amorphous precursor synthesized by Method A using (a) 0.1 M and (b) 0.005 M reactant aqueous solutions.

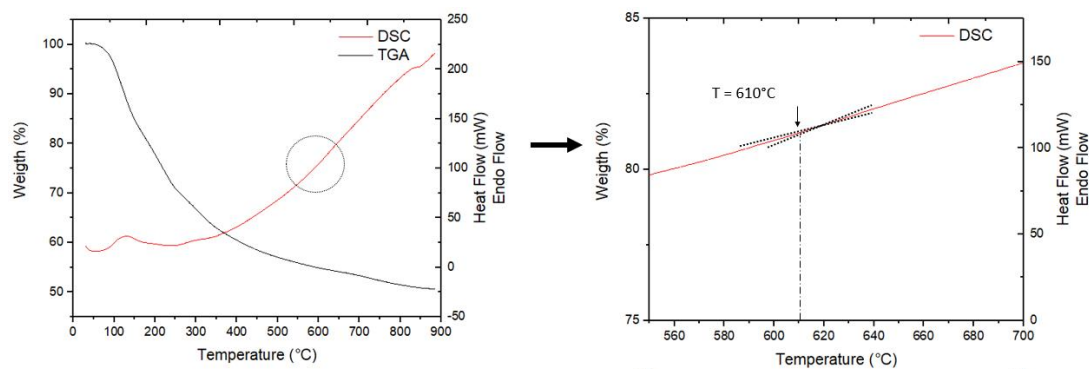


Figure 21: TGA/DSC curves of amorphous precursor synthesized by method A35 using 0.005 M reactant aqueous solutions.

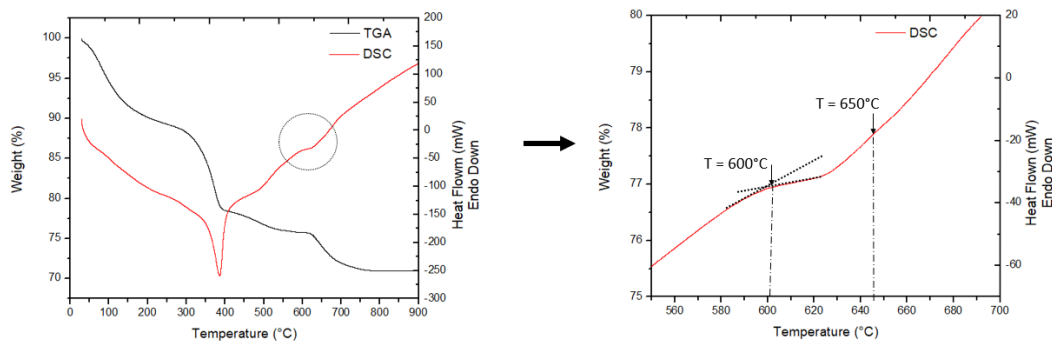


Figure 22: TGA/DSC curves of amorphous precursor synthesized by method CTAB at room temperature and using 0.005 M reactant aqueous solutions.

#### 4.3.1.2. Impact of aging time on crystallization of precursors at room temperature

The impact of aging time was also studied in this work to verify if amorphous precursor samples could become crystallized over time, without the need of calcination step. To evaluate the effect of aging time, the dispersions (co-precipitated amorphous precursor particles and reaction medium), prepared by the methods previously described, were stored at room temperature in the absence of light for a period between 2 and 4 months. No heat treatment has been performed after the aging time was completed.

The equation by Johnson-Mehl-Avrami-Kolmogorov (JMAK, Equation 35), commonly referred to as Avrami equation described the kinetic parameters used to consider the transformation of amorphous solids under isothermal conditions into a crystalline product [103-105].

Equation 35: Johnson-Mehl-Avrami-Kolmogorov

$$\alpha = 1 - \exp(kt^n)$$

where  $\alpha$  is the fraction of crystallized product, while  $k$  and  $n$  are constants and  $t$  is the time.

This equation has been well-established for polymers materials [106]. The volume fraction of crystal content increases with time at a constant temperature [107]. However, some reports applied this equation to ceramics [108-110]. Physical aging occurs on the material (in an aqueous dispersion or dried powder) at a constant temperature with the storage time, without any other external influence

[109,111]. The change of properties of the powder, during aging, is documented for dielectric property [112], isoelectric point [26], and primary particle sizes [31-32].

However, although aging time can promote crystallization of the material, our findings for method A (0.1 M and 0.005 M), A35, and CTAB, revealed no crystallization has been registered through XRPD analysis (amorphous-like XRPD patterns, not shown here).

#### 4.3.2. $\text{Al}_2\text{W}_3\text{O}_{12}$ calcined powder

Table 5 summarizes the synthesis conditions of  $\text{Al}_2\text{W}_3\text{O}_{12}$  nanopowders using the three methods previously described, varying the molarity of reactant aqueous solutions, co-precipitation temperature, and calcination conditions (temperature and time). The specific surface areas achieved for the as-prepared  $\text{Al}_2\text{W}_3\text{O}_{12}$  nanopowders are also presented in Table 5.

Since method A at 0.1 M reactant aqueous solutions was the first method employed, the initial calcination temperature has been based on its TGA/DSC onset temperature at 600 °C for 20 min (see Figure 20a). Nevertheless, after XRPD analysis (not shown), it was concluded that the conditions applied were insufficient to crystallize the amorphous precursor. As such, an increment of temperature to 650 °C was necessary to achieve complete crystallization (Figure 23). Since the crystalline nanoparticles of orthorhombic  $\text{Al}_2\text{W}_3\text{O}_{12}$  were synthesized at 650°C, the calcination temperature was reduced in 5 °C or 10 °C to achieve less agglomerated crystallized nanopowder, in accord with our previous studies [33,34,82].

Method A35 followed the same approach varying the crystallization temperature in small steps, meanwhile method CTAB has been evaluated only for 650 °C. It is worth mentioning that all methods described in Table 5 allowed for the synthesis of monophasic  $\text{Al}_2\text{W}_3\text{O}_{12}$ , as shown in Figure 23, Figure 24, Figure 25, Figure 26 and Figure 27 for method A (0.1 M), method A (0.005 M), method A35 and, method CTAB, respectively, except for sample CTAB/c\_0.005\_650\_20, where traces of monoclinic  $\text{WO}_3$  were identified at  $\sim 33.3^\circ (2\theta)$  [113].

Table 5: Synthesis conditions applied for each method and the specific surface areas and average particle sizes ( $d_{\text{BET}}$ ) of the as-prepared  $\text{Al}_2\text{W}_3\text{O}_{12}$  powders. The density of orthorhombic  $\text{Al}_2\text{W}_3\text{O}_{12}$  phase used for the  $d_{\text{BET}}$  calculation was  $5.12 \text{ g cm}^{-3}$  [114].

Method	Sample nomenclature (Method_x_y_z)	Concentration of reagent solutions (M): x	Calcination temperature ( $^{\circ}\text{C}$ ): y	Calcination time (min): z	BET ( $\text{m}^2\text{g}^{-1}$ )	$d_{\text{BET}}$ (nm)	Comments
A	pA_0.1	0.1	N/A	N/A	10.5	112	Amorphous
	A_0.1_650_20	0.1	650	20	6.3	186	
	A_0.1_640_20	0.1	640	20	6.6	178	
	A_0.1_635_20	0.1	635	20	7.4	158	
	A_0.1_630_20	0.1	630	20	7.3	161	
	A_0.1_625_20	0.1	625	20	7.0	167	
	A_0.1_600_20	0.1	600	20	N/A	N/A	Amorphous
	pA_0.005	0.005	N/A	N/A	34.6	34	Amorphous
	A_0.005_650_20	0.005	650	20	18.0	65	
	A_0.005_640_20	0.005	640	20	18.8	62	
	A_0.005_635_40	0.005	635	40	18.1	65	
	A_0.005_635_30	0.005	635	30	16.6	71	
	A_0.005_635_20	0.005	635	20	29.5	40	
	A_0.005_635_10	0.005	635	10	19.8	59	
	A_0.005_630_20	0.005	630	20	17.9	65	
	A_0.005_625_20	0.005	625	20	N/A	N/A	Amorphous
	A_0.005_625_40	0.005	625	40	11.9	98	
	A_0.005_625_60	0.005	625	60	14.5	81	
A35	pA35_0.005	0.005	N/A	N/A	39.15	30	Amorphous
	A35_0.005_640_20	0.005	640	20	10.3	114	
	A35_0.005_630_20	0.005	630	20	13.4	87	
	A35_0.005_630_10	0.005	630	10	12.5	94	
	A35_0.005_620_20	0.005	620	20	21.8	54	
	A35_0.005_620_15	0.005	620	15	N/A	N/A	Amorphous
	A35_0.005_610_20	0.005	610	20	7.6	154	
A45	A45_0.005_620_20	0.005	620	20	18.0	65	
	A45_0.005_630_20	0.005	630	20	18.5	63	
	A45_0.005_640_20	0.005	640	20	17.3	68	
CTAB	CTAB/a_0.005_650_20	0.005	650	20	3.22	364	
	CTAB/b_0.005_650_20	0.005	650	20	11.9	98	
	CTAB/c_0.005_650_20	0.005	650	20	12.4	95	

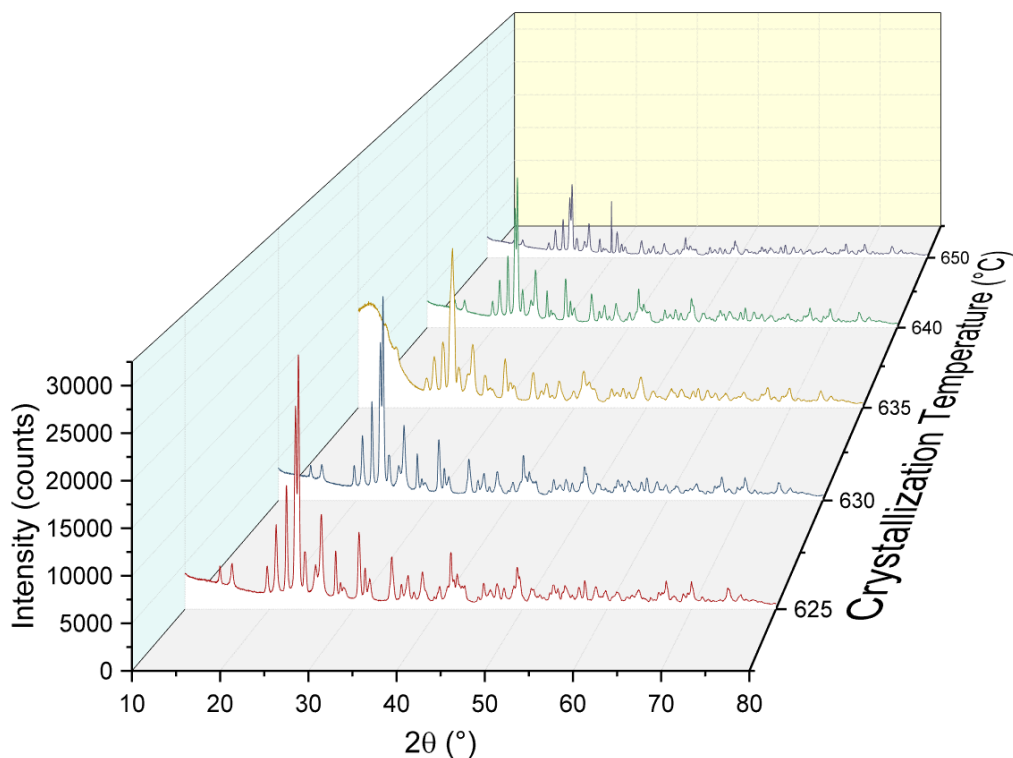


Figure 23: XRPD patterns of monophasic orthorhombic  $\text{Al}_2\text{W}_3\text{O}_{12}$ , obtained by method A (0.1 M reactant aqueous solutions) and calcined at different temperatures for 20 min.

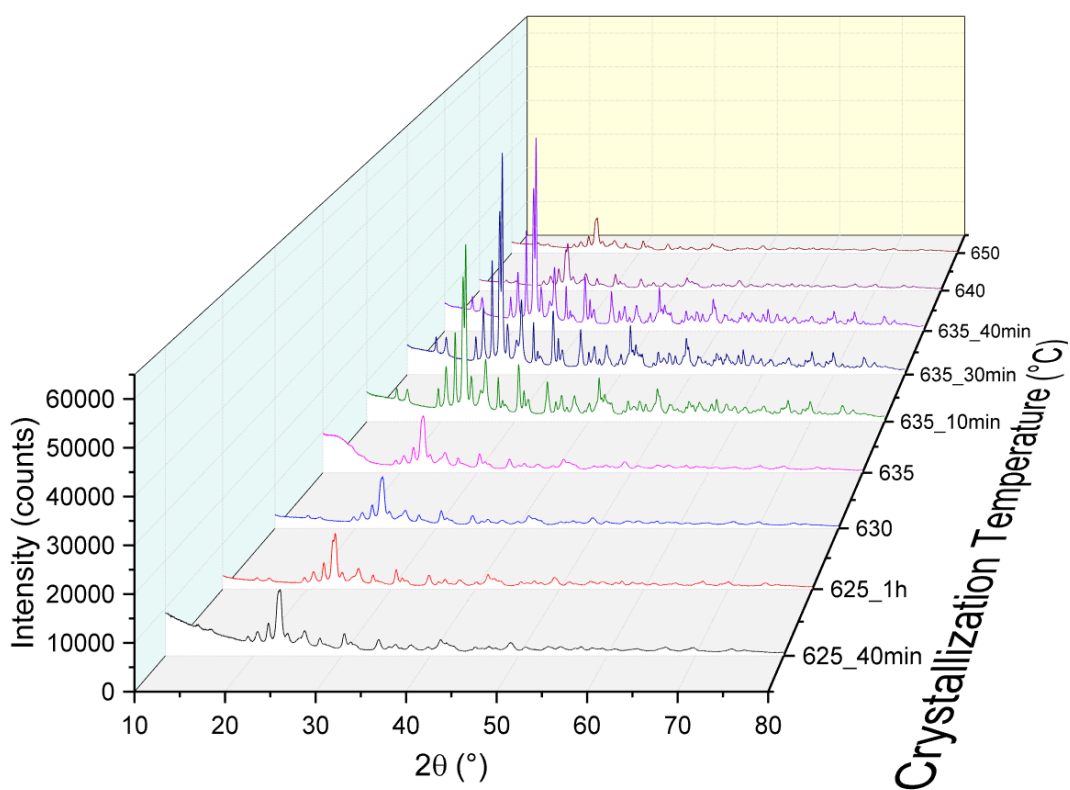


Figure 24: XRPD patterns of monophasic orthorhombic  $\text{Al}_2\text{W}_3\text{O}_{12}$ , obtained by method A (0.005 M reactant aqueous solutions) and calcined at different temperatures for 20 min, if it is not marked different.

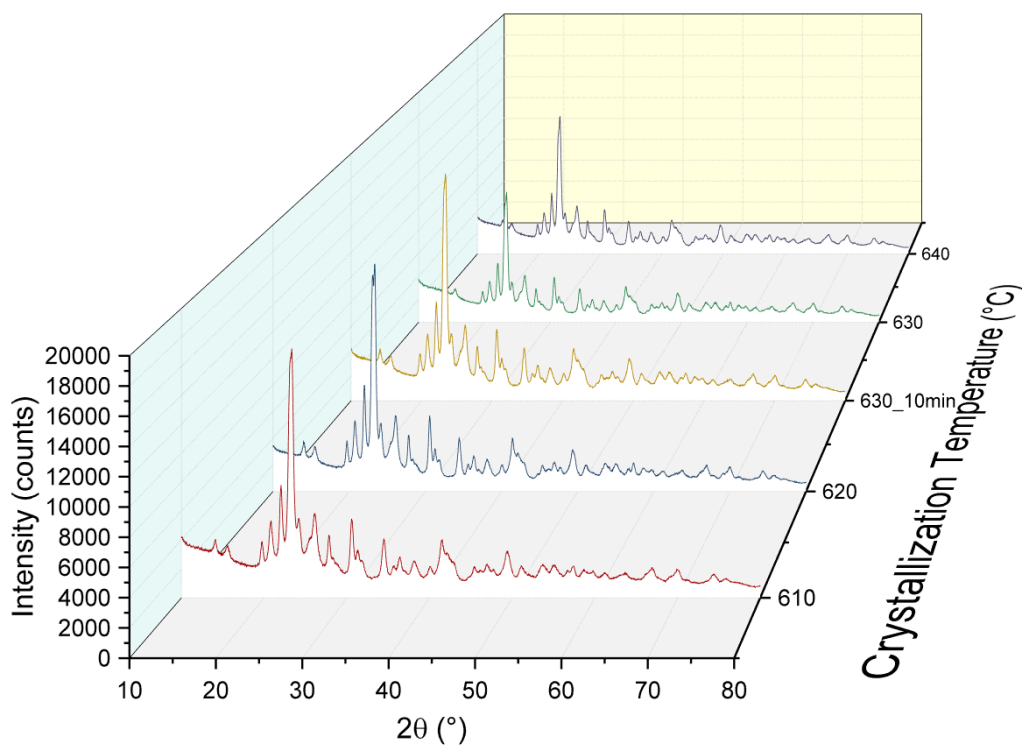


Figure 25: XRPD patterns of monophasic orthorhombic  $\text{Al}_2\text{W}_3\text{O}_{12}$ , obtained by method A35 (0.005 M reactant aqueous solutions) and calcined at different temperatures for 20 min, if it is not marked different.

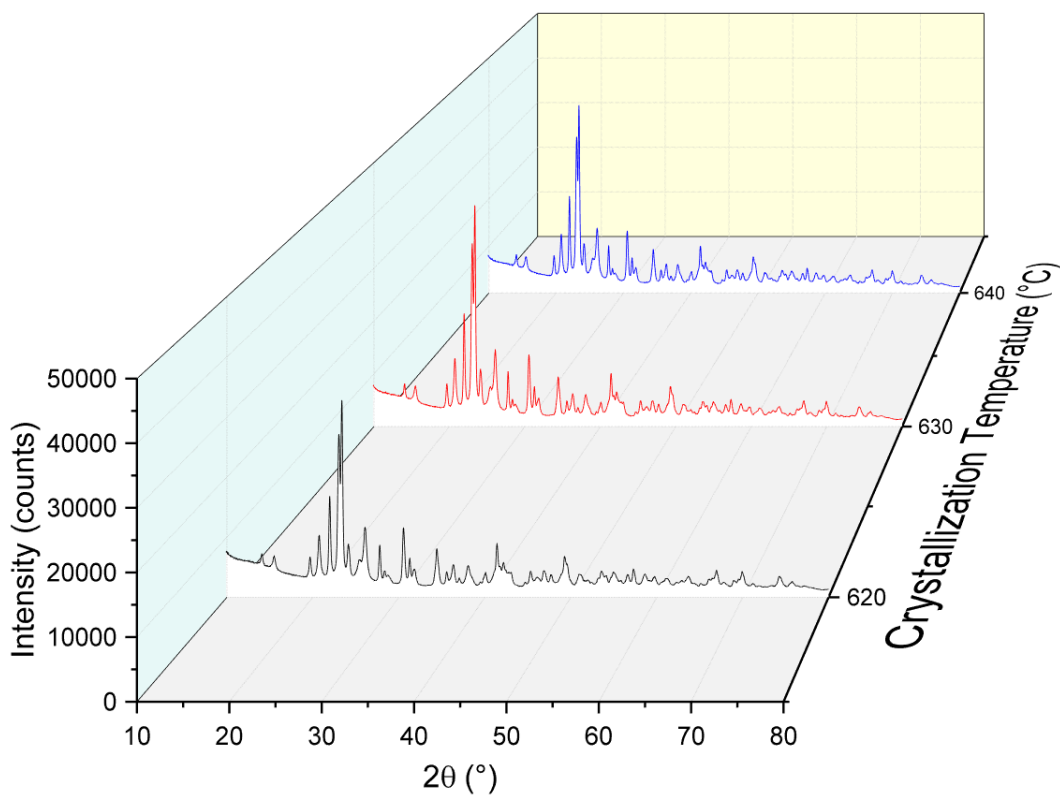


Figure 26: XRPD patterns of monophasic orthorhombic  $\text{Al}_2\text{W}_3\text{O}_{12}$ , obtained by method A45 (0.005 M reactant aqueous solutions) and calcined at different temperatures for 20 min.

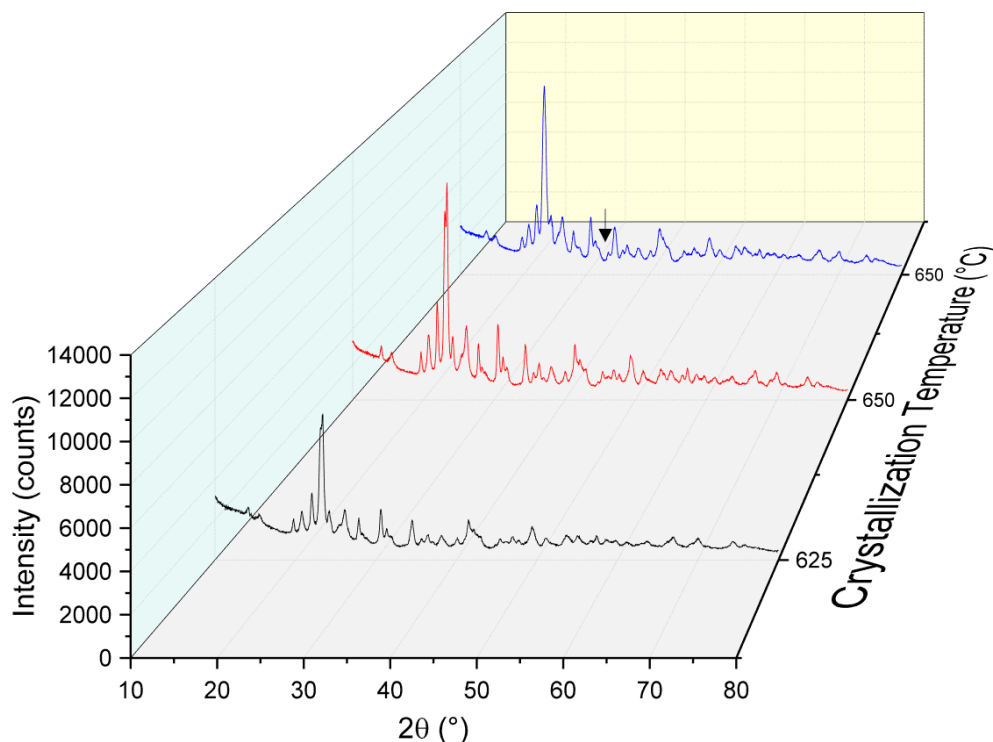


Figure 27: XRPD patterns of orthorhombic  $\text{Al}_2\text{W}_3\text{O}_{12}$  obtained by Method CTAB (0.005 M of reactant aqueous solutions) and calcined at different temperatures. ↓ stands for a diffraction peak of  $\text{WO}_3$ .

#### 4.4. Discussion

##### 4.4.1. Effect of the molarity of the reactant starting solutions

The effect of the molarity of reactant solutions was investigated for two molarities, 0.005 M and 0.1 M. Our data indicated that lower molarity resulted in higher specific surface areas of the amorphous precursor powders (see Table 5). Co-precipitation of precursors involves the stages of nucleation, growth, coarsening, and/or agglomeration processes, as elaborated by LaMer theory [39,115]. Co-precipitation starts when the pH of the solution elevates the supersaturation state to the nucleation threshold according to the LaMer theory and the LeChateleur principle. The supersaturation is the driving force for nucleation and, also, for crystal growth [38]. Therefore, increasing the concentration of solute, increases the nucleation rate (exponentially), in such a manner, that a large number of precipitates with small sizes are formed.

However, a different tendency was found according to Table 5. The most promising specific surface area for amorphous precursors was achieved when the molarity of the reactant aqueous solutions was as low as 0.005 M, through methods A and A35, and corresponding to  $34.6 \text{ m}^2 \text{ g}^{-1}$  and  $39.15 \text{ m}^2 \text{ g}^{-1}$ , respectively. These results can be explained by Equation 36 and Equation 37 which describe the relationship between the rates of nucleation and growth, respectively, regarding the supersaturation (S), growth order (g), a constant of growth ( $k_g$ ), the kinetics parameter ( $K_1$ ), and a parameter that depends on the thermodynamic properties ( $K_2$ ) [48].

Equation 36: Rate of nucleation

$$B = K_1 e^{-\left(\frac{K_2}{\ln^2 S}\right)}$$

Equation 37: Rate of crystal growth

$$G = k_g S^g$$

Thus, the nucleation rate increases exponentially with concentration (supersaturation), while the growth rate is approximately a linear function of supersaturation [41]. In order to guarantee nucleation predominance, the rate of growth must be smaller than nucleation, otherwise, the rate of growth cannot be neglected and will influence the final particle size [116]. Thus, the size of the precursor particles is related to the competition between nucleation and growth kinetics [117].

Supersaturation is of paramount importance since it is the driving force for nucleation and growth of particles during co-precipitation. When the supersaturation is low, precursor particles can grow quicker than they nucleate, which gives rise to a larger particle size distribution. On the other hand, at higher supersaturations, the nucleation surpasses the crystal growth rate, which leads to smaller precursor particles. Thus, there is a supersaturation threshold which defines the dominance of growth rate (low supersaturation), or nucleation (high supersaturation), as can be seen in the following Figure 28 [38,118]:

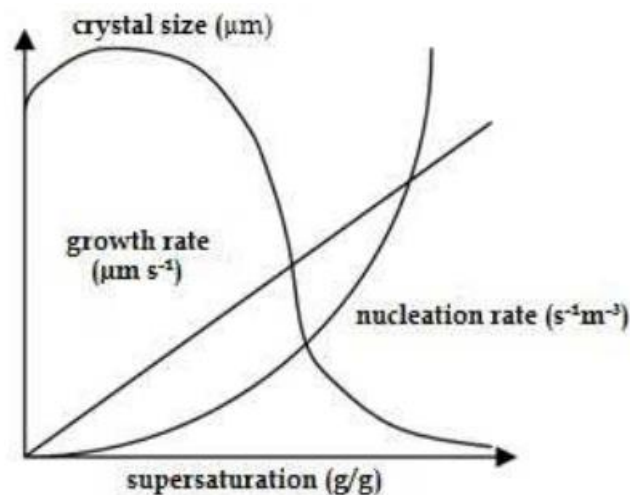


Figure 28: Relationship between supersaturation, nucleation, and growth [38].

In the present work, we have not defined the supersaturation threshold for the formation of precursor particles of  $\text{Al}_2\text{W}_3\text{O}_{12}$ . However, it would be expected that precursor pA\_0.1, prepared in a condition of high supersaturation compared to precursor pA35\_0.005, presents a high specific surface area and, consequently, a lower particle size. However, the opposite trend was observed. This could be explained because, at high supersaturation values (expected for 0.1 M reactant aqueous solutions), smaller precursor nanoparticles would be formed, however, these could easily agglomerate to reduce their high surface energy, resulting in specific surface area of  $10.5 \text{ m}^2 \text{ g}^{-1}$  for pA\_0.1 compared to  $39.15 \text{ m}^2 \text{ g}^{-1}$  for pA\_0.005 (see Table 5). In the case of precursor pA\_0.005, possibly, precursor particles grew more (forming larger nanoparticles) but are fewer and agglomerated less. Therefore, their specific surface areas were higher (Table 5).

#### 4.4.2. Effect of the synthesis temperature during co-precipitation on the particle size of $\text{Al}_2\text{W}_3\text{O}_{12}$ powders

The synthesis temperature strongly influences the nucleation and growth rate during co-precipitation. As a matter of fact, a low temperature increases the supersaturation due to a decrease in the solubility of the reactants, promoting both the nucleation and crystal growth to a greater extent than at a high temperature. Therefore, larger particle sizes would be obtained at low temperatures [120]. Thus, it would be expected that the precursor prepared at  $3.5 \text{ }^\circ\text{C}$  exhibits a lower specific

surface area, and larger particle size, compared to the precursor prepared at room temperature. However, the assessed synthesis temperatures, for molarity of reactant solutions of 0.005 M, did not significantly impact the BET values of precursors pA\_0.005 ( $39.15 \text{ m}^2 \text{ g}^{-1}$ ) and pA35\_0.005 ( $34.6 \text{ m}^2 \text{ g}^{-1}$ ), as can be seen in Table 5. This outcome demonstrates that for the synthesis of  $\text{Al}_2\text{W}_3\text{O}_{12}$  precursors, a variation of about  $20 \text{ }^\circ\text{C}$  did not cause important changes in the amorphous particle size.

Although the result for the amorphous sample by method A45 was not possible to achieve, comparing the results of calcined samples under the same conditions of temperature and time for methods A, A35 and A45, it is well noted that there is a strong reduction impact on the agglomerates size regarding the agglomerates size for the temperatures of  $630$  and  $640 \text{ }^\circ\text{C}$  (method A and A45). As previously stated, the dependence of nucleation rate and temperature is exponential, therefore, high temperature increases the nucleation rate, and then, small particle sizes would be obtained at high temperatures.

On the other hand, the sample of method A45 calcined at  $620 \text{ }^\circ\text{C}$  presented a small increment (practically derisory) in  $d_{\text{BET}}$  results compared with the sample of method A35. Likely, the phenomenon of nanoparticle agglomeration overrides the effect of temperature on nucleation and growth processes.

#### **4.4.3. Effect of the crystallization temperature and calcination time on the particle size of $\text{Al}_2\text{W}_3\text{O}_{12}$ powders**

Several studies relate the increment of the crystallization temperature with the increase in mean particle size [33-34, 121-123]. However, most of these reports studied the increments of  $100 \text{ }^\circ\text{C}$  in the crystallization temperature which favors a significant increase of particle sizes.

The crystallization and crystal growth is a thermally activated process. The Arrhenius equation describes the relationship between the rate of reaction ( $k$ ) and temperature (see Equation 38) [124].

Equation 38: Arrhenius equation

$$k = A e^{-\frac{E_a}{k_B T}}$$

where  $k_B$  is the rate constant,  $T$  is the absolute temperature,  $A$  is a temperature-independent constant for each chemical reaction,  $E_a$  is the activation energy for the reaction and  $k_B$  is the Boltzmann constant.

Borgwardt [125], developed a calcination model for small particles that relates the calcination as a function of time (Equation 39).

Equation 39: Borgwardt equation

$$\ln(1 - x) = -K_c s_g t$$

where  $x$  is fractional conversion from amorphous to crystalline phase during the calcination,  $K_c$  is the rate constant of the calcination reaction,  $s_g$  is the initial specific surface area and  $t$  is the time. Thus, the calcination rate at time  $t$  is proportional to the specific surface area. As can be seen from the above Equations, the influence of the temperature is exponential, while the influence of time is linear. Hence, small increments in the calcination temperature have a greater impact than the calcination time on particle size.

Figure 29 shows the relationship between the calcination temperature and particle size. The methods (A, A35 and A45) presented an optimal temperature of crystallization with the highest specific surface area, except for method A (0.1 M), which presented almost no variation in specific surface area with the calcination temperature. However, as explained in sec. 4.4.1 the molarity 0.1 M of the starting salt reactants solutions favored the agglomeration.

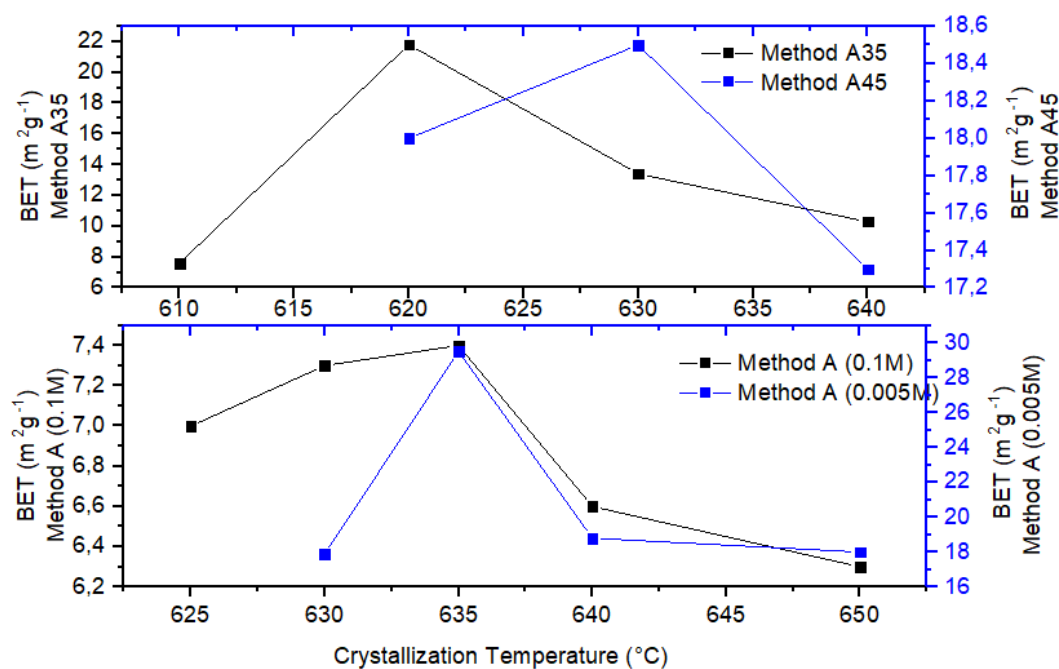


Figure 29: Relationship between specific surface areas ( $\text{m}^2\text{g}^{-1}$ ) and calcination temperatures (samples calcined during 20 min).

The best result related to the specific surface area compared with the amorphous precursor ( $34.6 \text{ m}^2 \text{ g}^{-1}$ ) was presented by the sample from method A (0.005 M) which was calcined at  $635 \text{ }^\circ\text{C}$  during 20 min ( $29.5 \text{ m}^2 \text{ g}^{-1}$ ) presenting a small reduction of 14.6% of specific surface area after calcination. An attempt to crystallize this sample at  $625 \text{ }^\circ\text{C}$  for 20 min was performed twice but the sample kept amorphous.

It is expected that the calcination time variation has less impact than the calcination temperature once the influence of the temperature is exponential, while the influence of time is linear. Table 6 presents the average of specific surface area and their standard deviation for each method evaluating the effect of the crystallization temperature and calcination time, while Figure 30 shows the relationship between the calcination time and particle size in respect of calcination temperatures  $625$  and  $635^\circ\text{C}$ .

Table 6: Comparison between different methods evaluating the effect of the crystallization temperature and calcination time on the particle size for orthorhombic  $\text{Al}_2\text{W}_3\text{O}_{12}$  phase.

Method	Temperature variation and constant time (20 min)		Time variation (constant temperature)	
	Average BET ( $\text{m}^2\text{g}^{-1}$ )	Standard deviation	Average BET ( $\text{m}^2\text{g}^{-1}$ )	Standard deviation
A (0.1M)	7	0,5	-	-
A (0.005M)	18,4	5,6	19,0 <sup>(1)</sup>	5,8 <sup>(1)</sup>
			13,2 <sup>(2)</sup>	1,8 <sup>(2)</sup>
A35	11,85	6,2	12,95 <sup>(3)</sup>	0,6 <sup>(3)</sup>
A45	18	0,6	-	-

<sup>(1)</sup> Calcination at 635 °C

<sup>(2)</sup> Calcination at 625 °C

<sup>(3)</sup> Calcination at 630 °C

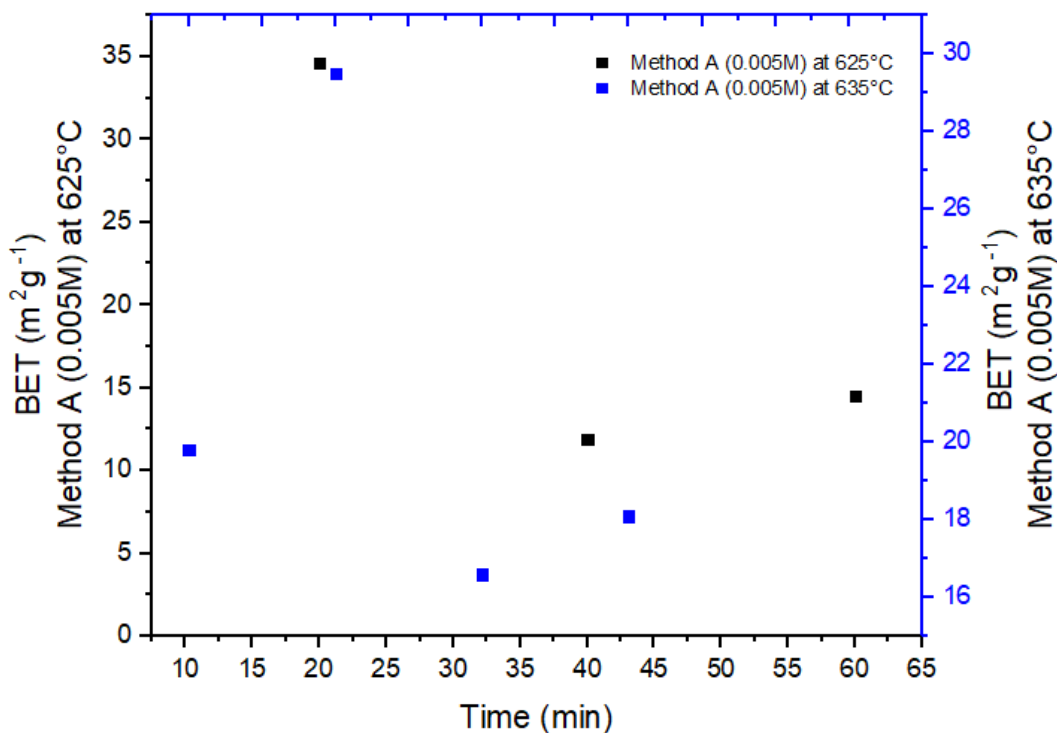


Figure 30: Relationship between specific surface areas ( $\text{m}^2\text{g}^{-1}$ ) and calcination time for samples of method A calcined at 625 and 635°C.

## 4.5. Conclusions

$\text{Al}_2\text{W}_3\text{O}_{12}$  powders were synthesized by different methods based on co-precipitation method. A detailed analysis of molarity, aging time, synthesis temperature as well as crystallization temperature has been performed. The molarity of 0.005 M (method A) showed to be very promising regarding the high surface area found for amorphous ( $34.6 \text{ m}^2 \text{ g}^{-1}$ ) and crystalline ( $29.5 \text{ m}^2 \text{ g}^{-1}$ ) samples. The decrease in the synthesis temperature (method A35) induced a supersaturation stage which stabilize the precipitate and controlled the growth, although the specific surface area of the crystalline sample was below that of the sample synthesized at room temperature.

Nonetheless, the results with CTAB addition (method CTAB), due to the increment in the temperature, avoided the formation of micelles due to the high concentration of surfactant used (0.9 mM). The results of this method using temperature above the room temperature showed BET results nearby to method A35 and higher than method A (0.1 M).

Method CTAB could be further explored to define a better relationship between the synthesis temperature and the critical micelle concentration, or even to replace the type of cationic surfactant. Steric stabilization, indeed, favors the particles to be repelled during the calcination step, thus, another variation of the method could be implemented, performing the full synthesis of method A and adding the surfactant on the final suspension with the aim to minimize the agglomeration of the powder during calcination.

## 5.

### Non-Hydrolytic Sol-Gel synthesis of $\text{Al}_2\text{W}_3\text{O}_{12}$ nanopowders

#### 5.1

#### Background

In recent years, there has been renewed interest in improving the synthesis routes of advanced ceramics for obtaining thermodynamically stable and/or metastable phases at low or moderate temperatures, through several soft-chemistry approaches. Among them, the non-hydrolytic sol-gel (NHSG) method has been intensively studied during the last three decades, due to its versatility in the preparation of mixed metal oxides, since it involves reactions between metal halides and an oxygen donor different from water, such as, alkoxide, alcohol or ether and the synthesis occurs in the absence of water/moisture [64,70, 126-127]. In the conventional sol-gel route for the synthesis of mixed metal oxides within an aqueous medium, the hydrolysis and condensation reactions may proceed at different rates depending on the alkoxide, resulting, occasionally, in inhomogeneous oxide ceramic powders [128]. However, the NHSG provides very homogeneous atomic mixtures offering the possibility to synthesize monophasic mixed metal oxides. Besides, volatile organic solvents used in NHSG, characterized by a surface tension lower than presented by water, simplify the drying step and allow the formation of highly porous ceramics with high specific surface areas [65].

Amongst the variety of metal mixed oxides cataloged as advanced ceramics, the ceramics with negative, zero, or low-positive thermal expansion, the so-called thermomiotics, have been the subject of growing studies due to their potential engineering applications as thermal shock resistance ceramics or as fillers to control the undesired high positive thermal expansion of a vast variety of composite matrices [1,5,93,129-130].  $A_2M_3O_{12}$  family of thermomiotics and low-positive thermal expansion phases comprises the  $\text{Al}_2\text{W}_3\text{O}_{12}$  phase, which has been explored in recent years as the exemplar phase, due to its relatively low cost in comparison to other members of this ceramic family.  $\text{Al}_2\text{W}_3\text{O}_{12}$  exhibits low positive thermal expansion ( $\sim 1.50 \times 10^{-6} \text{ }^\circ\text{C}^{-1}$ ), in the temperature range between 25 and 800  $^\circ\text{C}$  [79-

81], and its sintering and mechanical properties have been reported in a few recent studies [10,79,85].

Prisco et al., [10], reported the synthesis of  $\text{Al}_2\text{W}_3\text{O}_{12}$  by co-precipitation method, starting from  $\text{Al}(\text{NO}_3)_3 \cdot x\text{H}_2\text{O}$  and  $(\text{NH}_4)_6\text{W}_{12}\text{O}_{39} \cdot x\text{H}_2\text{O}$ . The crystalline state was reached by calcination at 650 °C for 30 min. In addition, these authors compared two sintering approaches focusing on the mechanical properties for applications that required a high thermal shock resistance. The specific surface area of the  $\text{Al}_2\text{W}_3\text{O}_{12}$  co-precipitated powder was, however, as low as  $2.1 \text{ m}^2 \text{ g}^{-1}$ .

In another study, Prisco et al., [79] prepared  $\text{Al}_2\text{W}_3\text{O}_{12}$  through a total evaporation route using the same starting reagents as in [10], however, increasing calcination temperature to 750°C, for 30 min. The as-obtained powder showed a specific surface area of  $9.6 \text{ m}^2 \text{ g}^{-1}$ . Pontón et al., [82], synthesized  $\text{Al}_2\text{W}_3\text{O}_{12}$  powder by the normal strike co-precipitation method using the same starting reagents, as in the two previous studies [10,79], and the calcination at 750 °C for 30 min. The specific surface area of the as-synthesized powder was  $7.7 \text{ m}^2 \text{ g}^{-1}$ .

On the other hand, Jardim et al., [85], synthesized  $\text{Al}_2\text{W}_3\text{O}_{12}$  by co-precipitation method, starting from  $\text{Al}(\text{NO}_3)_3$  and  $\text{Na}_2\text{WO}_4$  and calcined the amorphous powder at 800 °C, for 30 min. The as-obtained powder presented a low specific surface area of  $1.2 \text{ m}^2 \text{ g}^{-1}$ .

Therefore, the synthesis routes described in the literature imply the formation of agglomerated  $\text{Al}_2\text{W}_3\text{O}_{12}$  powders, resulting in low specific surface areas and large agglomerates. These features of the previously prepared powders can be ascribed, partially, to the calcination step, mandatory to crystallize the amorphous co-precipitated precursors into the desired phase, and which gives rise to the necking among adjacent particles. As a consequence, strongly agglomerated  $\text{Al}_2\text{W}_3\text{O}_{12}$  powders are produced [33-34]. This powder feature prevents achieving i) highly dense  $\text{Al}_2\text{W}_3\text{O}_{12}$  bulk ceramics with improved thermal shock resistance (free of microcracks) [10] and ii) nanofillers with low agglomeration degree, which can be easily and homogeneously dispersed into metal, ceramic, or polymer matrices [129].

Encouraged by the advantages of the NHSG method, Gates et al. [77], synthesized  $\text{Ga}_2\text{Mo}_3\text{O}_{12}$ , a member of the  $A_2M_3O_{12}$  family, for the first time. The authors mixed stoichiometric quantities of  $\text{GaCl}_3$  and  $\text{MoCl}_5$  and used distilled acetonitrile as a solvent under an argon atmosphere. Isopropyl ether was added as

the oxygen source. The as-prepared mixture was cooled in liquid nitrogen and sealed under a vacuum. Afterwards, the ampoule was heated at 130 °C for one week, and subsequently, was opened in the air. After a few heat treatment steps (first calcination at 300 °C, for 3 h and the second one at 600 °C, for 3 h), a metastable monoclinic  $\text{Ga}_2\text{Mo}_3\text{O}_{12}$  was crystallized.

Gates and Lind [76] prepared  $\text{Y}_2\text{Mo}_3\text{O}_{12}$  by NHSG. The authors used the same approach detailed previously [77]. The sample was calcined at 300 °C for 4 h, however, it was still amorphous. The  $\text{Y}_2\text{Mo}_3\text{O}_{12}$  crystallized in the orthorhombic phase at a temperature higher than 550 °C.

Truitt et al. [75], synthesized  $\text{AlScMo}_3\text{O}_{12}$  using NHSG. The reactions were carried out using a glovebox and standard Schlenk procedure. The reactant solution was kept under stirring during the addition of solvent (acetonitrile) and diisopropyl ether. The ampoule was cooled in liquid nitrogen, evacuated and flame sealed. Then, the ampoule was heated at 150 °C for 7 days and afterwards was opened in the air. The as-obtained powder was calcined at 700 °C for 3 h to crystallize the  $\text{AlScMo}_3\text{O}_{12}$  phase.

Baiz et al. [131], synthesized  $\text{HfMgW}_3\text{O}_{12}$  and  $\text{ZrMgW}_3\text{O}_{12}$  using also Schlenk and glovebox procedures. The mixture was stirred at room temperature for 30 min, then cooled in liquid  $\text{N}_2$ , sealed under vacuum and heated at 130 °C for 3 to 5 days. Then, the powder was washed with  $\text{CHCl}_3$ . The as-prepared powders received heat treatment between 500 °C and 1050 °C. The secondary phases started to disappear at the temperatures  $> 540^\circ\text{C}$ . The samples were heat treated, at least, for 2h. The scanning electron microscopy (SEM) images confirmed formation of spherical particles, organized into micron-sized agglomerates, between 1 and 6  $\mu\text{m}$ .

In many cases, the amorphous precursor powders are recovered, dried and then, crystallized at temperatures higher than 500 °C, as discussed previously. However, Young et al. [74], reported the NHSG synthesis of the  $A_2M_3O_{12}$  family, in which  $A = \text{Fe, In or Sc}$  and  $M = \text{Mo}$ , using a similar synthesis approach as in [131], with the difference that the first heating of the solution was carried out between 80 and 170 °C, for periods from 1 to 28 days. As the ampoule was previously sealed, after the heating described above, the ampoule was cooled and opened and the content placed over an evaporation dish. A second heating, between 230 and 300 °C for, at least, 3 h, was performed to complete the drying process.

Interestingly, it was observed that these samples crystallized at these low temperatures.

Even though the calcination temperatures for the amorphous powders prepared by NHSG and co-precipitation are similar in many cases, the formation of a more homogenous precursor in the former approach could have an impact during calcination since it has been suggested that volatilization of organic fragments additionally contribute to the preparation of deagglomerated powders [33].

Despite some advantages of the NHSG method over other synthesis methods, the drawbacks are complex and laborious, time-consuming, steps. In this context, the aim of the present research was to synthesize  $\text{Al}_2\text{W}_3\text{O}_{12}$  nanopowders with high specific surface area *via* NHSG through a simpler and more rapid route than the generally reported in the literature, consisting of two steps: i) amorphous  $\text{Al}_2\text{W}_3\text{O}_{12}$ -based powder synthesis through total evaporation under inert atmosphere and ii) crystallization by rapid heat treatment. To assess the impact of these steps on the specific surface area of the as-prepared  $\text{Al}_2\text{W}_3\text{O}_{12}$  powders, two molarities of the reagent solutions were selected, as well as different calcination temperatures. In addition, there are no reports exploring the synthesis of  $\text{Al}_2\text{W}_3\text{O}_{12}$  by NHSG routes, as the authors are aware.

## 5.2. Materials and methods

### 5.2.1. Synthesis of $\text{Al}_2\text{W}_3\text{O}_{12}$ powders by NHSG

The NHSG synthesis was conducted by spilling 0.1 M or 0.005 M solutions of  $\text{AlCl}_3$  (anhydrous, Sigma Aldrich, 99.99%) into  $\text{WCl}_6$  (Sigma Aldrich, 99.99%), both dissolved, separately, in acetonitrile (Sigma Aldrich, anhydrous, 99.8%).  $\text{AlCl}_3$  was easily dissolved, however, to increase the dissolution of  $\text{WCl}_6$  it was necessary to keep the solution under magnetic stirring (150 rpm for 0.1M and 300 rpm for 0.005M) at 50 °C for 20 min before the  $\text{AlCl}_3$  addition. All previous procedures were carried out under severely controlled conditions of humidity (significantly lower than 50 ppm) and in a nitrogen atmosphere in dried glassware using a glovebox (MB-ProVap-3, MBRAUN) at room temperature. After the reactants were mixed, a dark orange solution was formed, and diisopropyl ether (Sigma Aldrich,  $\geq 98.5\%$ ) was added as an oxygen donor, changing the color of the

solution to yellow. The synthesis continued by stirring, at room temperature, for 30 min, and the color of the mixture changed to dark brown. The 0.1 M solution was further kept under stirring at 130 °C until total evaporation in a nitrogen atmosphere after 2 days. For the 0.005 M solution, despite being kept under continuous stirring, the temperature for evaporation was intermittent, *i.e.*, the mixture was heated for 8 h at 130 °C and cooled at room temperature for a period of 16 h in a nitrogen atmosphere. This heating cycle was maintained until complete evaporation (4 days). The amorphous precursor powders were labeled  $\text{pAl}_2\text{W}_3\text{O}_{12}\text{-NHSG-0.1M}$  or  $\text{pAl}_2\text{W}_3\text{O}_{12}\text{-NHSG-0.005M}$ , for the molarities of 0.1 M and 0.005 M, respectively. The dried amorphous precursors, after total evaporation inside the glovebox, were recovered with a stainless steel spatula and the powder stored in a plastic snap cap vial. Then, the powder was transferred to an alumina crucible and calcined for 20 min, in a tubular furnace (model FT-1200/H-1 Z furnace; São Carlos, Brazil) after achieving the desired temperature, based on thermogravimetric analysis (TGA) and differential scanning calorimetry (DSC) data. Then, the as-synthesized light grey color  $\text{Al}_2\text{W}_3\text{O}_{12}$  powders were removed from the furnace and cooled in ambient atmosphere to room temperature.

The yield of crystalline, orthorhombic,  $\text{Al}_2\text{W}_3\text{O}_{12}$  phase, calculated by comparing the theoretical mass and the mass after calcination, varied between 73% and 80% for the majority of calcination temperatures, while it was as high as 88% for the powders calcined at 645 °C and 660 °C, using 0.005 M solutions.

### 5.2.2. Characterization of amorphous and crystalline $\text{Al}_2\text{W}_3\text{O}_{12}$ powders

The amorphous  $\text{Al}_2\text{W}_3\text{O}_{12}$  precursors were analyzed by TGA/DSC in a PerkinElmer Simultaneous Thermal Analyzer STA-6000 (Seer Green, U.K.) with a heating rate of 20 °C  $\text{min}^{-1}$ , under air flow of 20  $\text{mL min}^{-1}$  in an alumina crucible, for determination of the crystallization temperature and weight losses.

$\text{Al}_2\text{W}_3\text{O}_{12}$  powders were analyzed by X-ray powder diffraction (XRPD) at room temperature, on a D8 Advance X-ray diffractometer (Bruker, Karlsruhe, Germany), using  $\text{CuK}_\alpha$  radiation at 0.02° (2 $\theta$ ) step, with an acquisition time of 2 s per step, from 10° to 80° (2 $\theta$ ).

The specific surface area (BET) was determined by the nitrogen adsorption method at  $-196\text{ }^\circ\text{C}$  in a TriStar 3020 V1.03 (Micromeritics, USA) and applying the Brunauer–Emmett–Teller (BET) approach. In addition, the average particle sizes ( $d_{\text{BET}}$ ) were calculated based on measured specific surface areas, assuming spherical shapes for the particles.

Scanning Electron Microscopy (SEM) has been performed on a JEOL – JSM-6701F equipment operating at 2 kV, using secondary electrons, to reveal the morphology and size of the  $\text{Al}_2\text{W}_3\text{O}_{12}$  particles.

Transmission Electron Microscopy (TEM) has been performed on a JEM-2100F operating at 200 kV. For this experiment, a small amount of powder ( $\text{Al}_2\text{W}_3\text{O}_{12}$  0.005 M, calcined at  $660\text{ }^\circ\text{C}$ ) is ultrasonically dispersed in isopropyl alcohol and then dropped onto a holey carbon film supported by a copper grid.

### 5.3

#### Results and discussions

It is worth mentioning that the NHSG reaction used in our synthesis, between metal chlorides and diisopropyl ether is a rigorously non-hydrolytic aprotic condensation reaction which does not form water in-situ, as established previously by Vioux [67] and Vioux and Mutin [132]. In addition, Wang et al.[66], recently measured, by Karl Fischer titration, in-situ water formation during the reaction between  $\text{ZrCl}_4$  and diisopropyl ether and confirmed that this kind of reaction is a strictly non-hydrolytic reaction which does not result in in-situ water formation.

The exothermic peaks on the DSC curves related to the crystallization process of amorphous  $\text{Al}_2\text{W}_3\text{O}_{12}$ -based powders, obtained by different molarities of the starting reagents (Figure 31a and b), were very weak and not well resolved, appearing as a slight change of the slope at around  $600\text{ }^\circ\text{C}$ , for  $\text{pAl}_2\text{W}_3\text{O}_{12}\text{-NHSG-0.1M}$  and  $\text{pAl}_2\text{W}_3\text{O}_{12}\text{-NHSG-0.005M}$ . To guarantee the crystallization of the as-synthesized  $\text{Al}_2\text{W}_3\text{O}_{12}$  precursors and to confirm the viability of the as-performed NHSG approach, it was firstly chosen to tentatively crystallize the  $\text{Al}_2\text{W}_3\text{O}_{12}$  precursor, prepared from 0.1 M solution, at  $950\text{ }^\circ\text{C}$ , during 5 h. This sample was denoted  $\text{Al}_2\text{W}_3\text{O}_{12}\text{-950}^\circ\text{C-5h}$ . In addition, despite the difference in the used molarities (0.1 M and 0.005 M), the weight losses were very similar for both precursors and close to 50 % until the end of the TGA (Figure 31a

and Figure 31b). These weight losses are in the range reported by Truitt et al. [75], from 20 to 50 wt. %, for  $\text{AlScMo}_3\text{O}_{12}$  samples synthesized at the same temperature of the present work (130 °C) and by the same rigorously non-hydrolytic route as in our synthesis. The weight loss of the precursors up to 200 °C corresponded to ~ 20 -22.5 %, which can be ascribed to moisture [126], due to the fast absorption of water from the atmosphere on the precursor surface, when the powder was removed from the glovebox. Similar weight losses have been reported in the literature in the case of  $\text{V}_2\text{O}_5$  [126] and  $\text{Fe}_2\text{Mo}_3\text{O}_{12}$  [74] precursors prepared by rigorously non-hydrolytic reactions. The weight loss above 200 °C (~27.5 - 30 %) can be attributed to the release of residual organics since the NHSG method produces amorphous oxide precursors with a high organic content [74,126]. This was consistent with the fact that the precursors exhibited a black color, suggesting a high amount of organics.

Figure 32 and Figure 33 show XRPD patterns of  $\text{Al}_2\text{W}_3\text{O}_{12}$  for 0.1 M and 0.005 M calcined in the temperature range between from 600 to 950 °C. Both series of calcined samples, matched well with the orthorhombic crystal structure (*Pbcn* space group) previously reported by Woodcock et al. [80]. The majority of the powders presented a weak diffraction peak at ~ 33.3° (2 $\theta$ ) due to monoclinic  $\text{WO}_3$  [113], while the powders  $\text{pAl}_2\text{W}_3\text{O}_{12}\text{-NHSG-0.005M}$  calcined at 650 °C and 660 °C, as well as the sample  $\text{Al}_2\text{W}_3\text{O}_{12}\text{-950}^\circ\text{C-5h}$ , were completely monophasic. In addition, broad diffraction lines observed for the diffraction patterns acquired on the powders treated at the calcination temperatures  $\leq 660$  °C, suggested the nanocrystalline state of these powders [126].

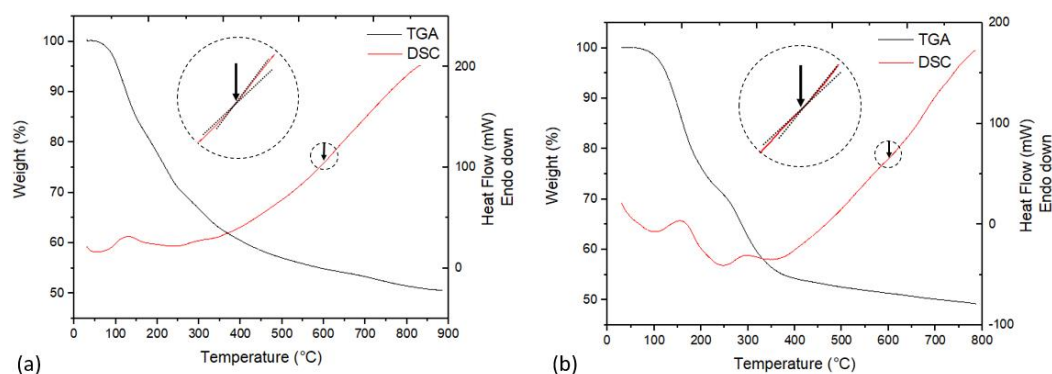


Figure 31: TGA/DSC curves of amorphous  $\text{Al}_2\text{W}_3\text{O}_{12}$ -based precursors synthesized by NHSG (a)  $\text{pAl}_2\text{W}_3\text{O}_{12}\text{-NHSG-0.1M}$  (b)  $\text{pAl}_2\text{W}_3\text{O}_{12}\text{-NHSG-0.005M}$ .

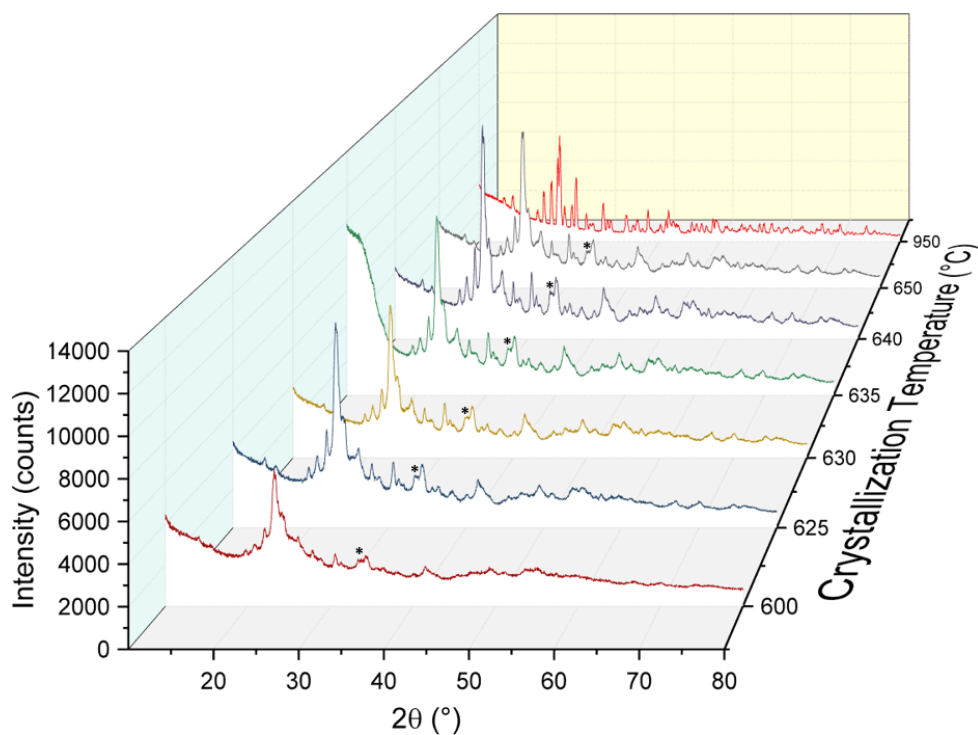


Figure 32: XRPD patterns of orthorhombic  $\text{Al}_2\text{W}_3\text{O}_{12}$  (0.1 M) obtained by NHSG route; \* stands for a diffraction peak of monoclinic  $\text{WO}_3$ .

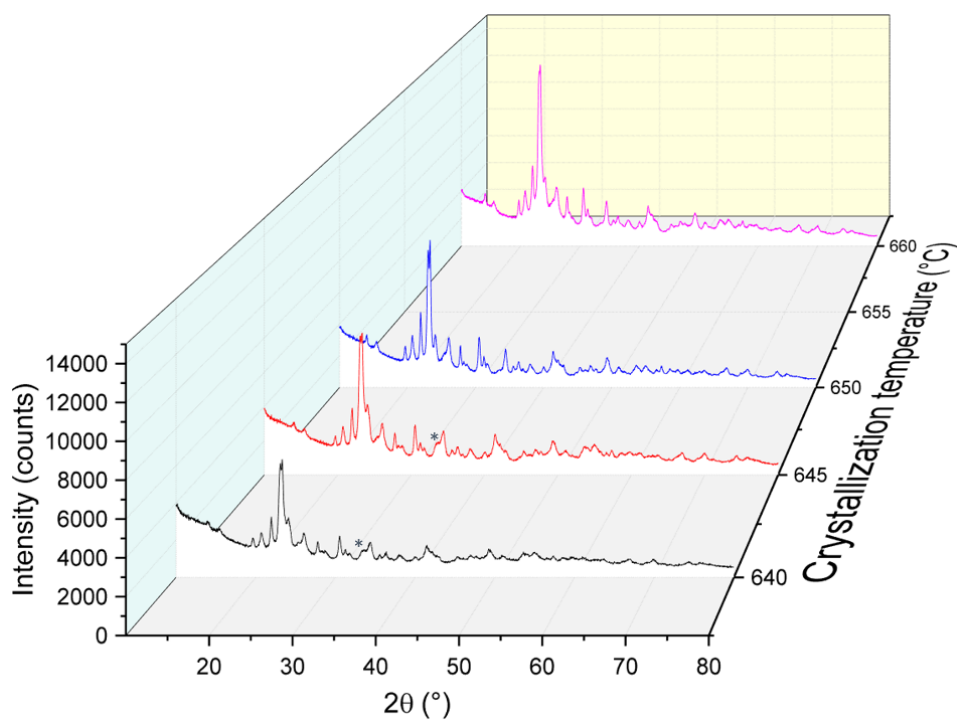


Figure 33: XRPD patterns of orthorhombic  $\text{Al}_2\text{W}_3\text{O}_{12}$  (0.005 M) obtained by NHSG route; \* stands for a diffraction peak of monoclinic  $\text{WO}_3$ .

The specific surface areas of crystallized samples are presented in Table 7. The theoretical density of the orthorhombic  $\text{Al}_2\text{W}_3\text{O}_{12}$  phase used for the average particle size ( $d_{\text{BET}}$ ) calculation was  $5.12 \text{ g cm}^{-3}$  [114]. Since the specific surface areas of amorphous powders were insignificant ( $< 2 \text{ m}^2 \text{ g}^{-1}$ ), these values and are not presented in Table 7. As can be seen, the increase in specific surface areas did not follow the decrease of calcination temperatures, as might be expected. For instance, Marzano et al., [33], affirmed that even small increases in the calcination temperature were unfavorable and provoked the formation of hard agglomerates in the case of the co-precipitated  $\text{Y}_2\text{W}_3\text{O}_{12}$  powders, resulting in reduction of the specific surface areas.

Table 7: Specific surface areas and the average particle sizes of orthorhombic  $\text{Al}_2\text{W}_3\text{O}_{12}$  powders, prepared by NHSG using different molarities and calcined at different temperatures.

Concentration of reagent solutions (M)	Calcination temperature ( $^{\circ}\text{C}$ )	Calcination Time (min)	BET ( $\text{m}^2 \text{ g}^{-1}$ )	$d_{\text{BET}}$ (nm)	Phase composition
0.1	950	300	N/A	N/A	Monophasic
0.1	650	20	20.5	57	$\text{Al}_2\text{W}_3\text{O}_{12} + \text{WO}_3$
0.1	640	20	26	45	$\text{Al}_2\text{W}_3\text{O}_{12} + \text{WO}_3$
0.1	635	20	19.7	59	$\text{Al}_2\text{W}_3\text{O}_{12} + \text{WO}_3$
0.1	630	20	13.5	87	$\text{Al}_2\text{W}_3\text{O}_{12} + \text{WO}_3$
0.1	625	20	11.9	98	$\text{Al}_2\text{W}_3\text{O}_{12} + \text{WO}_3$
0.1	600	20	16.4	71	$\text{Al}_2\text{W}_3\text{O}_{12} + \text{WO}_3$
0.005	660	20	12.9	91	Monophasic
0.005	650	20	9.4	125	Monophasic
0.005	645	20	7.2	163	$\text{Al}_2\text{W}_3\text{O}_{12} + \text{WO}_3$
0.005	640	20	12.1	97	$\text{Al}_2\text{W}_3\text{O}_{12} + \text{WO}_3$

It is important to note that according to Table 7, the highest specific surface area ( $26 \text{ m}^2 \text{ g}^{-1}$ ) for the powders using 0.1 M is ascribed to the sample calcined at  $640 \text{ }^{\circ}\text{C}$ , during 20 min, while the powders calcined at temperature  $< 640 \text{ }^{\circ}\text{C}$  presented lower surface area, probably, due to the presence of organics, eliminated, almost, completely only during the calcination step at slightly higher temperatures. Thus, it is understandable why the lowest specific surface area ( $1.7 \text{ m}^2 \text{ g}^{-1}$ ) was measured for amorphous precursor since this presented a high amount of organics.

On the other hand, the powders synthesized using 0.005 M solutions showed a lower specific surface area than the calcined powder prepared from 0.1 M reagents. Most likely the reason is Ostwald ripening phenomenon. The 0.005 M samples were kept in evaporation stage, at least, twice as much time (4 days) as for 0.1 M samples, which could allow for the dissolution of small particles, followed by re-precipitation on larger ones. This phenomenon generally occurs for a system to reach a more thermodynamically stable state with the lowest surface area [48-49].

Furthermore, the specific surface area of  $26 \text{ m}^2 \text{ g}^{-1}$  reached for  $640 \text{ }^\circ\text{C}$  (0.1 M) is quite significant when compared with the reported in the literature [10,79, 82,85]. Although Young et al., [74] reported the synthesis of  $\text{A}_2\text{M}_3\text{O}_{12}$ -type molybdates at very low temperatures ( $230 \text{ }^\circ\text{C}$ ), it was observed that tungstate counterparts, synthesized and processed under the same conditions, did not crystallize. Some additional heat treatments at temperatures around  $600 \text{ }^\circ\text{C}$  were necessary to induce crystallization in tungstates, in accord with the temperatures employed in our study.

It is relevant to point out that the previous studies on NHSG synthesis of tungstate or molybdate from  $\text{A}_2\text{M}_3\text{O}_{12}$  and related families did not report specific surface areas of the synthesized powders [74-77, 127,131].

To elucidate the advantages of NHSG to prepare  $\text{Al}_2\text{W}_3\text{O}_{12}$  powders in comparison with the reported co-precipitation methods, it is important to mention that typically, the latter occurs in an aqueous medium to produce a hydroxide-based amorphous precursor [34], rich in OH surface groups, which can bond with adjacent  $\text{OH}^-$  groups through hydrogen bonding during drying, increasing the agglomeration among primary particles. As the evaporation of water proceeds it can exert capillary forces and causes the collapse of the precursor pores, resulting in powders with low specific surface areas [65].

Conversely, the NHSG approach results in amorphous powders with different surface chemistry due to the presence of organic groups. One of the roles of organic groups on the particles within powder can be explained by the phenomenon of steric stabilization [133]. Steric stabilization is caused by organic material that forms polymeric chains and physically separates particles in powder. Moreover, during our NHSG synthesis alkyl halide are formed [65]. Although alkyl halides are polar, these are of a hydrophobic nature [134], eliminating the possibility

of hydrogen bonding during the drying step. Alkyl chloride, product of the reaction between metal chloride and metal alkoxide, undergoes elimination processes in the gas phase. Thus, the volatilization of these organic materials allows the formation of porous metal oxide powders [65]. Furthermore, the reduction of necking between the particles can be additionally explained by the volatilization of the remaining organic material acting to prevent agglomeration during the calcination stage [33, 135]. Therefore, agglomeration between particles is reduced through several processes such as lower capillary forces of the organic solvents, as previously mentioned, which allows for faster drying compared to hydrolytic gelling, steric contribution from polymer chains and volatilization of organic material.

The specific surface area of the powder  $\text{Al}_2\text{W}_3\text{O}_{12}$ \_NHS<sub>G</sub>\_0.1M (calcined at 640 °C) is at least 170 % higher than the specific surface areas obtained for  $\text{Al}_2\text{W}_3\text{O}_{12}$  phase by other soft-chemistry methods [10,79,82,85]. This implies a high potential of the NHS<sub>G</sub> method for preparation of porous and high surface area powders in the  $A_2M_3O_{12}$  family.

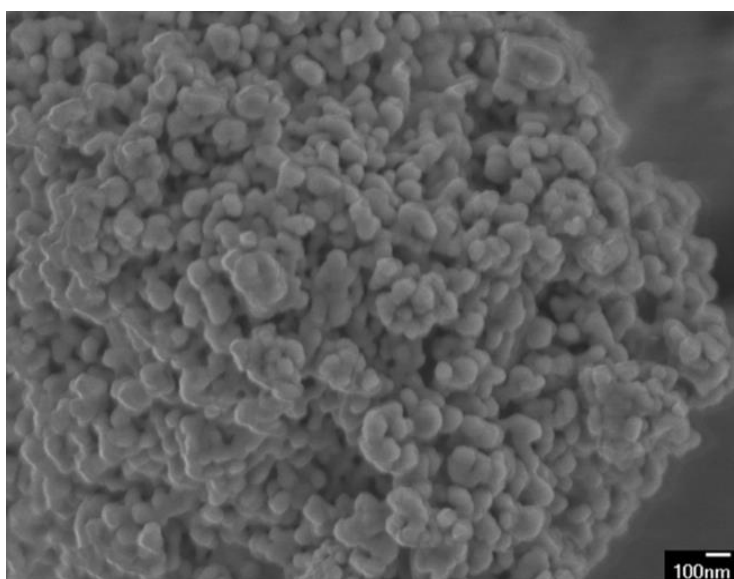


Figure 34: SEM images of monophasic orthorhombic  $\text{Al}_2\text{W}_3\text{O}_{12}$  (0.005 M) calcined at 660°C.

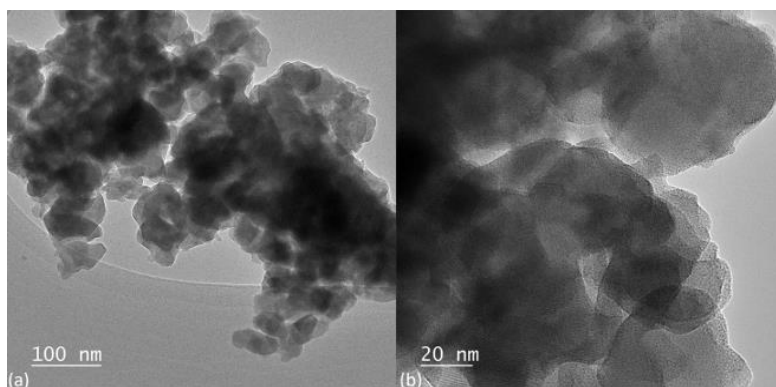


Figure 35: TEM images of monophasic orthorhombic  $\text{Al}_2\text{W}_3\text{O}_{12}$  (0.005 M). (a-b) Sample calcined at 660°C.

Based on the present study, the NHSG synthesis consisting of a total evaporation under stirring and calcination allowed the preparation of nanopowders with particles, smaller than 100 nm. Figure 34 and Figure 35 reveal nanometric size of primary particles of  $\text{Al}_2\text{W}_3\text{O}_{12}$  in the powder calcined at 660 °C (0.005 M). This is  $\text{Al}_2\text{W}_3\text{O}_{12}$  monophasic sample with the highest specific surface area within samples prepared from 0.005M. The SEM and TEM images show small, nanometric, rounded particles, in agreement with the assumption of the particles having a spherical shape used for the calculation of  $d_{\text{BET}}$ .

In addition, it is relevant for the viability of the NHSG method that the total duration of the synthesis proposed in this study was reduced to 2 or 4 days, depending on the molarity explored. Most of the previous reports [75-77, 131] on preparation of  $\text{A}_2\text{M}_3\text{O}_{12}$  phases by NHSG used a more laborious, sophisticated and time-consuming approach, taking more than one week to complete the procedure and to obtain a crystalline powder. The present study demonstrated that a simpler and quicker approach is viable for the preparation of  $\text{Al}_2\text{W}_3\text{O}_{12}$  powders with high surface area. However, there is still a need for optimization of the presented process to increase even more specific surface area and to eliminate the trace of the secondary  $\text{WO}_3$  phase in some of the powders.

## 5.4 Conclusions

This study found that  $\text{Al}_2\text{W}_3\text{O}_{12}$  nanopowder, with high surface area, can be prepared by the NHSG through a less laborious way than commonly reported in the literature for this type of ceramics. The synthesis time is far less than one week and there is no need for using cryogenic temperatures. The calcination time defined in this study (20 min) is shorter than that described in the literature, which also corroborates to avoid the formation of necks between the particles, during crystallization step. The sample with the highest specific area (0.1 M calcined at 640 °C) achieved specific surface area as high as  $26 \text{ m}^2 \text{ g}^{-1}$ .

Nonetheless, the results obtained for the molarity of 0.005 M could be more promising if the drying process would be exactly the same as that defined for the samples synthesized with 0.1 M of reactant solutions once the samples would be kept in the solvent for less time avoiding the Ostwald ripening. Furthermore, as the NHSG route is a water/moisture free synthesis, the evaporation rate is faster than the hydrolytic synthesis. Hence, the growth rate of the particles during drying (through Ostwald ripening) can be reduced decreasing the drying time.

Different types of solvents as well as calcination temperatures/times and drying times should be further studied to improve understanding of their impact on particle size (specific surface area) and eliminate the remaining secondary phases.

## 6.

### Evaluation of total evaporation route for the synthesis of zero thermal expansion $\text{ZrMgMo}_3\text{O}_{12}$ powders

#### 6.1

##### Background

Low and near-zero thermal expansion ceramics have captured great attention as potential engineering materials for thermal shock applications and as outstanding fillers for tailoring the thermal expansion coefficients (CTE) of different matrices [93]. The families of compounds exhibiting this unusual attribute have been widely described in the literature in the last more than 20 years [1,5,93,129-130, 136 -137], with special attention to  $A_2M_3O_{12}$  family members (and its sub-families such as  $ABM_3O_{12}$ ,  $ABM_2XO_{12}$ , and  $A_2MX_2O_{12}$ ) due to their chemical flexibility that allows for obtaining of a large variety of molybdates and tungstates with CTEs ranging from  $-12 \times 10^{-6}$  to  $2 \times 10^{-6} \text{ }^\circ\text{C}^{-1}$  [93].

The molybdates from  $A_2M_3O_{12}$  and related families are generally more hygroscopic than tungstates [138], a feature that makes more difficult their practical applications. This characteristic has been ascribed to the higher absorption energies of  $\text{H}_2\text{O}$  molecules within the molybdates [139]. In contrast to this,  $\text{ZrMgMo}_3\text{O}_{12}$  is not hygroscopic, since its packing fraction (reported to be 0.17) is greater in comparison to other  $A_2M_3O_{12}$  compounds that accommodate  $\text{H}_2\text{O}$  in their crystal frameworks [7]. This is an advantage since  $\text{ZrMgMo}_3\text{O}_{12}$  neither absorbs atmospheric humidity during storage nor forms hydrate agglomeration or becomes amorphous [7,140]. Orthorhombic  $\text{ZrMgMo}_3\text{O}_{12}$  is a potentially relevant material because of its near-zero CTE ( $-4.28 \times 10^{-7} \text{ K}^{-1}$  from room temperature until  $400 \text{ }^\circ\text{C}$ ) [140], a property extremely desirable for **i**) ceramics with high thermal shock resistance, and **ii**) composites with controlled thermal expansion [141-142]. In addition, unlike some  $A_2M_3O_{12}$  molybdates that undergo the monoclinic-to-orthorhombic transition at temperatures higher than room temperature,  $\text{ZrMgMo}_3\text{O}_{12}$  presents this phase transformation well below room temperature, at  $-126 \text{ }^\circ\text{C}$  [140]. Therefore, it remains in the orthorhombic phase in a very large span of temperatures, displaying its near-zero thermal expansion feature under ambient

conditions. The most common route to synthesize  $\text{ZrMgMo}_3\text{O}_{12}$  is through the traditional solid-state reaction [140,143-144], as detailed in Table 8. This approach can be summarized as follows: the reactants ( $\text{ZrO}_2$ ,  $\text{MgO}$ , and  $\text{MoO}_3$ ) are manually or mechanically mixed at stoichiometric ratios, and then, calcined at high temperatures (600-800 °C) for several hours to permit the interdiffusion of the ions [7]. Before calcination, thermal treatments at lower temperatures and/or milling can be also carried out to increase diffusion, as described in Table 8.

Table 8: Different synthesis routes for the preparation of  $\text{ZrMgMo}_3\text{O}_{12}$  and its solid solutions, as reported in the literature.

Synthesis route	Reactants	Pre-treatment	Calcination Conditions	Average particle size ( $\mu\text{m}$ ) (SEM analysis**)	Secondary phases	Ref.
I) Solid-state reaction ( $\text{ZrMgMo}_3\text{O}_{12}$ )	$\text{MgO}$ , $\text{ZrO}_2$ , $\text{MoO}_3$	Milling for 1 h	$T_1 = 800\text{ }^\circ\text{C}$ $t_1 = 4\text{ h}$	-	Non specified*	[143]
II) Solid-state reaction ( $\text{ZrMgMo}_3\text{O}_{12}$ )	$\text{MgO}$ , $\text{ZrO}_2$ , $\text{MoO}_3$	Milling for 18h	$T_1 = 650\text{ }^\circ\text{C}$ $t_1 = 5\text{ h}$	-	$\text{ZrMo}_2\text{O}_8$	[144]
			$T_1 = 700 - 750\text{ }^\circ\text{C}$ $t_1 = 5\text{ h}$	-	-	
			$T_1 = 800 - 850\text{ }^\circ\text{C}$ $t_1 = 5\text{ h}$	-	$\text{ZrO}_2$ , $\text{MgMoO}_4$	
			$T_1 = 700\text{ }^\circ\text{C}$ $t_1 = 5\text{ h}$	0.64	-	
			$T_1 = 700\text{ }^\circ\text{C}$ $t_1 = 5\text{ h}$ $T_2 = 700\text{ }^\circ\text{C}$ $t_2 = 5\text{ h}$	1.44	-	
III) Non-Hydrolytic Sol-Gel ( $\text{ZrMgMo}_3\text{O}_{12}$ )	$\text{MgCl}_2$ , $\text{Zr}(\text{OiPr})_4$ , $\text{HOiPr}$ , $\text{MoCl}_5$	-	$T_1 = 600\text{ }^\circ\text{C}$ $t_1 = 5\text{ h}$	> 5.00	$\text{MoO}_3$	[127]
IV) Total evaporation route in an aqueous medium ( $\text{In}_{0.5}(\text{ZrMg})_{0.75}\text{Mo}_3\text{O}_{12}$ )	$\text{Mg}(\text{NO}_3)_2$ , $\text{In}(\text{NO}_3)_3$ , $(\text{NH}_4)_6\text{Mo}_7\text{O}_{24} \cdot 4\text{H}_2\text{O}$ , $\text{ZrO}(\text{NO}_3)_2$ dissolved with $\text{HNO}_3$	Total evaporation under magnetic stirring: ( $T = 70\text{ }^\circ\text{C}$ , $t = 12\text{ h}$ )  Thermal treatment: drying of the precursor ( $T = 100\text{ }^\circ\text{C}$ , $t = 8\text{ h}$ )	$T_1 = 750\text{ }^\circ\text{C}$ $t_1 = 5\text{ h}$ $T_2 = 800\text{ }^\circ\text{C}$ $t_2 = 1\text{ min}$	0.70 - 1.60	-	[138]
V) Solid-state reaction ( $\text{ZrMg}_{1-x}\text{Zn}_x\text{Mo}_3\text{O}_{12}$ )	$\text{ZnO}$ , $\text{MgO}$ , $\text{ZrO}_2$ , $\text{MoO}_3$	Thermal treatment ( $T = 500\text{ }^\circ\text{C}$ , $t = 1\text{ h}$ , followed by milling for 2 h).	$T_1 = 800\text{ }^\circ\text{C}$ $t_1 = 5\text{ h}$	-	$\text{ZrMo}_2\text{O}_8 + \text{ZrO}_2$	[140]

\* Peaks of secondary phases are present, but not identified.

\*\* Scanning Electron Microscopy (SEM) analysis

The solid-state reaction is a synthesis classified as high energy since requires high processing temperatures and times [145]. The obtaining of a single-phase powder is strongly related to the homogeneity of the reactant mixture, which is achieved by thorough grinding of the metal oxide reagents. However, typically, the

produced powders are multiphasic, with large particles and hard agglomerates due to the high temperatures and long times required for calcination, promoting necking between the adjacent particles [146]. The synthesis of  $\text{ZrMgMo}_3\text{O}_{12}$  powders through soft-chemistry approaches would, in theory, result in a more homogeneous ion mixture, followed by a significant decrease in the calcination temperatures and times. Thus, this route could favor the preparation of  $\text{ZrMgMo}_3\text{O}_{12}$  with smaller crystallites/particles and the formation of less agglomerated powders [127]. Nonetheless, the synthesis of  $\text{ZrMgMo}_3\text{O}_{12}$ , or other phases from the  $\text{ABM}_3\text{O}_{12}$  sub-family, by soft-chemistry approaches has only been reported in a few works, as described as follows.

For instance, Baiz et al. [131] prepared  $\text{ZrMgW}_3\text{O}_{12}$  by non-hydrolytic sol-gel (NHSG) method. Those authors reported the presence of impurity phases after calcination, but these were not specified. This powder was calcined in a shorter time and at lower temperatures, in comparison with those required for the solid-state reaction method. However, the temperatures  $< 540$  °C led to not well-crystallized  $\text{ZrMgW}_3\text{O}_{12}$  with the presence of secondary phases. When the conditions of the thermal treatment were 400 °C for 3 h, followed by second heating up to 1050 °C with 0.5 h holding time,  $\text{ZrMgW}_3\text{O}_{12}$  was completely crystallized, although  $\text{ZrO}_2$  also appeared in traces.

Lind et al. [127] synthesized  $\text{ZrMgMo}_3\text{O}_{12}$  phase by NHSG using 1 mmol of  $\text{Zr}(\text{OiPr})_4 \cdot \text{HOiPr}$ , 1 mmol of  $\text{MgCl}_2$ , and 3 mmol of  $\text{MoCl}_5$ . The as-prepared powders were heat treated at 600 °C for 5 h. The as-obtained  $\text{ZrMgMo}_3\text{O}_{12}$  powder was not completely monophasic ( $\text{MoO}_3$  was found as a secondary phase) and the average particle sizes were higher than 5  $\mu\text{m}$ .

Additionally, Prisco et al. [138] synthesized  $\text{In}_{0.5}(\text{ZrMg})_{0.75}\text{Mo}_3\text{O}_{12}$  through a total evaporation route, *viz.* a soft-chemistry method where the supersaturation conditions for the co-precipitation of an amorphous hydroxide-based precursor comprising of  $\text{In}^{3+}$ ,  $\text{Mg}^{2+}$ ,  $\text{Zr}^{4+}$ , and  $\text{Mo}^{6+}$  was achieved by the complete solvent evaporation [147-149]. The authors prepared a stoichiometric mixture of 0.1 M aqueous solutions of metal salts. It is worth noting that the reactant  $\text{ZrO}(\text{NO}_3)_2$  was insoluble in water, therefore, 100 mL of  $\text{HNO}_3$  were added until the complete dissolution of this reactant. The solution of reactants, obtained by the mixture of 0.1 M aqueous solutions of salt reagents presented in Table 8, was magnetically

stirred, and heated at 75 °C for approximately 12 h until complete solvent evaporation. Afterwards, the precipitated precursor was oven dried at 100 °C for 8 h and calcination was performed at 750 °C for 5 h, followed by a rapid heating to 800 °C with the dwell time of 1min. The as-obtained powder was monophasic with monoclinic  $\text{In}_{0.5}(\text{ZrMg})_{0.75}\text{Mo}_3\text{O}_{12}$  as the only phase. Therefore, this method can be potentially useful for preparation of  $\text{ZrMgMo}_3\text{O}_{12}$  powders.

This work aimed to preliminary evaluate the total evaporation route for the synthesis of highly dispersed and monophasic  $\text{ZrMgMo}_3\text{O}_{12}$  powders. The phase composition of all prepared powder was verified through quantitative X-ray powder diffraction analysis, while the specific surface area and average particle size were evaluated by  $\text{N}_2$  adsorption and Scanning Electron Microscopy for the most promising powder.

## 6.2

### Materials and methods

#### 6.2.1. Total evaporation route

The synthesis of the  $\text{ZrMgMo}_3\text{O}_{12}$  was conducted, using 0.1 M aqueous solutions of salt reactants. First, 100 mL of nitric acid were spilled into 25 ml of  $(\text{NH}_4)_6\text{Mo}_7\text{O}_{24}\cdot 4\text{H}_2\text{O}$  (Isofar, 99%) solution. Afterwards, 25 ml of  $\text{Zr}(\text{NO}_3)_4\cdot 5\text{H}_2\text{O}$  (Isofar, 99%) solution was poured into the initial solution containing nitric acid and the ammonium molybdate. Then, 10.7 ml of  $\text{Mg}(\text{NO}_3)_2\cdot 6\text{H}_2\text{O}$  (Vetec, 99%) solution was added to form the final solution. Note that nitric acid was used to keep the pH highly acid to avoid any partial precipitation. Therefore, no precipitation occurred instantaneously due to the very low pH, lower than 1, (*vide infra*). The final solution was kept under magnetic stirring at 75 °C for 24 h until total evaporation of water and acid. The mean rate of evaporation was  $12.5 \text{ mL h}^{-1}$ . The precipitation took part during the evaporation of the resultant aqueous solution and a yellowish powder was formed. No further treatment was performed at the end of evaporation once the powder was fully dried, i.e., there was no need for centrifugation, washing, or additional drying. The precursor was introduced in a tubular furnace (Maitec-INTI FET 1600/H furnace; São Carlos, Brazil) after the desired temperature was achieved (the chosen temperatures were based on thermogravimetric analysis (TGA) and differential scanning calorimetry (DSC),

*vide infra*), and kept there during 20 min. Afterwards, the powders were removed and quenched in air to room temperature.

The scheme of total evaporation synthesis is shown in detail in Figure 36, and the final amorphous precursor powder was denoted as  $\text{pZrMgMo}_3\text{O}_{12\_ET}$ , while calcined samples were denoted as  $S_y$ , where “y” is assigned to the chosen calcination temperature (“y” = 500, 550, 600, 700 and 800 °C).

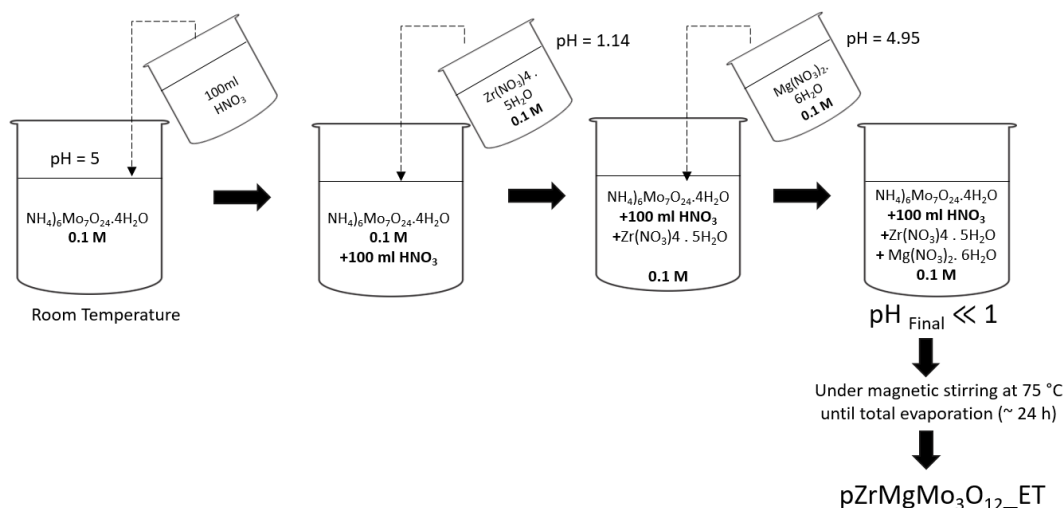


Figure 36: Total evaporation route for synthesis of orthorhombic  $\text{ZrMgMo}_3\text{O}_{12}$ .

### 6.2.2. Characterization of amorphous precursors and calcined powders

The amorphous  $\text{ZrMgMo}_3\text{O}_{12}$  precursors were analyzed by TGA/DSC in a PerkinElmer Simultaneous Thermal Analyzer STA-6000 (Seer Green, U.K.) with a heating rate of  $20\text{ °C min}^{-1}$ , under air flow of  $20\text{ mL min}^{-1}$  in an alumina crucible, for determination of the crystallization temperature and weight losses.

The as-prepared powders (see section 6.2.1) were characterized by X-ray powder diffraction (XRPD) at room temperature, in a D8 Advance X-ray diffractometer (Bruker, Karlsruhe, Germany), using  $\text{CuK}_\alpha$  radiation at  $0.02^\circ$  ( $2\theta$ ) step, with an acquisition time of 2 s per step, from  $10^\circ$  to  $80^\circ$  ( $2\theta$ ).

The phase composition was determined using the PDF-4+ 2022 database [150], and the quantitative analysis for each powder diffraction pattern of samples obtained at different calcination temperatures was carried out using Jade MDI (2022) software. Whole pattern fitting was done using the Pawley method, where

the refined parameters include background, lattice, and profile parameters. Refined scale factors are applied to the integrated intensities or peak areas in profile refinement. Reference intensity ration (RIR) is calculated from refined phases by normalizing intensities of a structure phase to its density, thus making the scale factors directly proportional to the weight fractions of structure phases.

Field-emission scanning electron microscopy (FE-SEM) was performed in JSM-6701F equipment (JEOL, Tokyo, Japan), in secondary electron mode, operating at 1 kV, to evaluate the morphology and the average size of the  $\text{ZrMgMo}_3\text{O}_{12}$  particles. The powder was coated with carbon film.

The specific surface area was determined by the nitrogen adsorption method at - 196 °C using a TriStar 3020 V1.03 (Micromeritics, USA) and applying the Brunauer–Emmett–Teller (BET) approach. Furthermore, the average particle size ( $d_{\text{BET}}$ ) was calculated based on the measured specific surface area, assuming spherical shapes for the particles.

### 6.3 Results and discussions

Figure 37 shows the TGA/DSC curves of amorphous precursor ( $\text{pZrMgMo}_3\text{O}_{12\_ET}$ ) prepared by a total evaporation method. The initial endothermic peaks, situated at 25 – 200 °C, are associated with the release of the remaining water, while the endo peaks in the 200 – 500 °C range can be ascribed to the release of volatile species (such as  $\text{NH}_3$ ,  $\text{N}_2\text{O}$ , and  $\text{NO}$  [151]) since the powders have not been washed after synthesis (totalizing a weight loss ~ 45% up to 500 °C). At 550 °C there is a faint exothermic peak possibly related to  $\text{ZrMgMo}_3\text{O}_{12}$  crystallization, noticed as the change in DSC curve slope. This event is also presented in a previous report on  $\text{ZrMgMo}_3\text{O}_{12}$  preparation [144]. The faint feature at ~ 750 °C may correspond to the start of  $\text{ZrMgMo}_3\text{O}_{12}$  decomposition [7,144].

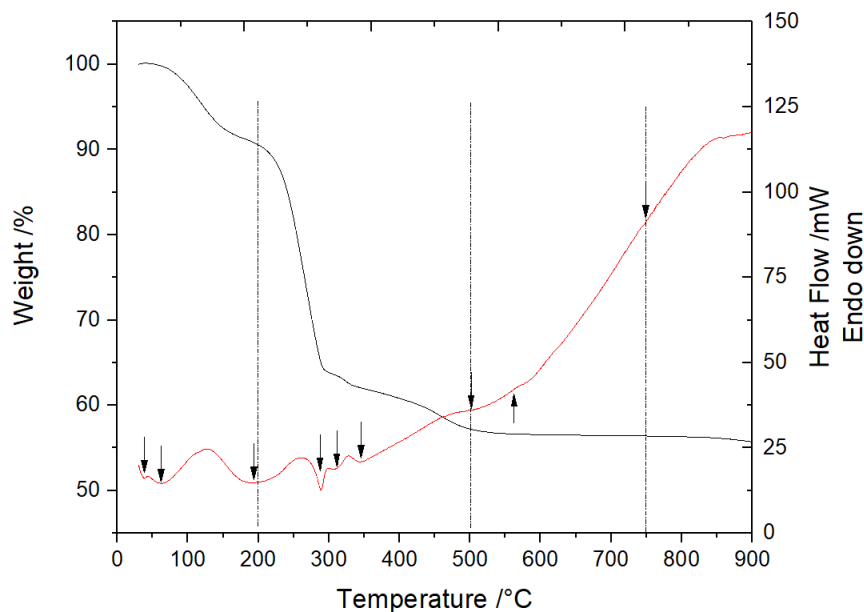


Figure 37: TGA and DSC curves of the precursor powder ( $\text{pZrMgMo}_3\text{O}_{12\_ET}$ ). Endothermic peaks are marked as ↓, and the exothermic peak is marked as ↑.

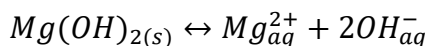
When co-precipitation occurs from salt aqueous solutions, formation of amorphous oxyhydroxide or hydroxide-based precursors is expected, containing the cations present in the solutions [34]. The precipitation of amorphous precursor starts when a non-equilibrium condition, called supersaturation, is attained [149]. Supersaturation, which is the driving force for the precipitation [152], can be achieved by different chemical and physical means such as pH change (normally adding a base); solvent evaporation at a constant temperature; change of temperature or pressure; oxidation-reduction reactions, and by addition of other solutes or solvents [147-148]. Before achieving the supersaturation condition, all aqueous solutions, containing the desired cations, should be mixed into a unique solution avoiding the precipitation of a part of the mixed cations. This can be a real challenge whenever the cation salt aqueous solutions possess different precipitation pH values for the formation of the corresponding hydroxide, as it is in the case of the reagents commonly selected for the synthesis of  $\text{ZrMgMo}_3\text{O}_{12}$  powders by soft-chemistry approaches.

According to Kobayashi et al. [153], the precipitation pH for  $\text{Zr}(\text{OH})_4$  is situated above 1.5. On the other hand, the precipitation of molybdenum in aqueous solution is not trivial due to the instability of its electronic structure, allowing a variation of the valency of this element [154-155].  $\text{Mo}^{6+}$  exists in alkaline or weak

acid medium, MoO<sub>4</sub><sup>2-</sup>, but as the pH decreases it is possible to form HMoO<sub>4</sub><sup>-</sup> under weak acid conditions. Moreover, in an extremely acidic medium (pH =1), molybdenum exists as MoO<sub>3</sub>·2H<sub>2</sub>O [154]. Yatirajam et. al [156], reported that Mo<sup>6+</sup> does not precipitate as hydroxides in an acid or alkaline medium, although Mo<sup>5+</sup> hydroxide can be precipitated between pH 5 and 5.8. Although the authors [156] did not explicit the reaction, “molybdenum (V) hydroxide” is assigned in the literature as MoO(OH)<sub>3</sub> [157].

The precipitation of zirconium and magnesium hydroxides, simultaneously, is another challenge due to the opposite pH necessary for precipitation of these compounds, *i.e.*, zirconium hydroxide precipitates in an acid medium, while magnesium hydroxides precipitate in a weak alkaline pH [158]. Note that Yamagata et al. [159], studied the precipitation of Mg(OH)<sub>2</sub> with the addition of NH<sub>4</sub>OH solution, controlling the pH between 10.6 – 11, and reported the formation of soluble complexes of ammonia with magnesium, promoting incomplete precipitation of magnesium hydroxide, which varied from 39.3 - 98.8%. The authors concluded that keeping the pH constant is not enough to control the precipitation of Mg(OH)<sub>2</sub> with NH<sub>4</sub>OH.

The dissociation equilibrium for magnesium hydroxide is described as per below:



The solubility product constant, K<sub>sp</sub>, of Mg(OH)<sub>2</sub> near 25°C is 3.4 x 10<sup>-11</sup> [160]. Thus, the calculation of the pH at which Mg(OH)<sub>2</sub> begins to precipitate from a 0.1 M solution is described as follows:

$$K_{sp} = [Mg^{2+}] \cdot [OH^{-}]^2 = 3.4 \times 10^{-11}$$

$$[OH^{-}] = \sqrt{\frac{K_{sp}}{[Mg^{2+}]}} = \sqrt{\frac{3.4 \times 10^{-11}}{0.1}} = 1.84 \times 10^{-5}$$

$$pOH = -\log([OH]^{-}) \sim 5$$

$$pOH + pH = 14$$

$$pH = 14 - 5 = 9$$

Therefore, it appears that for pH above 9, the solution should become supersaturated, and the magnesium hydroxide would precipitate.

The synthesis route reported in this work, performed by total evaporation of the solvent, however, allowed for the preparation of an amorphous precursor powder which resulted in predominantly crystalline ZrMgMo<sub>3</sub>O<sub>12</sub> powder after rapid calcination (*vide infra*). This can be explained through the addition of HNO<sub>3</sub> since when added in a solution of three salts, such as (NH<sub>4</sub>)<sub>6</sub>Mo<sub>7</sub>O<sub>24</sub>·4H<sub>2</sub>O, Zr(NO<sub>3</sub>)<sub>4</sub>·5H<sub>2</sub>O, and Mg(NO<sub>3</sub>)<sub>2</sub>·6H<sub>2</sub>O, it avoids preferential precipitation of one, or two cations, due to very low pH (<< 1) which is not appropriate for precipitation of any of the three cations. The pH of the resultant solution did not change over time and was kept below 1 during the entire process. After 3 h under stirring at 75 °C, the precipitation of the powder started, owing to supersaturation caused by solvent partial evaporation, and the solution changed from transparent to white cloudy, followed by a yellowish dispersion. Hence, the precipitation was not controlled by pH, but by the concentration of the cations in the solution which was increased during solvent evaporation, eventually reaching the supersaturation state.

Table 9 shows the different calcination temperatures and times, along with the respective phase compositions of the obtained powders.

Table 9: Phase composition of crystallized powders, prepared by total evaporation, followed by rapid calcination at different temperatures and times.

Calcined Sample	Calcination temperature (°C)	Time (min)	Phase composition
S <sub>500</sub>	500	40	ZrMgMo <sub>3</sub> O <sub>12</sub> + ZrMo <sub>2</sub> O <sub>8</sub> + MoO <sub>3</sub>
S <sub>550</sub>	550	20	ZrMgMo <sub>3</sub> O <sub>12</sub> + ZrMo <sub>2</sub> O <sub>8</sub> + MoO <sub>3</sub>
S <sub>600</sub>	600	20	ZrMgMo <sub>3</sub> O <sub>12</sub> + ZrMo <sub>2</sub> O <sub>8</sub> + MoO <sub>3</sub> + ZrO <sub>2</sub>
S <sub>700</sub>	700	20	ZrMgMo <sub>3</sub> O <sub>12</sub> + ZrMo <sub>2</sub> O <sub>8</sub> + MoO <sub>3</sub>
S <sub>800</sub>	800	300	ZrMgMo <sub>3</sub> O <sub>12</sub> + MgMoO <sub>4</sub> + MoO <sub>3</sub> + ZrO <sub>2</sub>

XRPD patterns (Figure 38) show predominantly crystalline feature independent of the calcination temperature, although amorphous precursor was present in lower content in the powders calcined between 500 and 700°C (Table 10). It is important to note that the synthesized powders were not monophasic, once the patterns revealed the formation of hexagonal ZrMo<sub>2</sub>O<sub>8</sub> (Powder Diffraction File (PDF): 78-3070), a monoclinic β-MoO<sub>3</sub> (PDF: 85-2405 for sample S<sub>500</sub>), an

orthorhombic  $\alpha$ -  $\text{MoO}_3$  (PDF: 005-0508 for samples calcined above 500 °C),  $\text{MgMoO}_4$  (PDF: 21-0961) and  $\text{ZrO}_2$  (PDF: 03-065-1022) depending on the calcination temperature.

To evaluate the percentage of orthorhombic  $\text{ZrMgMo}_3\text{O}_{12}$  (PDF: 67-0300) and the amount of secondary, crystalline, and amorphous phases present in the samples, a quantitative analysis of XRPD data was performed, as previously described, and the results were summarized in Table 10.

Table 10: Quantitative phase analysis of the powders crystallized at different temperatures and times.

Phase composition (wt. %)	Samples				
	S500	S550	S600	S700	S800
$\text{ZrMgMo}_3\text{O}_{12}$	48.0	66.8	62.4	64.9	72.8
$\text{ZrMo}_2\text{O}_8$	13.0	4.0	7.0	12.2	-
$\text{MoO}_3$	24.6	15.9	18.8	17.0	0.8
$\text{ZrO}_2$	-	-	5.4	-	13.6
$\text{MgMoO}_4$	-	-	-	-	12.7
Amorphous	14.3	13.3	6.6	5.9	-

Despite Yang et al.[144], reported that the lowest synthesis temperature for preparing a monophasic  $\text{ZrMgMo}_3\text{O}_{12}$  powder was  $\sim 700$  °C, in our study amounts of  $\text{ZrMo}_2\text{O}_8$ ,  $\text{MoO}_3$ , and amorphous precursor were still present in  $S_{700}$  sample. In contrast, another research [144] reported the presence of  $\text{ZrO}_2$  within the calcination temperature range between 750 °C and 850 °C. This compound was also found, in a significant amount, for the  $S_{800}$  sample. Although raising the crystallization temperature caused an increase in the percentage of the orthorhombic  $\text{ZrMgMo}_3\text{O}_{12}$  phase and a decrease in amorphous precursor, it also, promoted the formation of  $\text{ZrO}_2$  and  $\text{MgMoO}_4$ . The  $\text{ZrO}_2$  and  $\text{MgMoO}_4$  phases identified after calcination at 800 °C might be a consequence of the partial decomposition of  $\text{ZrMgMo}_3\text{O}_{12}$  [7,144].

Madrid et al. [141], synthesized  $\text{ZrMg}_{1-x}\text{Zn}_x\text{Mo}_3\text{O}_{12}$  through solid-state reaction for  $x = 0.1, 0.30, 0.35$  and  $0.40$ , identifying for compositions up to  $x = 0.35$ , the presence of hexagonal  $\text{ZrMo}_2\text{O}_8$  ( $P3_1C$  space group; PDF:78-3070) as

secondary phase, as well. In addition, for  $x = 0.40$ , the authors identified the monoclinic  $\text{ZnMoO}_4$  phase (C2/m setting), as a secondary phase.

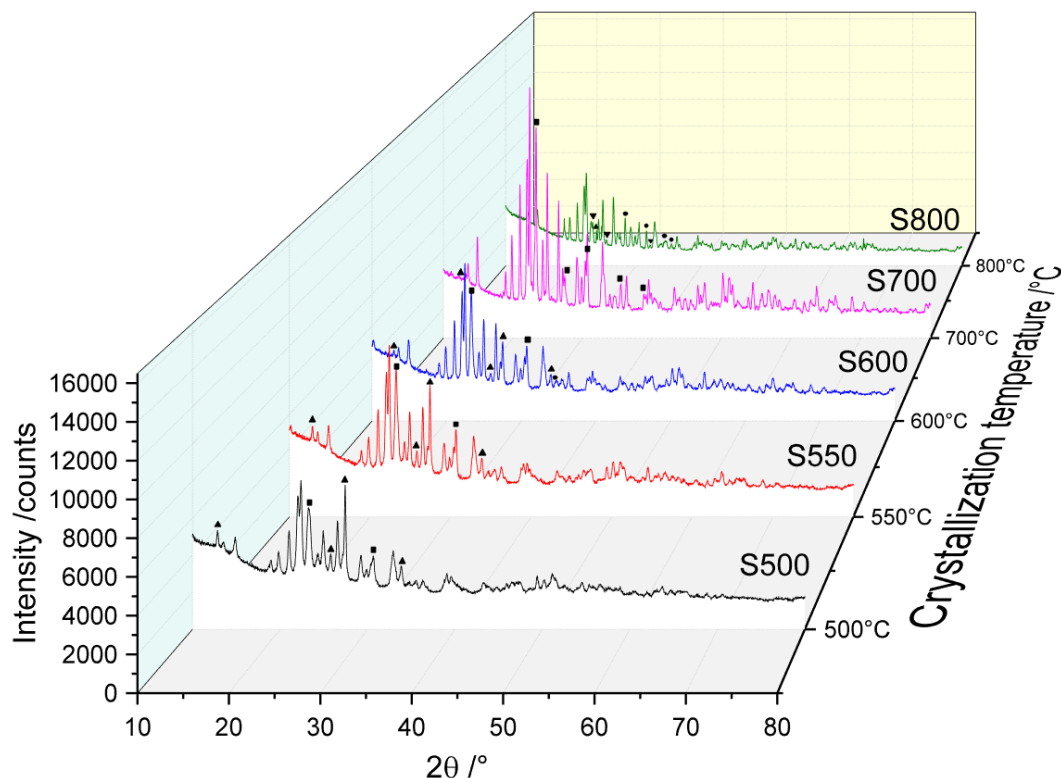


Figure 38: XRPD patterns of calcined powders.  $\text{ZrMo}_2\text{O}_8$  diffraction lines are marked as ■,  $\text{ZrO}_2$  peaks are marked as ●,  $\text{MgMoO}_4$  peaks are marked as ▼, and peaks related to  $\text{MoO}_3$  are marked with ▲. The main phase is orthorhombic  $\text{ZrMgMo}_3\text{O}_{12}$ .

Despite the specific surface area of  $\text{ZrMgMo}_3\text{O}_{12}$  not being reported in previous studies (see Table 8), it was evaluated for the sample S700. Although the result cannot be fully attributed to  $\text{ZrMgMo}_3\text{O}_{12}$  phase, since  $\sim 35\%$  of secondary phases are still present, it provides an estimative of the average size of particles, as confirmed by SEM images (Figure 39). The theoretical density of the orthorhombic  $\text{ZrMgMo}_3\text{O}_{12}$  phase used for the average particle size ( $d_{\text{BET}}$ ) calculation was  $3.3 \text{ g cm}^{-3}$  [144]. The obtained value of a specific surface area of  $\sim 4.0 \text{ m}^2\text{g}^{-1}$  would correspond to an average particle size of  $\sim 460 \text{ nm}$  of the main  $\text{ZrMgMo}_3\text{O}_{12}$  phase. Figure 39 shows the powder calcined at  $700^\circ\text{C}$ , revealing agglomerated submicronic particles in accordance with the estimation based on the surface area.

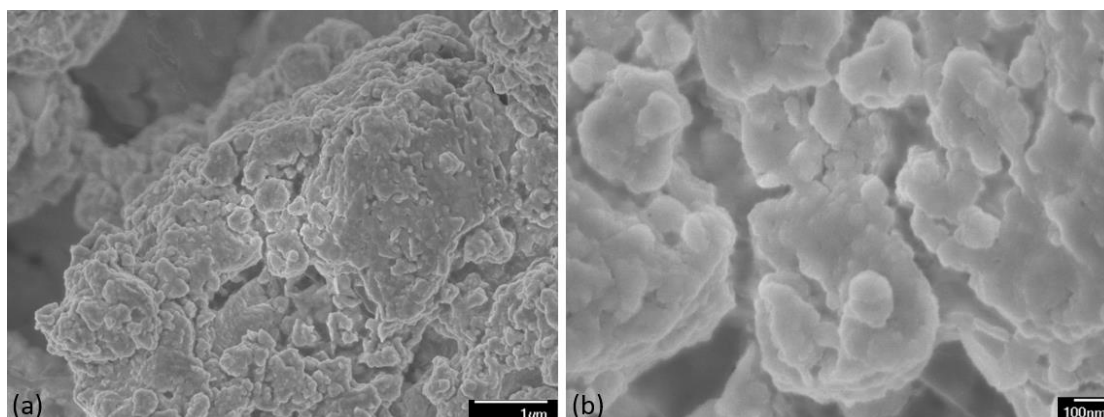


Figure 39: SEM images of the sample calcined at 700°C

Despite the methodology of our synthesis followed a rigorous protocol, based on the principles of the solvent evaporation controlled precipitation, a monophasic powder has not been achieved for the conditions (type of starting reagents, molarity, calcination temperatures, and times) tested in this study.

Lind et al. [127] synthesized  $\text{ZrMgMo}_3\text{O}_{12}$  phase by NHSG with  $\text{MoO}_3$  traces. The authors suggested the reduction of  $\text{MoCl}_5$  from 3 mmol to 2.5 mmol to achieve a pure phase based on a previous study on  $\text{Ga}_2\text{Mo}_3\text{O}_{12}$ . However, the as-prepared powder still presented micron-sized particles (see Table 8). This could be attributed to the long calcination time (5 h).

Based on the present study, despite the high amount of the secondary phase (35 %) after the calcination at 700 °C during merely 20 min, it was possible to synthesize orthorhombic  $\text{ZrMgMo}_3\text{O}_{12}$  by total evaporation route. The evaluation has been performed in a range of calcination temperatures from 500 - 800 °C, using uniformly 20 min for crystallization. Thus, calcination temperature and times might be additionally optimized to achieve monophasic and dispersed  $\text{ZrMgMo}_3\text{O}_{12}$  powders. In addition, the  $\text{Zr}(\text{NO}_3)_4 \cdot 5\text{H}_2\text{O}$  reactant could be replaced by the zirconium (IV) oxynitrate hydrate in order to obtain monophasic, as reported by Prisco et. al [138] for a parent phase. Another modification of the process, to eliminate the secondary phases, would be the decrease in the concentrations of the starting salt aqueous solutions from 0.1 M to 0.0025 M, as proposed by Lind et al. [127].

## 6.4 Conclusions

Total evaporation route has been preliminarily evaluated for the synthesis of  $\text{ZrMgMo}_3\text{O}_{12}$  powders under different calcination conditions. The applied synthesis parameters (type of starting reagents, their molarity, calcination temperatures, and times) did not result in fully monophasic powders. The as-prepared powders contained, at least, 27% of secondary phases, as achieved for the sample calcined at 800 °C for 5 h. Calcinations at temperatures between 500 and 700 °C maintained a percentage of amorphous phase, together with an amount of secondary phases.

Our preliminary evaluation of total evaporation method for precipitation of pure, monophasic,  $\text{ZrMgMo}_3\text{O}_{12}$  powders showed that the studied parameters such as starting reagents, molarity of solutions, and calcination temperatures and times were not adequate for the preparation of monophasic powders with high specific surface area.

This pitfall might be solved by decreasing the molarity of the starting reagents or even by further adjustment of the calcination temperatures ( $550\text{ °C} < T < 700\text{ °C}$ ) and times, since the decomposition of the  $\text{ZrMgMo}_3\text{O}_{12}$  should be avoided, and also secondary phases could be eliminated. In addition, starting salts can be modified, for example by substitution of  $\text{Zr}(\text{NO}_3)_4 \cdot 5\text{H}_2\text{O}$  for  $\text{ZrO}(\text{NO}_3)_2$ , to evaluate their effect on the phase composition of the powders.

## 7.

### Conclusions and future works

Submicronic powders of two phases from  $A_2M_3O_{12}$  ceramic family were synthesized by different coprecipitation methods and, also, by the non-hydrolytic sol-gel method. Different parameters of synthesis that influence the agglomeration state of  $A_2M_3O_{12}$  powders, such as molarity and temperature of calcination, have been evaluated since the agglomeration of the powder can restrict their application due to lower sinterability and the consequent decrease of the mechanical properties which are important for the applications that require high thermal shock resistance.

$Al_2W_3O_{12}$  was synthesized *via* co-precipitation, which includes i) mixing of reactants at room temperature, ii) mixing of reactants at 3.5 °C, iii) mixing of reactants with CTAB surfactant addition, and by NHSG route.

#### **$Al_2W_3O_{12}$ synthesis by co-precipitation:**

- Mixing reactants at room temperature (Method A): The highest specific surface area was reached through the lower molarity of precursor reagents. Thus, the supersaturation of the initial solution should be lower to minimize the period of the simultaneousness of nucleation and particle growth.
- Mixing reactants at 3.5 °C (Method A35): The decrease in the synthesis temperature induced a supersaturation stage which stabilizes the precipitate and controls the crystals growth, leading to an increase in specific surface area.
- Mixing reactants with CTAB surfactant addition (Method CTAB): The increment in the temperature was fundamental to avoid the formation of micelles due to the high concentration of surfactant used. The results of this method using temperature above the room temperature showed specific surface areas close to method A35 (mixing reactants at 3.5 °C) and higher than method A when 0.1 M was used (mixing reactants at room temperature).

- The most promising result for the amorphous precursor powders was reached for 0.005 M through method A and A35. The specific surface areas were  $34.6 \text{ m}^2 \text{ g}^{-1}$  and  $39.15 \text{ m}^2 \text{ g}^{-1}$ , respectively. Thus, for this system, lower concentrations of starting salts promotes homogeneous average small particle size than higher concentrations once the initial particles nucleated grow while the last small particles nucleated agglomerates leading to the decrease of specific surface area.
- The crystallized powder which presented the highest specific surface area, as high as  $29.5 \text{ m}^2 \text{ g}^{-1}$ , was reached for the sample synthesized with 0.005 M by mixing reactants at room temperature (method A) and calcined at  $635 \text{ }^\circ\text{C}$  during 20 min.
- Our results found that aging time did not affect the crystallization of amorphous powders, keeping them amorphous.

#### **$\text{Al}_2\text{W}_3\text{O}_{12}$ synthesis by NHSG route:**

- $\text{Al}_2\text{W}_3\text{O}_{12}$  nanopowder, with high surface area, can be prepared by the NHSG through a less laborious and faster way than the commonly reported in the literature for this type of ceramics.
- The synthesis time is far less than one week and there is no need for using cryogenic temperatures.
- The calcination time defined in this study (20 min) is shorter than the reported in the literature, which also corroborates to avoid the formation of hard agglomerates, during crystallization step.
- The powder with the highest specific area, as high as  $26 \text{ m}^2 \text{ g}^{-1}$ , was the one prepared using 0.1 M and calcined at  $640 \text{ }^\circ\text{C}$ .

#### **$\text{ZrMgMo}_3\text{O}_{12}$ synthesis by total evaporation.**

- Orthorhombic  $\text{ZrMgMo}_3\text{O}_{12}$  powder was synthesized using total evaporation route. Although different calcination temperatures were tested a completely monophasic powder was not attained.

- Lower calcination temperature and time were used for crystallization of near-zero thermal expansion  $\text{ZrMgMo}_3\text{O}_{12}$  material in comparison with the traditional solid state method.
- Despite the applied methodology, based on the fundamentals of precipitation controlled by the concentration of the cations in solution, a monophasic powder has not been achieved.

Based on the as-presented conclusions, the following proposals were suggested for future work:

#### **$\text{Al}_2\text{W}_3\text{O}_{12}$ synthesis by co-precipitation**

- To evaluate method A using higher pH.
- Other co-precipitation routes such as, for example, by dripping the reactants in a controlled manner can be explored. This step can be performed with or without surfactant addition.
- Modification of Method A, by surfactant addition after precipitation can be also a promising route to keep the nanometric powders dispersed after calcination due the volatilization of surfactant.

#### **$\text{Al}_2\text{W}_3\text{O}_{12}$ synthesis by NHSG route:**

- Different types of solvents, as well as, calcination temperatures/times and drying temperatures/times should be further studied to improve understanding of their impact on primary particle size (specific surface area) and on complete elimination of the residues of secondary phases.

#### **$\text{ZrMgMo}_3\text{O}_{12}$ synthesis by total evaporation route**

- The secondary phases could be eliminated by decreasing the molarity of the starting reagents.
- Further adjustment of the calcination temperature ( $600\text{ }^\circ\text{C} < T < 700\text{ }^\circ\text{C}$ ) and time. The starting salts can be, also, changed by substitution of  $\text{Zr}(\text{NO}_3)_4 \cdot 5\text{H}_2\text{O}$  for  $\text{ZrO}(\text{NO}_3)_2$ , to evaluate their effect on the phase composition of the powders.

**8.****References**

- [1] C.P. Romao, K.J. Miller, C.A. Whitman, M.A. White, B.A. Marinkovic, Negative Thermal Expansion (Thermomiotic) Materials, in: *Compr. Inorg. Chem. II* (Second Ed. From Elem. to Appl., Elsevier Ltd., 2013: pp. 127–151. doi:10.1016/B978-0-08-097774-4.00425-3.
- [2] M. BARSOUM, *Fundamentals of Ceramic*, 2003.
- [3] A. Mathew, *Lattice Vibrations – Phonons in Solid State*, Univ. Rochester. (2006) 1–3.
- [4] J.S.O. Evans, T.A. Mary, A.W. Sleight, Negative thermal expansion materials, *Phys. B Condens. Matter.* 241–243 (1998) 311–316. doi:10.1016/S0921-4526(97)00571-1.
- [5] W. Miller, C.W. Smith, D.S. MacKenzie, K.E. Evans, Negative thermal expansion: A review, *J. Mater. Sci.* 44 (2009) 5441–5451. doi:10.1007/s10853-009-3692-4.
- [6] R.M. Hazen, C.T. Prewitt, Effects of temperature and pressure on interatomic distances in oxygen-based minerals, *Am. Mineral.* 62 (1977) 309–315.
- [7] C.P. Romao, F.A. Perras, U. Werner-Zwanziger, J.A. Lussier, K.J. Miller, C.M. Calahoo, J.W. Zwanziger, M. Bieringer, B.A. Marinkovic, D.L. Bryce, M.A. White, Zero thermal expansion in  $ZrMgMo_3O_{12}$ : NMR crystallography reveals origins of thermoelastic properties, *Chem. Mater.* 27 (2015) 2633–2646. doi:10.1021/acs.chemmater.5b00429.
- [8] A.E.C. Cortés, A. Dosen, V.L. Blair, M.B. Johnson, M.A. White, B.A. Marinkovic, Phase transition and coefficients of thermal expansion in  $Al_{2-x}In_xW_3O_{12}$  ( $0.2 \leq x \leq 1$ ), *Materials.* 14 (2021). doi:10.3390/ma14144021.
- [9] S. Fu, Z. Sun, P. Huang, Y. Li, N. Hu, Some basic aspects of polymer nanocomposites: A critical review, *Nano Mater. Sci.* 1 (2019) 2–30. doi:10.1016/j.nanoms.2019.02.006.
- [10] L.P. Prisco, M. Marzano, P.I. Pontón, A.M.L.M. Costa, C.A. da Costa Neto, G. Sweet, C.P. Romao, M.A. White, B.A. Marinkovic, Relationship between sintering methods and physical properties of the low positive thermal

- expansion material  $\text{Al}_2\text{W}_3\text{O}_{12}$ , *Int. J. Appl. Ceram. Technol.* 16 (2019) 346–356. doi:10.1111/ijac.13054.
- [11] T. Hanemann, D.V. Szabó, *Polymer-nanoparticle composites: From synthesis to modern applications*, 2010. doi:10.3390/ma3063468.
- [12] D. Xu, K.M. Liechti, K. Ravi-Chandar, On the modified Tabor parameter for the JKR-DMT transition in the presence of a liquid meniscus, *J. Colloid Interface Sci.* 315 (2007) 772–785. doi:10.1016/j.jcis.2007.07.048.
- [13] A. Thill, O. Spalla, Aggregation due to capillary forces during drying of particle submonolayers, *Colloids Surfaces A Physicochem. Eng. Asp.* 217 (2003) 143–151. doi:10.1016/S0927-7757(02)00569-1.
- [14] Chapter 7 Measures of Rock-Fluid Interactions, (2000) 108–132.
- [15] L. Saunders, *Surface and Colloid Chemistry*, *J. Pharm. Pharmacol.* 3 (1951) 865–882. doi:10.1111/j.2042-7158.1951.tb13130.x.
- [16] S.J. Park, M.K. Seo, *Intermolecular Force*, 2011. doi:10.1016/B978-0-12-375049-5.00001-3.
- [17] D.J. Shaw, *Introduction to Colloid and Surface Chemistry*, 1992.
- [18] S. Fundamentals, *Encyclopedia of Tribology*, 2013. doi:10.1007/978-0-387-92897-5.
- [19] U. Nilsson, B. Jönsson, H. Wennerström, Hydration force, steric force or double-layer force between zwitterionic surfaces, *Faraday Discuss. Chem. Soc.* 90 (1990) 107–114. doi:10.1039/DC9909000107.
- [20] X. Zhang, D. Liu, Y. Sang, H. Liu, J. Wang, Effects of aging on the characteristics of Nd:YAG nano-powders, *J. Alloys Compd.* 502 (2010) 206–210. doi:10.1016/j.jallcom.2010.04.144.
- [21] S.V.N.T. Kuchibhatla, A.S. Karakoti, D.R. Baer, S. Samudrala, M.H. Engelhard, J.E. Amonette, S. Thevuthasan, S. Seal, Influence of aging and environment on nanoparticle chemistry: Implication to confinement effects in nanoceramics, *J. Phys. Chem. C.* 116 (2012) 14108–14114. doi:10.1021/jp300725s.
- [22] G.A. Parks, P.L. De Bruyn, The zero point of charge of oxides, *J. Phys. Chem.* 66 (1962) 967–973. doi:10.1021/j100812a002.
- [23] R.D. Kulkarni, P. Somasundaran, Mineralogical heterogeneity of ore particles and its effects on their interfacial characteristics, *Powder Technol.* 14 (1976) 279–285. doi:10.1016/0032-5910(76)80076-9.

- [24] L. Cromières, V. Moulin, B. Fourest, E. Giffaut, Physico-chemical characterization of the colloidal hematite/water interface: Experimentation and modelling, *Colloids Surfaces A Physicochem. Eng. Asp.* 202 (2002) 101–115. doi:10.1016/S0927-7757(01)01065-2.
- [25] D.N. Furlong, P.A. Freeman, A.C.M. Lau, The adsorption of soluble silica at solid-aqueous solution interfaces. I. Leaching from glass-an electrokinetic study, *J. Colloid Interface Sci.* 80 (1981) 20–31. doi:10.1016/0021-9797(81)90155-7.
- [26] K. Quast, Effects of solution ageing on the zeta potential characteristics of a hematite ore, *Adv. Powder Technol.* 26 (2015) 1219–1224. doi:10.1016/j.appt.2015.06.003.
- [27] M. Lok, Coprecipitation, *Synth. Solid Catal.* (2009) 135–151. doi:https://doi.org/10.1002/9783527626854.ch7.
- [28] H. Li, G. Wang, F. Zhang, Y. Cai, Y. Wang, I. Djerdj, Surfactant-assisted synthesis of CeO<sub>2</sub> nanoparticles and their application in wastewater treatment, *RSC Adv.* 2 (2012) 12413–12423. doi:10.1039/c2ra21590j.
- [29] L. Mancic, R.F.M. Osman, A.M.L.M. Costa, J.R.M. d’Almeida, B.A. Marinkovic, F.C. Rizzo, Thermal and mechanical properties of polyamide 11 based composites reinforced with surface modified titanate nanotubes, *Mater. Des.* 83 (2015) 459–467. doi:10.1016/j.matdes.2015.06.059.
- [30] I. Som, K. Bhatia, M. Yasir, Status of surfactants as penetration enhancers in transdermal drug delivery, *J. Pharm. Bioallied Sci.* 4 (2012) 2–9. doi:10.4103/0975-7406.92724.
- [31] Marzieh Jalilpour, Effect of aging time and calcination temperature on the cerium oxide nanoparticles synthesis via reverse co-precipitation method, *Int. J. Phys. Sci.* 7 (2012) 944–948. doi:10.5897/ijps11.131.
- [32] H.N. Azlina, J.N. Hasnidawani, H. Norita, S.N. Surip, Synthesis of SiO<sub>2</sub> nanostructures using sol-gel method, *Acta Phys. Pol. A.* 129 (2016) 842–844. doi:10.12693/APhysPolA.129.842.
- [33] M. Marzano, P.I. Pontón, B.A. Marinkovic, Co-precipitation of low-agglomerated Y<sub>2</sub>W<sub>3</sub>O<sub>12</sub> nanoparticles: The effects of aging time, calcination temperature and surfactant addition, *Ceram. Int.* 45 (2019) 20189–20196. doi:10.1016/j.ceramint.2019.06.288.
- [34] P.I. Pontón, L.P. Prisco, A. Dosen, G.S. Faro, M.A.S. de Abreu, B.A.

- Marinkovic, Co-precipitation synthesis of  $Y_2W_3O_{12}$  submicronic powder, *Ceram. Int.* 43 (2017) 4222–4228. doi:10.1016/j.ceramint.2016.12.055.
- [35] M.G.N. C. Barry Carter, *Ceramic Materials., Science and Engineering*, 2007.
- [36] U.P.M. Ashik, S. Kudo, J. Hayashi, *An Overview of Metal Oxide Nanostructures*, Elsevier Ltd., 2018. doi:10.1016/b978-0-08-101975-7.00002-6.
- [37] F. Schuth, M. Hesse, K.K. Unger, Preparation of solid catalysts. Bulk catalysts and supports, *Handb. Heterog. Catal.* (2008) 100–119. doi:https://doi.org/10.1002/9783527610044.hetcat0008.
- [38] M. Çelikkilek, A.E. Ersundu, S. Aydin, Crystallization kinetics of amorphous Material, in: *Adv. Cryst. Process.*, 2012: pp. 127–162. doi:10.1016/0040-6031(89)87294-6.
- [39] S. Arshadi, J. Moghaddam, M. Eskandarian, LaMer diagram approach to study the nucleation and growth of  $Cu_2O$  nanoparticles using supersaturation theory, *Korean J. Chem. Eng.* 31 (2014) 2020–2026. doi:10.1007/s11814-014-0130-3.
- [40] F. Schuth, M. Hesse, K.K. Unger, Precipitation and Coprecipitation, in: *Prep. Solid Catal.*, 2008: pp. 100–119.
- [41] T. Sugimoto, Preparation of monodispersed colloidal particles, *Av. Colloid Interface Sci.* 28 (1987) 65–108.
- [42] J.W.P. Schmelzer, G.S. Boltachev, V.G. Baidakov, Classical and generalized Gibbs' approaches and the work of critical cluster formation in nucleation theory, *J. Chem. Phys.* 124 (2006). doi:10.1063/1.2196412.
- [43] R.P. Rastogi, Thermodynamics of metastable equilibria (Metastability-Supersaturation, Nucleation and crystallization), *Proc. Indian Natl. Sci. Acad.* 75 (2009) 107–112.
- [44] I.M. Lifshitz, V. V. Slyozov, The kinetics of precipitation from supersaturated solid solutions, *J. Phys. Chem. Solids.* 19 (1961) 35–50. doi:10.1016/0022-3697(61)90054-3.
- [45] L. Ratke, P.W. Voorhees, *Growth and Coarsening: Ostwald Ripening in Material Processing*, 2002. doi:10.1080/08940886.2017.1316123.
- [46] G. Madras, B.J. McCoy, Transition from nucleation and growth to Ostwald ripening, *Chem. Eng. Sci.* 57 (2002) 3809–3818. doi:10.1016/S0009-2509(02)00313-5.

- [47] K. Sangwal, Ostwald Ripening, Crystal Size Distribution, and Polymorph Selection, *Nucleation Cryst. Growth.* (2018) 361–421. doi:10.1002/9781119461616.ch8.
- [48] T. Vetter, M. Iggländ, D.R. Ochsenein, F.S. Hänseler, M. Mazzotti, Modeling nucleation, growth, and ostwald ripening in crystallization processes: A comparison between population balance and kinetic rate equation, *Cryst. Growth Des.* 13 (2013) 4890–4905. doi:10.1021/cg4010714.
- [49] J. Gopalakrishnan, Chimie Douce Approaches to the Synthesis of Metastable Oxide Material, *Chem. Mater.* 7 (1995) 1265–1275. doi:10.1021/cm00055a001.
- [50] T. Werz, M. Baumann, U. Wolfram, C.E. Krill, Particle tracking during Ostwald ripening using time-resolved laboratory X-ray microtomography, *Mater. Charact.* 90 (2014) 185–195. doi:10.1016/j.matchar.2014.01.022.
- [51] J. Santos, N. Calero, L.A. Trujillo-Cayado, M.C. Garcia, J. Muñoz, Assessing differences between Ostwald ripening and coalescence by rheology, laser diffraction and multiple light scattering, *Colloids Surfaces B Biointerfaces.* 159 (2017) 405–411. doi:10.1016/j.colsurfb.2017.08.015.
- [52] J. Soma, K.D. Papadopoulos, Ostwald ripening in sodium dodecyl sulfate-stabilized decane-in-water emulsions, *J. Colloid Interface Sci.* 181 (1996) 225–231. doi:10.1006/jcis.1996.0374.
- [53] E. Gonzalez, N. Vejar, R. Solis, L. Muñoz, M. Victoria Encinas, M. Paez, Sol-Gel Films: Corrosion Protection Coating for Aluminium Alloy, *Sol-Gel Method - Des. Synth. New Mater. with Interes. Phys. Chem. Biol. Prop.* (2019). doi:10.5772/intechopen.79712.
- [54] C.J. Brinker, G.W. Scherer, *Sol-Gel Science: the physics and chemistry of sol-gel processing*, 1990. doi:10.1016/c2009-0-22386-5.
- [55] G.M. PAJONK, Drying Methods Preserving the Textural Properties of Gels, *Le J. Phys. Colloq.* 24 (1989) C4-13-C4-22. doi:10.1051/jphyscol:1989403.
- [56] A.M. Buckley, M. Greenblatt, The Sol-Gel Preparation of Silica Gels, *J. Chem. Educ.* 71 (1994) 599–602.
- [57] M. Jafarzadeh, I.A. Rahman, C.S. Sipaut, Synthesis of silica nanoparticles by modified sol-gel process: The effect of mixing modes of the reactants and drying techniques, *J. Sol-Gel Sci. Technol.* 50 (2009) 328–336.

- doi:10.1007/s10971-009-1958-6.
- [58] T. Matsoukas, E. Gulari, Monomer-addition growth with a slow initiation step: A growth model for silica particles from alkoxides, *J. Colloid Interface Sci.* 132 (1989) 13–21. doi:10.1016/0021-9797(89)90210-5.
- [59] K. Do Kim, H.T. Kim, Comparison of the effect of reaction parameters on particle size in the formation of SiO<sub>2</sub>, TiO<sub>2</sub>, and ZrO<sub>2</sub> nanoparticles, *Mater. Lett.* 57 (2003) 3211–3216. doi:10.1016/S0167-577X(03)00037-5.
- [60] M.A. Shadiya, N. Nandakumar, R. Joseph, K.E. George, On the facile polyvinyl alcohol assisted sol-gel synthesis of tetragonal zirconia nanopowder with mesoporous structure, *Adv. Powder Technol.* 28 (2017) 3148–3157. doi:10.1016/j.appt.2017.09.029.
- [61] M. Sivakumar, S. Kanagesan, R.S. Babu, S. Jesurani, R. Velmurugan, C. Thirupathi, T. Kalaiyani, Synthesis of CoFe<sub>2</sub>O<sub>4</sub> powder via PVA assisted sol-gel process, *J. Mater. Sci. Mater. Electron.* 23 (2012) 1045–1049. doi:10.1007/s10854-011-0545-0.
- [62] K. Siwińska-Stefańska, J. Zdarta, D. Paukszta, T. Jesionowski, The influence of addition of a catalyst and chelating agent on the properties of titanium dioxide synthesized via the sol–gel method, *J. Sol-Gel Sci. Technol.* 75 (2015) 264–278. doi:10.1007/s10971-015-3696-2.
- [63] C. Zhou, J. Ouyang, B. Yang, Retarded hydrolysis-condensing reactivity of tetrabutyl titanate by acetylacetone and the application in dye-sensitized solar cells, *Mater. Res. Bull.* 48 (2013) 4351–4356. doi:10.1016/j.materresbull.2013.07.016.
- [64] J.N. Hay, H.M. Raval, Synthesis of organic-inorganic hybrids via the non-hydrolytic sol-gel process, *Chem. Mater.* 13 (2001) 3396–3403. doi:10.1021/cm011024n.
- [65] A. Styskalik, D. Skoda, C.E. Barnes, J. Pinkas, The power of non-hydrolytic sol-gel chemistry: A review, *Catalysts.* 7 (2017). doi:10.3390/catal7060168.
- [66] Y. Wang, M. Bouchneb, R. Mighri, J.G. Alauzun, P.H. Mutin, Water Formation in Non-Hydrolytic Sol–Gel Routes: Selective Synthesis of Tetragonal and Monoclinic Mesoporous Zirconia as a Case Study, *Chem. - A Eur. J.* 27 (2021) 2670–2682. doi:10.1002/chem.202003081.
- [67] A. Vioux, Nonhydrolytic Sol-Gel Routes to Oxides, *Chem. Mater.* 9 (1997) 2292–2299. doi:10.1021/cm970322a.

- [68] V. Kestens, P. Conneely, A. Bernreuther, Vaporisation coulometric Karl Fischer titration: A perfect tool for water content determination of difficult matrix reference materials, *Food Chem.* 106 (2008) 1454–1459. doi:10.1016/j.foodchem.2007.01.079.
- [69] A.S. Meyer, C.M. Boyd, Determination of Water by Titration with Coulometrically Generated Karl Fischer Reagent, *Anal. Chem.* 31 (1959) 215–219. doi:10.1021/ac60146a018.
- [70] P.H. Mutin, A. Vioux, Non-Hydrolytic Sol–Gel Routes, *Ref. Modul. Mater. Sci. Mater. Eng.* (2016) 1–5. doi:10.1016/b978-0-12-803581-8.03751-6.
- [71] M. Andrianainarivelo, R.J.P. Corriu, D. Leclercq, P.H. Mutin, A. Vioux, Nonhydrolytic Sol-Gel Process: Aluminum Titanate Gels, *Chem. Mater.* 9 (1997) 1098–1102. doi:10.1021/cm960405b.
- [72] P. Arnal, R.J.P. Corriu, D. Leclercq, P.H. Mutin, A. Vioux, A Solution Chemistry Study of Nonhydrolytic Sol - Gel Routes to Titania, *Chem. Mater.* 9 (1997) 694–698. doi:10.1021/cm960337t.
- [73] M. Andrianainarivelo, R.J.P. Corriu, D. Leclercq, P. Hubert Mutin, A. Vioux, Non-hydrolytic sol-gel process: Zirconium titanate gels, *J. Mater. Chem.* 7 (1997) 279–284. doi:10.1039/a605168e.
- [74] L. Young, P.T. Alvarez, H. Liu, C. Lind, Extremely Low Temperature Crystallization in the  $A_2M_3O_{12}$  Family of Negative Thermal Expansion Materials, *Eur. J. Inorg. Chem.* 2016 (2016) 1251–1256. doi:10.1002/ejic.201501420.
- [75] R. Truitt, I. Hermes, A. Main, A. Sendekci, C. Lind, Low temperature synthesis and characterization of  $AlScMo_3O_{12}$ , *Materials.* 8 (2015) 700–716. doi:10.3390/ma8020700.
- [76] S.D. Gates, C. Lind, Polymorphism in yttrium molybdate  $Y_2Mo_3O_{12}$ , *J. Solid State Chem.* 180 (2007) 3510–3514. doi:10.1016/j.jssc.2007.10.011.
- [77] S.D. Gates, J.A. Colin, C. Lind, Non-hydrolytic sol-gel synthesis, properties, and high-pressure behavior of gallium molybdate, *J. Mater. Chem.* 16 (2006) 4214–4219. doi:10.1039/b608864c.
- [78] V. Lafond, P.H. Mutin, A. Vioux, Control of the texture of titania-silica mixed oxides prepared by nonhydrolytic sol-gel, *Chem. Mater.* 16 (2004) 5380–5386. doi:10.1021/cm0490569.
- [79] L.P. Prisco, P.I. Pontón, M. V. Guamán, R.R. Aviliez, C.P. Romao, M.B.

- Johnson, M.A. White, B.A. Marinkovic, Assessment of the Thermal Shock Resistance Figures of Merit of  $\text{Al}_2\text{W}_3\text{O}_{12}$ , a Low Thermal Expansion Ceramic, *J. Am. Ceram. Soc.* 99 (2016) 1742–1748. doi:10.1111/jace.14160.
- [80] D.A. Woodcock, P. Lightfoot, C. Ritter, Negative thermal expansion in  $\text{Y}_2(\text{WO}_4)_3$ , *J. Solid State Chem.* 149 (2000) 92–98. doi:10.1006/jssc.1999.8502.
- [81] N. Imanaka, M. Hiraiwa, G. Adachi, H. Dabkowska, A. Dabkowski, Thermal contraction behavior in  $\text{Al}_2(\text{WO}_4)_3$  single crystal, *J. Cryst. Growth.* 220 (2000) 176–179. doi:10.1016/S0022-0248(00)00771-5.
- [82] P.I. Pontón, L.P. Prisco, B.A. Marinkovic, Effects of low contents of  $\text{A}_2\text{M}_3\text{O}_{12}$  submicronic thermomiotic-like fillers on thermal expansion and mechanical properties of HDPE-based composites, *Polym. Compos.* 39 (2018) E1821–E1833. doi:10.1002/pc.24811.
- [83] S.N. Ellis, C.P. Romao, M.A. White, Near-zero thermal expansion in freeze-cast composite materials, *Ceramics.* 2 (2019) 112–125. doi:10.3390/ceramics2010011.
- [84] C.P. Romao, B.A. Marinkovic, U. Werner-Zwanziger, M.A. White, Thermal Expansion Reduction in Alumina-Toughened Zirconia by Incorporation of Zirconium Tungstate and Aluminum Tungstate, *J. Am. Ceram. Soc.* 98 (2015) 2858–2865. doi:10.1111/jace.13675.
- [85] P.M. Jardim, E.S. Garcia, B.A. Marinkovic, Young's modulus, hardness and thermal expansion of sintered  $\text{Al}_2\text{W}_3\text{O}_{12}$  with different porosity fractions, *Ceram. Int.* 42 (2016) 5211–5217. doi:10.1016/j.ceramint.2015.12.045.
- [86] T. Varga, A.P. Wilkinson, C. Lind, W.A. Bassett, C.S. Zha, High pressure synchrotron x-ray powder diffraction study of  $\text{Sc}_2\text{Mo}_3\text{O}_{12}$  and  $\text{Al}_2\text{W}_3\text{O}_{12}$ , *J. Phys. Condens. Matter.* 17 (2005) 4271–4283. doi:10.1088/0953-8984/17/27/004.
- [87] S. Karmakar, S.K. Deb, A.K. Tyagi, S.M. Sharma, Pressure-induced amorphization in  $\text{Y}_2(\text{WO}_4)_3$ : In situ X-ray diffraction and Raman studies, *J. Solid State Chem.* 177 (2004) 4087–4092. doi:10.1016/j.jssc.2004.08.020.
- [88] N.J.-. Fang, T. -W Chou, Characterization of Interlaminar Shear Strength of Ceramic Matrix Composites, *J. Am. Ceram. Soc.* 76 (1993) 2539–2548. doi:10.1111/j.1151-2916.1993.tb03979.x.
- [89] T.I. Baiz, Non-hydrolytic sol-gel synthesis and characterization of materials

- of the type  $AA'M_3O_{12}$ , 2010.
- [90] C. Sanchez, L. Rozes, F. Ribot, C. Laberty-Robert, D. Grosso, C. Sasso, C. Boissiere, L. Nicole, “Chimie douce”: A land of opportunities for the designed construction of functional inorganic and hybrid organic-inorganic nanomaterials, *Comptes Rendus Chim.* 13 (2010) 3–39. doi:10.1016/j.crci.2009.06.001.
- [91] D. Nihtianova, N. Velichkova, R. Nikolova, I. Koseva, A. Yordanova, V. Nikolov, Characterization of nanosized  $Al_2(WO_4)_3$ , *Mater. Res. Bull.* 46 (2011) 2125–2130. doi:10.1016/j.materresbull.2011.06.038.
- [92] V. Nikolov, I. Koseva, R. Stoyanova, E. Zhecheva, Conditions for preparation of nanosized  $Al_2(WO_4)_3$ , *J. Alloys Compd.* 505 (2010) 443–449. doi:10.1016/j.jallcom.2010.06.100.
- [93] B.A. Marinkovic, P.I. Pontón, C.P. Romao, T. Moreira, M.A. White, Negative and Near-Zero Thermal Expansion in  $A_2M_3O_{12}$  and Related Ceramic Families: A Review, *Front. Mater.* 8 (2021). doi:10.3389/fmats.2021.741560.
- [94] C. Marlot, E. Barraud, S. Le Gallet, M. Eichhorn, F. Bernard, Synthesis of YAG nanopowder by the co-precipitation method: Influence of pH and study of the reaction mechanisms, *J. Solid State Chem.* 191 (2012) 114–120. doi:10.1016/j.jssc.2012.02.063.
- [95] W. Li, M. Zhang, J. Zhang, Y. Han, Self-assembly of cetyltrimethylammonium bromide in ethanol-water mixtures, *Front. Chem. China.* 1 (2006) 438–442. doi:10.1007/s11458-006-0069-y.
- [96] J. Mata, D. Varade, P. Bahadur, Aggregation behavior of quaternary salt based cationic surfactants, *Thermochim. Acta.* 428 (2005) 147–155. doi:10.1016/j.tca.2004.11.009.
- [97] P. Bhattarai, T.P. Niraula, A. Bhattarai, Thermodynamic properties of cetyltrimethylammonium bromide in ethanol-water media with/without the presence of the divalent salt, *J. Oleo Sci.* 70 (2021) 363–374. doi:10.5650/jos.ess20207.
- [98] M. Dalpasquale, Comportamento térmico (TG-DTA) de sais de alumínio e análise morfológica (MEV) e estrutural (DRX) do resíduo final, (2017).
- [99] J.C.R. de A. Andrade, A.R. Loiola, L.R.D. da Silva, R.E. Romero, Assessment of release of  $NH_4NO_3$  occluded zeolite 4A in solutions from

- salinas, *Quim. Nova.* 33 (2010) 1692–1697. doi:10.1590/s0100-40422010000800014.
- [100] M. Pudukudy, Z. Yaakob, R. Rajendran, T. Kandaramath, Photodegradation of methylene blue over novel 3D ZnO microflowers with hexagonal pyramid-like petals, *React. Kinet. Mech. Catal.* 112 (2014) 527–542. doi:10.1007/s11144-014-0703-5.
- [101] H.P. Poole, T. Grande, F. Sciortino, H. Stanley, C.A. Angell, Amorphous polymorphs, *Comput. Mater. Sci.* (1995) 373–382. doi:10.1063/1.4709880.
- [102] M. Durandurdu, Polyamorphism in Aluminum Nitride: A First Principles Molecular Dynamics Study, *J. Am. Ceram. Soc.* 99 (2016) 1594–1600. doi:10.1111/jace.14186.
- [103] W. Sha, X. Wu, K.G. Keong, Modelling the thermodynamics and kinetics of crystallisation of nickel–phosphorus (Ni–P) deposits, *Electroless Copping Nickel–Phosphorus Plat.* (2011) 183–217. doi:10.1533/9780857090966.2.183.
- [104] J. Málek, T. Mitsuhashi, Testing method for the Johnson-Mehl-Avrami equation in kinetic analysis of crystallization processes, *J. Am. Ceram. Soc.* 83 (2000) 2103–2105. doi:10.1111/j.1151-2916.2000.tb01523.x.
- [105] J. Málek, The applicability of Johnson-Mehl-Avrami model in the thermal analysis of the crystallization kinetics of glasses, *Thermochim. Acta.* 267 (1995) 61–73. doi:10.1016/0040-6031(95)02466-2.
- [106] C.A. Kelly, M.J. Jenkins, Modeling the crystallization kinetics of polymers displaying high levels of secondary crystallization, *Polym. J.* 54 (2022) 249–257. doi:10.1038/s41428-021-00581-0.
- [107] D.W. Van Krevelen, K. Te Nijenhuis, Properties Determining Mass Transfer In Polymeric Systems, 2009. doi:10.1016/b978-0-08-054819-7.00018-2.
- [108] M. Ghasemzadeh, A. Nemat, A. Nozad, Z. Hamnabard, S. Baghshah, Crystallization kinetics of glass-ceramics by differential thermal analysis, *Ceram. - Silikaty.* 55 (2011) 188–194.
- [109] J. Shi, F. He, J. Xie, X. Liu, H. Yang, Kinetic analysis of crystallization in  $\text{Li}_2\text{O}-\text{Al}_2\text{O}_3-\text{SiO}_2-\text{B}_2\text{O}_3-\text{BaO}$  glass-ceramics, *J. Non. Cryst. Solids.* 491 (2018) 106–113. doi:10.1016/j.jnoncrysol.2018.04.004.
- [110] R.R. Pelá, L.S. Cividanes, D.D. Brunelli, S.M. Zanetti, G.P. Thim, Kinetic study of  $\alpha$ -BZN crystallization obtained from chemical method, *Mater. Res.*

- 11 (2008) 289–293. doi:10.1590/S1516-14392008000300010.
- [111] C.-C. Chen, F.-S. Yen, C.-Y. Huang, Aging Effects on the Characteristics and Sintering Behavior of Coprecipitated Al<sub>2</sub>O<sub>3</sub>-ZrO<sub>2</sub> Powders, *Ceram. Int.* 20 (1994) 379–384. doi:10.1109/ISIE.2017.8001273.
- [112] L. Luo, K. Li, P. Du, Y. Wang, Aging effect in Er<sup>3+</sup>-doped 0.5Ba(Zr<sub>0.2</sub>Ti<sub>0.8</sub>)O<sub>3</sub>-0.5(Ba<sub>0.7</sub>Ca<sub>0.3</sub>)TiO<sub>3</sub> ceramics, *J. Am. Ceram. Soc.* 103 (2020) 773–778. doi:10.1111/jace.16887.
- [113] F. Can, X. Courtois, D. Duprez, Tungsten-based catalysts for environmental applications, *Catalysts*. 11 (2021). doi:10.3390/catal11060703.
- [114] D. Ivanova, V. Nikolov, P. Peshev, Solvents for growing Al<sub>2</sub>(WO<sub>4</sub>)<sub>3</sub> single crystals from high-temperature solutions, *J. Alloys Compd.* 430 (2007) 356–360. doi:10.1016/j.jallcom.2006.05.028.
- [115] N.T.K. Thanh, N. Maclean, S. Mahiddine, Mechanisms of nucleation and growth of nanoparticles in solution, *Chem. Rev.* 114 (2014) 7610–7630. doi:10.1021/cr400544s.
- [116] M. Haruta, B. Delmon, Preparation of homodisperse solids, *J. Chim. Phys.* 83 (1986) 859–868. doi:10.1051/jcp/1986830859.
- [117] A.R. Pascoe, Q. Gu, M.U. Rothmann, W. Li, Y. Zhang, A.D. Scully, X. Lin, L. Spiccia, U. Bach, Y.B. Cheng, Directing nucleation and growth kinetics in solution-processed hybrid perovskite thin-films, *Sci. China Mater.* 60 (2017) 617–628. doi:10.1007/s40843-017-9043-y.
- [118] D.A. Porter, K.E. Easterling, M.Y. Sherif, Phase transformations in metals and alloys, third edition, 2009.
- [119] G. Wang, Y. Zhou, D.G. Evans, Y. Lin, Preparation of highly dispersed nano-La<sub>2</sub>O<sub>3</sub> particles using modified carbon black as an agglomeration inhibitor, *Ind. Eng. Chem. Res.* 51 (2012) 14692–14699. doi:10.1021/ie300999u.
- [120] M.R. Shedam, A.V. Rao, Growth of Single Crystals of Cadmium Oxalate in Silica Gels, *Cryst. Res. Technol.* 28 (1993) K5–K7. doi:10.1002/crat.2170280125.
- [121] Pranwadee Kaewmuang, T. Thongtem, S. Thongtem, S. Kittiwachana, S. Kaowphong, Influence of Calcination Temperature on Particle Size and Photocatalytic Activity of Nanosized NiO Powder, *Russ. J. Phys. Chem. A.* 92 (2018) 1777–1781. doi:10.1134/S003602441809011X.

- [122] S. Satapathy, A. Ahlawat, A. Paliwal, R. Singh, M.K. Singh, P.K. Gupta, Effect of calcination temperature on nanoparticle morphology and its consequence on optical properties of Nd:Y<sub>2</sub>O<sub>3</sub> transparent ceramics, *CrystEngComm*. 16 (2014) 2723–2731. doi:10.1039/c3ce42529k.
- [123] S. Ghosh, D. Divya, K.C. Remani, T.S. Sreeremya, Growth of monodisperse nanocrystals of cerium oxide during synthesis and annealing, *J. Nanoparticle Res.* 12 (2010) 1905–1911. doi:10.1007/s11051-009-9753-4.
- [124] Syed Ali Ashter, Thermoforming of Single and Multilayer Laminates, in: *Thermoforming of Single and Multilayer Laminates*, 2014: pp. 123–145. doi:10.1201/b19009-9.
- [125] R.H. Borgwardt, Calcination kinetics and surface area of dispersed limestone particles, *AIChE J.* 31 (1985) 103–111. doi:10.1002/aic.690310112.
- [126] J. Gadiant, V. Livingstone, D. Klink, C.R. Grice, C. Lind, Low temperature synthesis of nanocrystalline V<sub>2</sub>O<sub>5</sub> using the non-hydrolytic sol–gel method, *J. Sol-Gel Sci. Technol.* 89 (2019) 663–671. doi:10.1007/s10971-019-04926-3.
- [127] C. Lind, S.D. Gates, N.M. Pedoussaut, T.I. Baiz, Novel materials through non-hydrolytic sol-gel processing: Negative thermal expansion oxides and beyond, *Materials*. 3 (2010) 2567–2587. doi:10.3390/ma3042567.
- [128] V. Smeets, A. Styskalik, D.P. Debecker, Non-hydrolytic sol–gel as a versatile route for the preparation of hybrid heterogeneous catalysts, *J. Sol-Gel Sci. Technol.* 97 (2021) 505–522. doi:10.1007/s10971-021-05486-1.
- [129] P.I. Pontón, K. Yamada, M. V. Guamán, M.B. Johnson, M.A. White, O. Pandoli, A.M.L.M. Costa, B.A. Marinkovic, The effect of titanate nanotube/Y<sub>2</sub>W<sub>3</sub>O<sub>12</sub> hybrid fillers on mechanical and thermal properties of HDPE-based composites, *Mater. Today Commun.* 18 (2019) 124–135. doi:10.1016/j.mtcomm.2018.11.014.
- [130] C. Lind, Two Decades of Negative Thermal Expansion Research: Where do we stand?, *Materials*. 5 (2012) 1125–1154. doi:10.3390/ma5061125.
- [131] T.I. Baiz, A.M. Gindhart, S.K. Kraemer, C. Lind, Synthesis of MgHf(WO<sub>4</sub>)<sub>3</sub> and MgZr(WO<sub>4</sub>)<sub>3</sub> using a non-hydrolytic sol-gel method, *J. Sol-Gel Sci. Technol.* 47 (2008) 128–130. doi:10.1007/s10971-008-1765-5.
- [132] A. Vioux, P.H. Mutin, *Handbook of Sol-Gel Science and Technology*, in: *Sol-Gel Process.*, Kluwer Academic Publishers, 2004: p. 621.

- [133] D.H. Napper, Steric stabilization, *J. Colloid Interface Sci.* 58 (1977) 390–407. doi:10.1016/0021-9797(77)90150-3.
- [134] N. Murshid, X. Wang, Hydrophobic Effect of Alkyl Groups Stabilizing Self-Assembled Colloids in Water, *J. Phys. Chem. B.* 121 (2017) 6280–6285. doi:10.1021/acs.jpcc.7b04353.
- [135] A. Vioux, P. Hubert Mutin, Nonhydrolytic Sol-Gel Technology, in: *Handb. Sol-Gel Sci. Technol.*, Springer International Publishing, Cham, 2018: pp. 1039–1065. doi:10.1007/978-3-319-32101-1\_28.
- [136] P.I. Pontón, K. Yamada, M. V. Guamán, M.B. Johnson, M.A. White, B.A. Marinkovic, Data supporting micromechanical models for the estimation of Young's modulus and coefficient of thermal expansion of titanate nanotube/ $Y_2W_3O_{12}$ /HDPE ternary composites, *Data Br.* 25 (2019). doi:10.1016/j.dib.2019.104247.
- [137] A. Salehabadi, Rare-earth-based tungstates ceramic nanomaterials: Recent advancements and technologies, in: *Adv. Rare Earth-Based Ceram. Nanomater.*, 2022. doi:10.1016/B978-0-323-89957-4.00003-7.
- [138] L.P. Prisco, P.I. Pontón, W. Paraguassu, C.P. Romao, M.A. White, B.A. Marinkovic, Near-zero thermal expansion and phase transition in  $In_{0.5}(ZrMg)_{0.75}Mo_3O_{12}$ , *J. Mater. Res.* 31 (2016) 3240–3248. doi:10.1557/jmr.2016.329.
- [139] M.Y. Wu, Y. Jia, Q. Sun, Effects of  $A^{3+}$  cations on hydration in  $A_2M_3O_{12}$  family materials: A first-principles study, *Comput. Mater. Sci.* 111 (2016) 28–33. doi:10.1016/j.commatsci.2015.09.010.
- [140] B.A. Marinkovic, T.M. Machado, R.R. de Avillez, A. Madrid, P.H. de Melo Toledo, G.F.S. Andrade, Zero thermal expansion in  $ZrMg_{1-x}Zn_xMo_3O_{12}$ , *Ceram. Int.* 47 (2021) 26567–26571. doi:10.1016/j.ceramint.2021.05.280.
- [141] A. Madrid, P.I. Pontón, F. Garcia, M.B. Johnson, M.A. White, B.A. Marinkovic, Solubility limit of  $Zn^{2+}$  in low thermal expansion  $ZrMgMo_3O_{12}$  and its influence on phase transition temperature, *Ceram. Int.* 46 (2020) 3979–3983. doi:10.1016/j.ceramint.2019.09.252.
- [142] E.S. Dedova, V.S. Shadrin, M.Y. Petrushina, S.N. Kulkov, The Study on Thermal Expansion of Ceramic Composites with Addition of  $ZrW_2O_8$ , *IOP Conf. Ser. Mater. Sci. Eng.* 116 (2016) 6–11. doi:10.1088/1757-899X/116/1/012030.

- [143] M. Yang, S. Wei, S. lei Su, M. Chao, J. Guo, H. Wang, X. Tang, Y. Jiao, E. Liang, The influence of  $\text{ZrMgMo}_3\text{O}_{12}$  on the dielectric properties of  $\text{BaTi}_4\text{O}_9$ , *Ceram. Int.* 46 (2020) 10250–10255. doi:10.1016/j.ceramint.2020.01.017.
- [144] J. Yang, Z. Liu, Y. Shi, M. Li, M. Yang, E. Liang, Investigation on the synthesis and the mechanical and thermal expansion properties of  $\text{ZrMgMo}_3\text{O}_{12}$  ceramic bodies, *Ceram. Int.* 45 (2019) 8750–8760. doi:10.1016/j.ceramint.2019.01.199.
- [145] V.C. Sanjay J. Dhoble, Vijay B. Pawade, Hendrik C. Swart, ed., *Spectroscopy of Lanthanide Doped Oxide Materials*, Woodhead P, Elsevier Science & Technology, 2020.
- [146] Y. Ben Smida, R. Marzouki, S. Kaya, S. Erkan, M. Faouzi Zid, A. Hichem Hamzaoui, *Synthesis Methods in Solid-State Chemistry*, *Synth. Methods Cryst.* (2020). doi:10.5772/intechopen.93337.
- [147] Y. Ma, M. Svärd, X. Xiao, J.M. Gardner, R.T. Olsson, K. Forsberg, Precipitation and crystallization used in the production of metal salts for lithium battery materials: A review, *Metals.* 10 (2020) 1–16. doi:10.3390/met10121609.
- [148] I. Pritula, K. Sangwal, *Fundamentals of Crystal Growth from Solutions*, Second Edi, Elsevier B.V., 2015. doi:10.1016/B978-0-444-63303-3.00029-8.
- [149] K. Sangwal, *Growth from Solutions*, *Encycl. Mater. Sci. Technol.* (2001) 3671–3680. doi:10.1016/b0-08-043152-6/00655-0.
- [150] S. Gates-Rector, T. Blanton, *The Powder Diffraction File: a quality materials characterization database*, *Powder Diffr.* 34 (2019) 352–360. doi:10.1017/S0885715619000812.
- [151] T.N. Kovács, D. Hunyadi, A.L.A. de Lucena, I.M. Szilágyi, Thermal decomposition of ammonium molybdates, *J. Therm. Anal. Calorim.* 124 (2016) 1013–1021. doi:10.1007/s10973-015-5201-0.
- [152] S. Bristow, T. Shekunov, B.Y. Shekunov, P. York, Analysis of the supersaturation and precipitation process with supercritical  $\text{CO}_2$ , *J. Supercrit. Fluids.* 21 (2001) 257–271. doi:10.1016/S0896-8446(01)00100-0.
- [153] T. Kobayashi, T. Sasaki, I. Takagi, H. Moriyama, Solubility of zirconium(IV) hydrous oxides, *J. Nucl. Sci. Technol.* 44 (2007) 90–94.

- doi:10.1080/18811248.2007.9711260.
- [154] J.H. Huang, C. Kargl-Simard, M. Oliazadeh, A.M. Alfantazi, pH-controlled precipitation of cobalt and molybdenum from industrial waste effluents of a cobalt electrodeposition process, *Hydrometallurgy*. 75 (2004) 77–90. doi:10.1016/j.hydromet.2004.06.008.
- [155] A.R. Lansdown, Molybdenum Disulphide Lubrication, in: A.R. Lansdown (Ed.), *Tribol. Ser.*, Elsevier, 1999: pp. 21–30. doi:https://doi.org/10.1016/S0167-8922(99)80006-6.
- [156] V. Yatirajam, U. Ahuja, L.R. Kakkar, Precipitation of molybdenum(V) as the hydroxide and its separation from rhenium, *Talanta*. 22 (1975) 315–317. doi:10.1016/0039-9140(75)80071-3.
- [157] A.N. Startsev, O. V. Klimov, S.A. Shkuropat, M.A. Fedotov, S.P. Degtyarev, D.I. Kochubey, Synthesis properties and structure of binuclear anionic “Mo(V) hydroxide”,  $[\text{Mo}_2\text{O}_4(\text{OH})_4(\text{H}_2\text{O}_2)]^{2-}$ , *Polyhedron*. 13 (1994) 505–512. doi:10.1016/S0277-5387(00)81667-8.
- [158] A.Z. Mesquita, *Nuclear Reactors*, Edited by Amir Zacarias Mesquita, IntechOpen, 2012. doi:10.5772/1919.
- [159] C. Yamagata, J.O.A. Paschoal, Systematic precipitation of magnesium hydroxide using  $\text{NH}_4\text{OH}$  to preparing MgO-PSZ precursor powder, *Mater. Sci. Forum*. 805 (2015) 712–717. doi:10.4028/www.scientific.net/MSF.805.712.
- [160] L.F. Amaral, R. Salomão, E. Frollini, V.C. Pandolfelli, Mechanisms of magnesium oxide hydration, *Ceramica*. 53 (2007) 368–372. doi:10.1590/s0366-69132007000400006.

**9.****Appendix****Appendix A: Supplementary material to support Chapter 4****A.1.****Methods applied to synthesize  $\text{Al}_2\text{W}_3\text{O}_{12}$** 

Four different co-precipitation routes have been applied with the purpose to synthesize  $\text{Al}_2\text{W}_3\text{O}_{12}$  submicronic powders, including i) Method A, ii) Method A35, iii) Method CTAB (in which the three methodologies were described in chapter 4), and iv) co-precipitation route by mixing reactants at room temperature followed by hydrothermal treatment at 180 °C (not discussed in chapter 4).

**A.1.1. Synthesis of  $\text{Al}_2\text{W}_3\text{O}_{12}$  powders through co-precipitation route by mixing reactants at room temperature followed by hydrothermal treatment at 180 °C (Method B)**

The co-precipitation synthesis was conducted by mixing 0.1 M aqueous solutions of  $\text{Al}(\text{NO}_3)_3 \cdot 9\text{H}_2\text{O}$  (Isofar, 99%) and  $(\text{NH}_4)_6\text{W}_{12}\text{O}_{39} \cdot x\text{H}_2\text{O}$  (Anhy, Alfa Aesar) or  $\text{Na}_2\text{WO}_4 \cdot 2\text{H}_2\text{O}$  (Sigma Aldrich, 99%) simultaneously, into an empty Becker. The final pH was around 4.0 and no adjustment was necessary. The dispersion was mixed with distilled water to complete 300 ml and the pH has been adjusted to 4 using nitric acid (Isofar, 65%, P.A.) in a molar ratio of 1:3. Then, the dispersion was introduced in an autoclave (High Pressure, Reator BR-300, Berghof) for hydrothermal treatment at 180 °C during 24 h with or without stirring. After hydrothermal treatment at 180 °C the content of the autoclave was cooled to room temperature. Subsequently, the final product was collected and washed three times with anhydrous ethanol (Vetec, 99.9%). The wet powder was dried using a conventional domestic microwave until complete drying (3 min). No further heat treatments were performed and the sample was analyzed to verify if the hydrothermal treatment (HT) was sufficient to promote the crystallization of the powder. Then, after XRPD analysis, part of the same dried powder was calcined using a tubular furnace (model FT-1200/H-1 Z furnace; São Carlos, Brazil) after achieving the desired temperature and kept there for 20min. After

that, the samples were removed and quenched to room temperature in air. This process was applied to observe if the hydrothermal treatment could be favorable in decreasing the crystallization temperature of the powder.

### A.1.2.

#### Result and discussion

Method B does not present TGA/DSC curves because the powder after the hydrothermal treatment was expected to be crystallized, therefore, in theory, would not need a subsequent calcination step.

The following attempts were performed:

- a) Synthesis was performed using sodium tungstate and the hydrothermal treatment at 180 °C during 24 h **under stirring**.
- b) Synthesis was performed using sodium tungstate and the hydrothermal treatment at 180 °C during 24 h **without stirring**.
- c) Synthesis was performed using **ammonium tungstate** and the hydrothermal treatment at 180 °C during 24 h **under stirring**.

Since those powders did not crystallize after these different attempts (from *a* - *c*), samples *a* and *b* (listed above) were calcined at 575 °C to verify if the hydrothermal treatment could, at least, present some effect on decreasing the calcination temperature. Thus, the following further attempts were performed:

- d) Part of the dried powder of sample *a* has been inserted in a tubular furnace at 575 °C for 20 min and cooled at room temperature.
- e) Part of the dried powder of sample *b* has been inserted in a tubular furnace at 575 °C for 20 min and cooled at room temperature.

However, the powders did not crystallize after both calcinations, therefore, no further analysis has been performed.

### A.1.3.

#### Conclusions

$\text{Al}_2\text{W}_3\text{O}_{12}$  did not crystallize by hydrothermal treatment even after calcination temperature was applied at 575 °C for 20 min.

Some improvements, such as increasing the time of the hydrothermal treatment or even changing the initial steps during synthesis, i.e., instead of mixing

the reagents the synthesis can be carried by dripping reactants that could be favorable to the crystallization step without the need of calcination step. It would be also interesting to explore complexing agents addition along with the reduction of the synthesis time or rising the pH and pressure.

## Appendix B: Supplementary material to support Chapter 6

### B.1.

#### Methods applied to synthesize $\text{ZrMgMo}_3\text{O}_{12}$

Three different co-precipitation routes have been applied with the purpose to synthesize  $\text{ZrMgMo}_3\text{O}_{12}$  submicronic powders, which include i) co-precipitation by mixing reactants, ii) co-precipitation by dripping reactants at pH=9, and iii) co-precipitation followed by total evaporation (described in chapter 6).

##### B.1.1. Co-precipitation by mixing reactants

The co-precipitation of the  $\text{ZrMgMo}_3\text{O}_{12}$  was conducted by simultaneous spilling 0.1 M aqueous solutions of  $\text{Zr}(\text{NO}_3)_4 \cdot 5\text{H}_2\text{O}$  (Isofar, 99%) and  $\text{Mg}(\text{NO}_3)_2 \cdot 6\text{H}_2\text{O}$  (Vetec, 99%) into  $(\text{NH}_4)_6\text{Mo}_7\text{O}_{24} \cdot 4\text{H}_2\text{O}$  (Isofar, 99%). A milky dispersion amorphous precipitate was immediately formed. The precipitate was recovered by centrifugation and washed three times with anhydrous ethanol (Vetec, 99.9%). The co-precipitate was dried using a microwave drying (MW) using a conventional domestic microwave oven during 3 min. The sample was introduced in a tubular furnace (Maitec-INTI FET 1600/H furnace; São Carlos, Brazil) after the desired temperature have been achieved (based on thermogravimetric analysis (TGA) and differential scanning calorimetry (DSC) results), kept there during 20 min and removed to quench at room temperature in air. A scheme of co-precipitation synthesis is shown in Figure 40, and the final amorphous precursor powder was denoted as  $\text{pmixS}_n$ , while calcined samples were denoted as  $\text{S}_n$ , where  $n = 1, 2, 3, 4,$  and  $5$ .

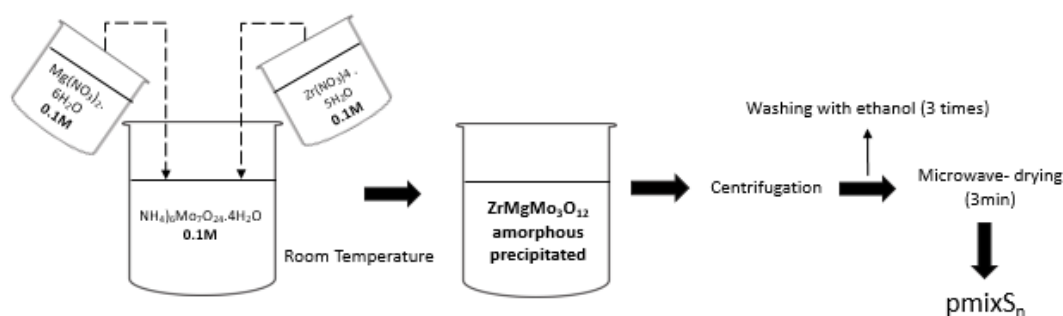


Figure 40: Co-precipitation by mixing reactants as an attempt to prepare a  $\text{ZrMgMo}_3\text{O}_{12}$  precursor.

Different attempts were made to reach the desired phase. Table 11 shows the different synthesis conditions applied, changing the pH of the reactant solutions.

Table 11: pH synthesis conditions applied to reach  $\text{ZrMgMo}_3\text{O}_{12}$  by mixing reactants

	Compound	Without	pH	pH	pH	pH
		adjustment of pH	adjustment *A	adjustment *B	adjustment *B	adjustment *B
1	$\text{Zr}(\text{NO}_3)_4 \cdot 5\text{H}_2\text{O}$	1.2	1.8 <sup>*A</sup>	1.1	3.5 <sup>**B</sup>	13.5 <sup>**B</sup>
2	$\text{Mg}(\text{NO}_3)_2 \cdot 6\text{H}_2\text{O}$	5.2	10.0 <sup>*A</sup>	9.0 <sup>**B</sup>	10.1 <sup>**B</sup>	5.1
3	$(\text{NH}_4)_6\text{Mo}_7\text{O}_{24} \cdot 4\text{H}_2\text{O}$	5.7	6.0 <sup>*A</sup>	9.0 <sup>**B</sup>	10.0 <sup>**B</sup>	5.5
	Final pH	1.6	2.8	7.0	9.6	13.2
	Amorphous Sample	pmixS <sub>1</sub>	pmixS <sub>2</sub>	pmixS <sub>3</sub>	pmixS <sub>4</sub>	pmixS <sub>5</sub>

\*The pH of reactant solution was adjusted using 0.1 M or 1 M NaOH, denoted (A) or (B), respectively.

### B.1.2.

#### Co-precipitation by dripping reactants and pH control

Co-precipitation was carried out by spilling of 0.1 M aqueous solution of  $\text{Mg}(\text{NO}_3)_2 \cdot 6\text{H}_2\text{O}$  (Vetec, 99%) into  $(\text{NH}_4)_6\text{Mo}_7\text{O}_{24} \cdot 4\text{H}_2\text{O}$  (Isofar, 99%). The pH of this suspension was adjusted until 8.5 using 1 M of NaOH. Afterwards,  $\text{Zr}(\text{NO}_3)_4 \cdot 5\text{H}_2\text{O}$  (Isofar, 99%) was dripped into the initial suspension, under stirring at 600 rpm (Fisam, model 752a) at room temperature. The dripping of  $\text{Zr}(\text{NO}_3)_4 \cdot 5\text{H}_2\text{O}$  was conducted in a controlled manner ( $2 \text{ mL min}^{-1}$ ) and in order to keep the pH of the reaction medium constant (pH ~9) 1 M of NaOH was also simultaneously dripped.

The co-precipitate was recovered by centrifugation and washed three times with anhydrous ethanol (Vetec, 99.9%). Then, it was dried in a conventional domestic microwave oven during 3 min. The sample was calcined using the same equipment as described in A.1.1., however, the sample was inserted at  $800^\circ\text{C}$ , kept there during 5 h, removed, and quenched to room temperature in air. The calcination was done only at the temperature and time described above. The scheme of co-precipitation synthesis is shown in Figure 41, and the final amorphous precursor powder was denoted as pGC, while the calcined powder was called GC<sub>800°C</sub>.

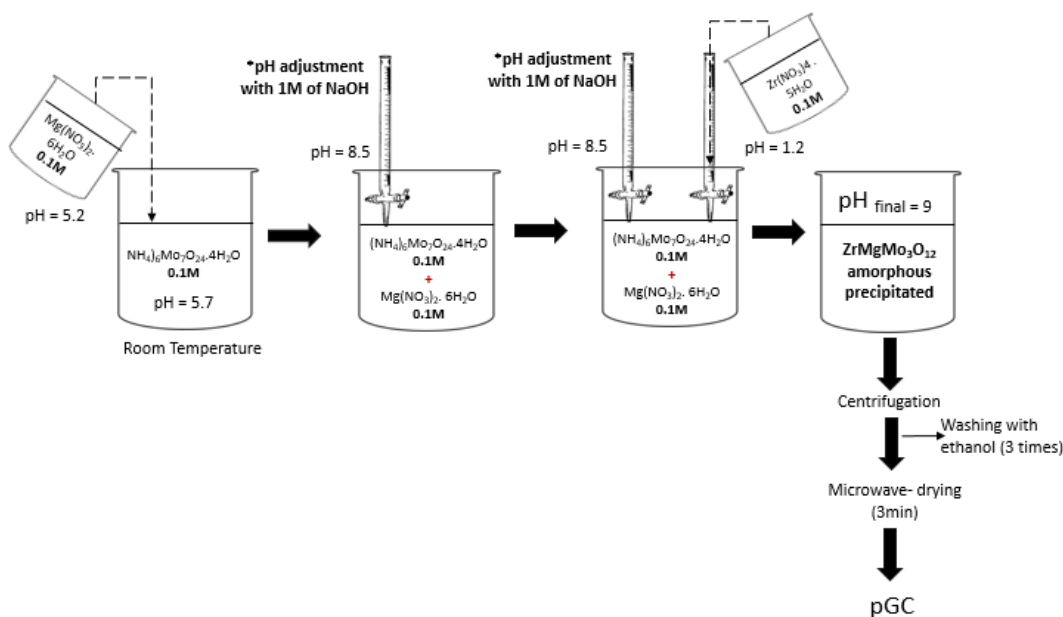


Figure 41: Co-precipitation by dripping reactants at controlled pH ( 9) as an attempt to synthesize  $\text{ZrMgMo}_3\text{O}_{12}$ .

### B.1.3.

#### Result and discussion

The crystallization temperature of the samples synthesized by co-precipitation of mixing reactants was based on TGA/DSC results (Figure 42). A weight loss between 20 and 40% was observed for all samples. The first endothermic peak (slightly above 100 °C) is associated with the release of remaining water while the other exothermic peaks correspond to the formation of oxides according to Table 12.

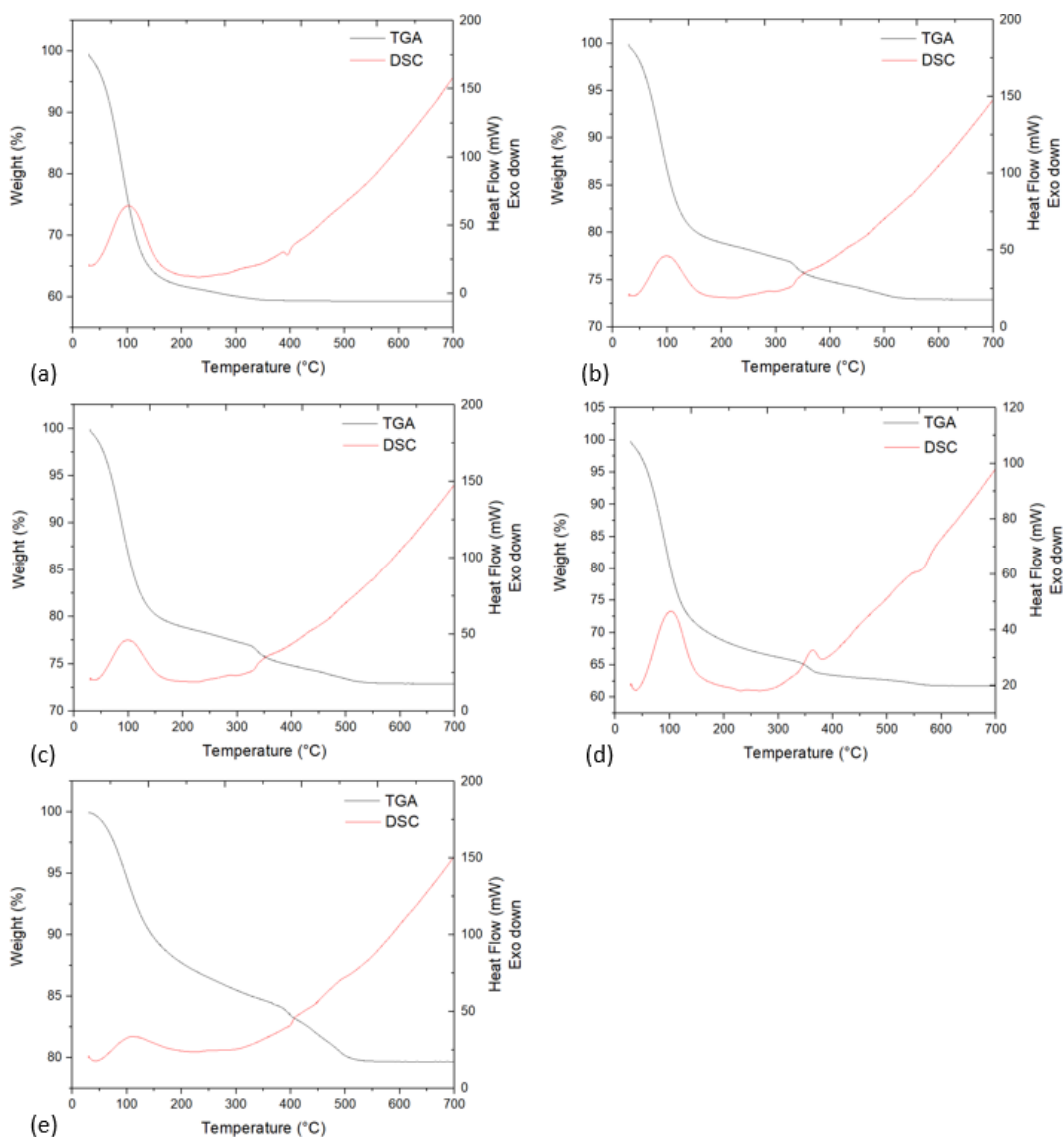


Figure 42: TGA/DSC of  $ZrMgMo_3O_{12}$  precursors obtained by co-precipitation by mixing reactants (a) S1; (b) S2; (c) S3 (d) S4 and (e) S5

Table 12 shows the crystallization temperature applied and the crystallized phases for the precursors obtained through co-precipitation by mixing reactants.

Table 12: Calcination temperature of  $\text{ZrMgMo}_3\text{O}_{12}$  precursors obtained through co-precipitation by mixing reactants.  $\text{ZrMo}_2\text{O}_8$  presents in the samples is a hexagonal phase.

Calcined Sample	Calcination temperature (°C)	Time (min)	Phase composition
S <sub>1</sub>	400	20	Not specified
S <sub>2</sub>	400	20	Amorphous
	550	20	Not specified
S <sub>3</sub>	400	20	Amorphous
	600	20	Not specified
S <sub>4</sub>	400	20	Amorphous
	550	20	Amorphous
	800	300	Not specified
S <sub>5</sub>	400	20	Amorphous
	550	20	Not specified

The XRPD patterns of the samples synthesized by co-precipitation of mixing reactants are presented in Figure 43.

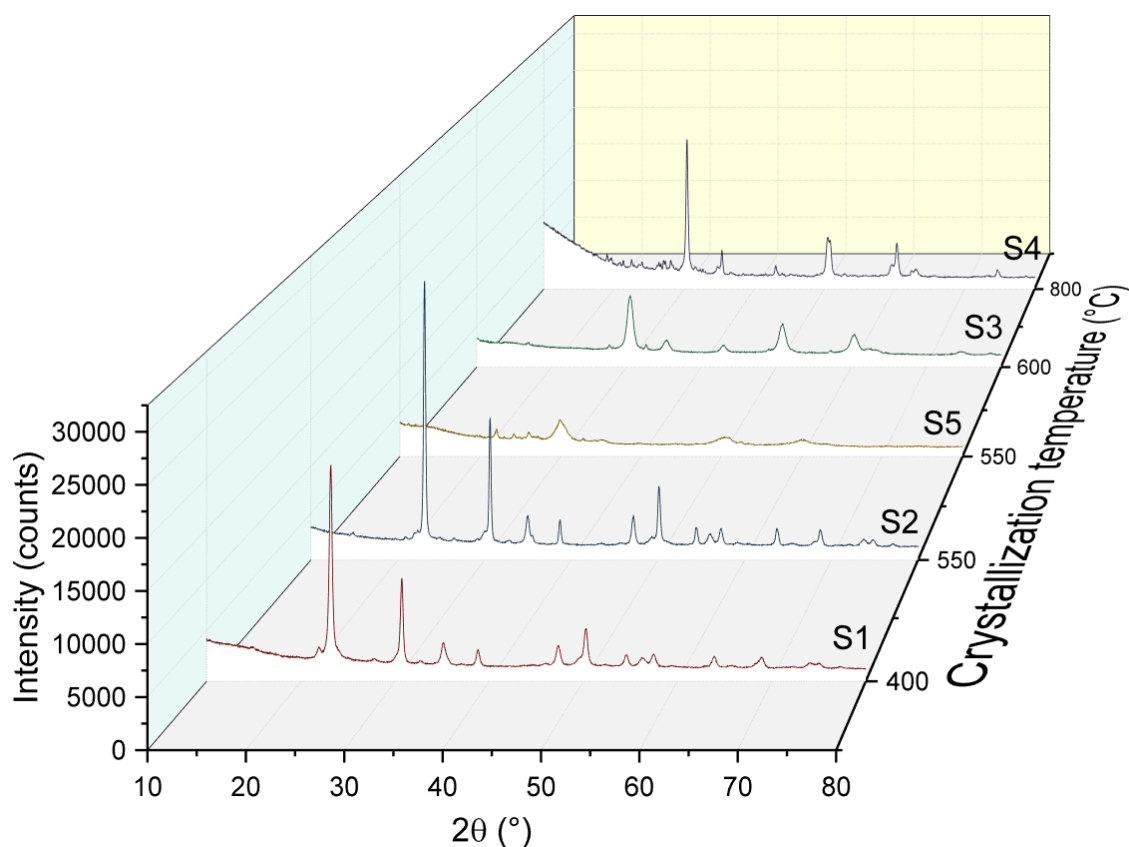


Figure 43: XRPD of samples obtained by co-precipitation by mixing reactants as an attempt to synthesize  $\text{ZrMgMo}_3\text{O}_{12}$ .

It can be noted that the co-precipitation by mixing reactants was unsuccessful since  $\text{ZrMgMo}_3\text{O}_{12}$  was not formed. The peaks were associated with the formation

of different oxides (Table 12), which may be related to the effect of pH on the solubility of the reagents in this synthesis route. In this type of co-precipitation route, it is expected the formation of hydroxide or oxohydroxide-based amorphous precursors to be crystallized in the calcination stage.

In this way, the second attempt to achieve the  $\text{ZrMgMo}_3\text{O}_{12}$  phase was conducted by co-precipitation by dripping reactants at pH=9 using NaOH. The TGA/DSC data presented in Figure 44a shows an exothermic peak just before 600°C indicating an event that could be associated with crystallization and a weight loss close to 45% at 200°C. The first endothermic peak (100 °C) is associated with the loss of moisture. The calcination conditions (sample inserted in a tubular furnace at 800 °C, kept during 5 h, and removed after that) were based on a previous article [141] (see Figure 44b). The XRPD result shows that the synthesis was also unsuccessful once the peaks correspond to oxide phases that might be due to the decomposition of the  $\text{ZrMgMo}_3\text{O}_{12}$ , which may be stable at other lower crystallization temperatures.

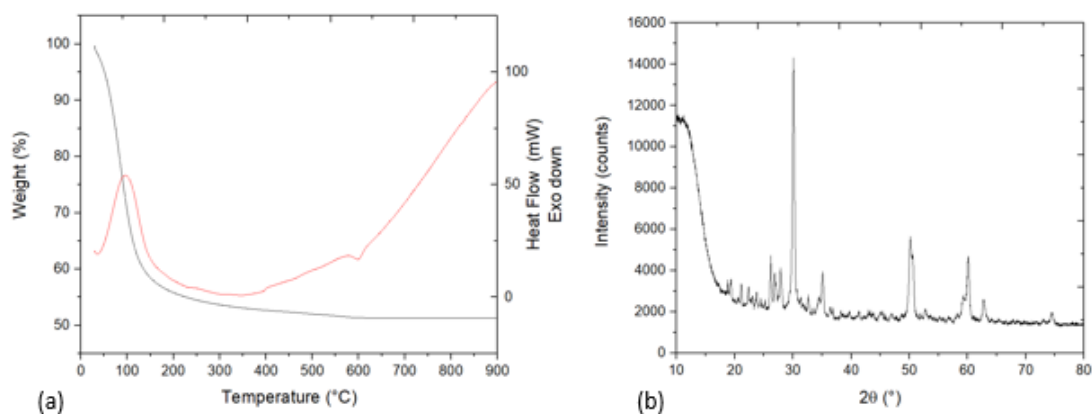


Figure 44: Co-precipitation dripping reactants at pH control ~ 9 (a) TGA/ DSC of pGC; (b) XRPD of the calcined powder GC\_800°C

#### B.1.4.

### Conclusions

The first synthesis attempt, co-precipitation by mixing reactants, did not crystallize the desired phase,  $\text{ZrMgMo}_3\text{O}_{12}$ , because the pH of the starting solutions was not in agreement to induce the supersaturation state for co-precipitation of the precursors.

The method of co-precipitation dripping reactants at pH control  $\sim 9$  could be a promising route regarding the theoretical foundations of precipitation. The weak sampling, exploiting only one calcination temperature, restricted the analysis due to the decomposition of the phases. Additional optimizations could be done to explore this route, however, using lower temperatures, such as  $700\text{ }^{\circ}\text{C}$ .